Queen Mary, University of London
School of Physics and Astronomy
Astronomy Unit

On the interaction between embedded planets and the corotation region of protoplanetary discs

Submitted in partial fulfillment of the requirements of the Degree of Doctor of Philosophy

By
Stephen Fendyke

September 2014

Declaration

I, Stephen Fendyke, confirm that the research included within this thesis is my own work or that where it has been carried out in collaboration with, or supported by others, that this is duly acknowledged below and my contribution indicated. Previously published material is also acknowledged below.

I attest that I have exercised reasonable care to ensure that the work is original, and does not to the best of my knowledge break any UK law, infringe any third party's copyright or other Intellectual Property Right, or contain any confidential material.

I accept that the College has the right to use plagiarism detection software to check the electronic version of the thesis.

I confirm that this thesis has not been previously submitted for the award of a degree by this or any other university.

Signature:

Date:

All the work in this thesis has been undertaken in collaboration with my supervisor, Professor Richard Nelson. In addition, the project presented in Chapter 5 was undertaken in collaboration with Dr Mario Flock of the CEA, Saclay, France. Unless otherwise stated, all figures in this thesis have been created by the author. This work was supported by an STFC PhD studentship.

Work in this thesis has been published in the following peer-reviewed papers, in collaboration with the listed authors:

Fendyke, S. M. and Nelson R. P. (2014). *On the corotation torque for low-mass eccentric planets.* MNRAS, 437(1):96–107.

Nelson, R. P., Hellary, P., **Fendyke, S. M.** and Coleman, G. (2014). *Planetary system formation in thermally evolving viscous protoplanetary discs.* Phil. Trans. R. Soc. A, 372

Acknowledgements

My first acknowledgement must be my supervisor, Professor Richard Nelson. Throughout my PhD, every problem felt much more approachable after speaking with him. Richard, for your wisdom and patience, thank you.

I also thank the other academic and administrative staff in both the School of Mathematical Sciences, where my PhD started, and the School of Physics and Astronomy, where it concluded.

I should like to acknowledge the support of my friends both in London and elsewhere, including all the PhD students in the Astronomy Unit at Queen Mary. Thank you all for the drinks, the conversations, the seminars, the coffee and everything else.

Of my friends, I must particularly single out Chris Haynes, with whom it was both an honour and a pleasure for me to share a flat (I will always fondly remember the *CIC*, the kittens, our 'May the Fourth' party and the late night combination of *Star Trek* and whisky), and Stephen Morgan, without whom I would never have been able to explore such an impressive fraction of London pubs; thanks for everything, chaps.

I should like to thank my sister and her family for their support over the years I have been studying, not least in the form of home-cooked food and a comfortable sofa to sleep on from time to time! Emma, Phil, Holly, Joseph; thank you.

Finally, I must thank the two wisest people I know, my parents, whose love, understanding and support through my time at university have been invaluable in everything I have achieved. From when I was very young, they encouraged and nurtured my nascent interest in science and never once failed to believe that I would make it this far. The debt I owe them can never be repaid, but it can be acknowledged, as it is here, and I must hope that my dedication of this thesis to them is able to do what words cannot, in expressing the true depth of my love and gratitude.

Abstract

Disc material in the corotation region librates with respect to low-mass planets on horseshoe trajectories. The exchange of angular momentum associated with this libration gives rise to the non-linear corotation torque (the horseshoe drag). For the first project described herein, we ran a suite of high-resolution 2D hydrodynamic simulations of low-mass (5 Earth mass) planets, at eccentricities $0 \leq e < 0.3$, embedded in both viscous protoplanetary discs with entropy relaxation and inviscid discs without. The attenuation of the corotation torque was obtained from these simulations and found to be well-fitted by an exponential decay with a characteristic 'e-folding eccentricity' that scales linearly with disc scale height. These results were tested with different disc scale heights between 0.03 and 0.1 and with a 10 Earth mass planet.

In the second project in this thesis we sought to extend on these results by examining the case of an embedded 5 Earth mass planet in three dimensional discs. We found that our scaling relation held in this new case, confirming that it is possible to use 2D simulations with a softening parameter to capture the behaviour of the corotation torque. We investigated the time-averaged horseshoe width as a function of altitude and found that the corotation region extends from the midplane to around three scale heights, changing most near the midplane for eccentric planets.

The final project looked at 3D radiative discs, under the influence of stellar irradiation, with more massive embedded planets capable of triggering gap formation. We use the PLUTO code to simulate a Jupiter mass planet at 5 AU in a protoplanetary disc. We describe our progress in understanding the process of gap formation in a case study of this class of hitherto undescribed disc.

Contents

List of Symbols

Symbol	Meaning
	Geometry
r	Spherical radius
R	Cylindrical radius
θ	Meridional angle (typically measured from from the z axis if not otherwise stated)
ϕ	Azimuthal angle
z	Height above disc midplane
	Theory
x_s	Horseshoe width; half-width of the corotation region
M_*	Stellar mass
m_p, r_p	Planet mass, orbital radius
q	Ratio of planet to star mass $= m_p/M_*$
G	Gravitational constant
Q	Toomre parameter
	Disc properties
ν	The kinematic viscosity ($= \alpha c_s H$, using the α-model of viscosity)
H	The scale height of the disc, typically $H = H(R)$
h	The aspect ratio of the disc. ($\equiv H/R$)
c_s	The sound speed in the disc
Ω	Angular velocity; Ω_k is the Keplerian velocity
γ	Adiabatic exponent
	Hydrodynamic quantities
σ	Surface density
ρ	Volume density
ρ_{mid}	Midplane density
T	Temperature
P	Pressure
e	Internal energy density
$K(s)$	Entropy function, $= P/\rho^\gamma$
$\mathcal{R}$	Ideal gas constant
μ	Mean molecular weight
$\mathcal{Q}$	Heating term
Λ	Cooling term

Planetary orbit	
i	Inclination
e	Eccentricity
Disc torques	
Γ_0	Torque normalisation
Γ_c	Corotation torque
Γ_L	Lindblad torque
α	Disc density power law: $\sigma = \sigma_0 r^{-\alpha}$
β	Disc temperature power law: $T = T_0 r^{-\beta}$
ξ	Disc entropy power law
$\Gamma_{\mathrm{c,e=0}}$	Corotation torque for a planet on a circular orbit
e_f	E-folding eccentricity

List of Figures

List of Tables

Chapter 1

The Formation and Evolution of Planetary Systems

In this chapter, I first describe and discuss the currently known population of extrasolar planets, the techniques by which they have been discovered and what they tell us about the process of planet formation. In section 1.2, I describe the protoplanetary discs in which planets are believed to form, discussing relevant observations and theory as they apply to disc formation, properties, evolution and structure. In sections 1.3 and 1.4, I describe two competing models of planet formation and the subsequent evolution of planets. This leads into the final section, 1.5, in which I describe disc-planet interactions.

1.1 Extrasolar Planets

Arguably the first attempt to apply modern scientific principles to the problem of detecting planets around other stars[1] was made by Captain W. S. Jacob of Madras in 1855. He deduced that a periodicity in the errors of orbits computed for the binary system *70 Ophiuchi* might be caused by the action of a third body in the system (Jacob, 1855). While this claim has since been shown to be incorrect (Heintz, 1988), it remains a milestone in the history of the field.

[1] Variously called either *exoplanets* or *extrasolar planets* in the literature and in this thesis.

Table 1.1: A brief summary of some of the major exoplanet detection missions along with the method each uses and whether it is ground- or space-based.

Name	Method	Ground/Space
Kepler	Transit	Space
CoRoT	Transit	Space
SuperWASP	Transit	Ground
OGLE	Microlensing	Ground
HARPS	Radial velocity	Ground
HATNet	Transit	Ground
LCOGT.net	Transit/Microlensing	Ground

The first accepted detection of an extrasolar planet around a main sequence star did not come for nearly a century and a half afterwards until the detection of *51 Pegasi b* by Mayor and Queloz (1995), using the radial velocity method described below. Since then, many hundreds of exoplanets have been confirmed, and the task of recording and cataloguing them has fallen to specialist websites such as `www.exoplanets.org`, produced and maintained by Wright et al. (2011), `www.exoplanet.eu` and the more recent *Open Exoplanet Catalogue*[2] developed by Rein (2012) and maintained by the community.

Figure 1.1 shows the semi-major axes and masses of currently confirmed exoplanets for which such values are available, colour-coded by method of discovery and with solar system planets shown for comparison. Some of the more well-known missions by which these data have been gathered are listed in table 1.1.

We first outline in section 1.1.1 the detection methods used to obtain these data before discussing the population of exoplanets shown in figure 1.1 in section 1.1.2.

1.1.1 Detection Methods

While the work in this thesis is theoretical, it is instructive to review the techniques used to detect and confirm the extrasolar planetary population against which we test our models and the associated biases. This section contains only a brief overview, and a more thorough review has been recently published by Wright and Gaudi (2013) to which the interested reader is referred. A compar-

[2]Hosted at `http://github.com/OpenExoplanetCatalogue`

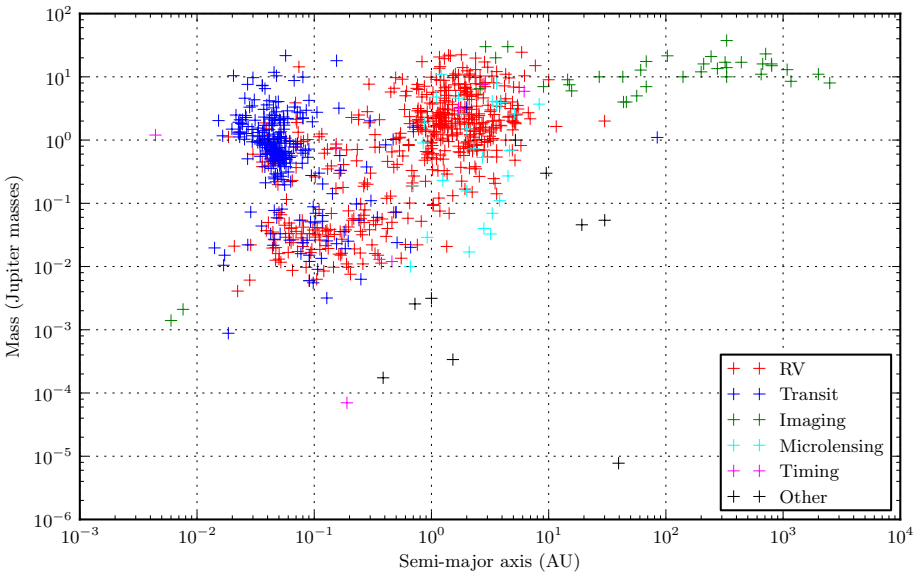

Figure 1.1: Mass against semi-major axis for the currently confirmed extrasolar planets for which mass and orbit data are available; note that $m_{\mathrm{p}} \sin i$ is given for planets detected by the radial velocity method, where a mass has not been otherwise determined. This plot was produced by the author on the 4th August 2014 and presents data on 823 exoplanets from the Open Exoplanet Catalogue, out of 1717 planets known; note that relatively few planets detected by the method of transits have a known mass. The biases of the different methods are manifested in the different regions of parameter space filled by each, as discussed in the text.

ison of the number of exoplanets detected by the different methods is shown in table 1.2.

Transit method A planet passing in front of its parent star– transiting– will naturally block some fraction of the starlight given by the ratio of the cross-sectional area of the planet to that of the star. If the size of the parent star is well-known, it is trivial to obtain a value for the radius of the planet. For readily apparent geometric reasons, only planets with orbits nearly perpendicular to the plane of the sky are liable to detection by this method. The maximum distance from its parent star that we can confirm a planet is limited by the finite length of the mission and the need to detect a number of transits before a planetary candidate can be confirmed. Without a sufficient number of repeat transit detections, there is the risk that a 'false positive' might be detected where, for instance, star spots mimic the decrease in brightness associated with a transiting planet.

Table 1.2: A comparison of the number of exoplanets detected by the different detection methods discussed in section 1.1.1. This table was produced by the author on the 4th August 2014 using data from the Open Exoplanet Catalogue.

Method	Planets confirmed
Transit	1139
RV	504
Imaging	38
Microlensing	28
Timing	8
Total	1717

One useful feature of this method is that it is sometimes possible to obtain spectroscoptic data from the planet, by considering variations in the depth of the transit as a function of wavelength during both primary and secondary transit events (that is, when the planet eclipses the star as well as when the star eclipses the planet). As planetary formation models become more sophisticated, this information about the composition of extrasolar planets may provide a useful diagnostic tool for constraining the formation histories of individual planets. Furthermore, as the spectral lines in the light emitted from the two sides of a rotating star are red-shifted and blue-shifted, it is also possible to extract the orbital inclination of the planet relative to the rotational axis of the star; this is known as the Rossiter-McLaughlin effect (Rossiter, 1924; McLaughlin, 1924). Brown et al. (2012) use this technique, for example, to constain the spin-orbit angles of *WASP-16*, *WASP-25* and *WASP-31*.

The orbit of an eclipsing body may be perturbed by its own moons or by other bodies orbiting its parent star. In either case, the perturbation to the orbit of the eclipsing body can be detected as *transit timing variations* or as *transit duration variations* (being, respectively, variations in the time of the start of a predicted transit event and variations in the duration of the transit) (Ford et al., 2012)[3]. In a system where multiple transiting planetary candidates have been detected, variations in transit timing and duration can be useful in confirming them and constraining masses (e.g. *Kepler 11* described by Lissauer et al., 2011).

Detections by this technique are easiest in the case of large planets, close to their parent stars. This is consistent with what we see in figure 1.1 in that a large population of transiting planets are shown (in blue) close to their parent

[3]And the other papers in the *Transit Timing Variations from Kepler* series.

stars. The light curve of a transit event is shown in figure 1.2.

Radial velocity method The bodies in an extrasolar planetary system orbit their common centre of mass. If the plane of the orbit is anything other than perfectly aligned with the plane of the sky, an observer, unable to resolve the planets, would note a periodic Doppler shifting of the spectral lines in the light of the observed star due to its motion along the line of sight. An example of such radial velocity data is shown in figure 1.2. The magnitude of the stellar radial velocity oscillation yields a lower limit to the mass of an orbiting planet and the periodicity similarly yields the orbital period though, as for the method of transits, a natural limit occurs here due to the finite length of our detection projects. In a system with a number of planets, given sufficient data, the observations can be decomposed to give mass estimates for them all. As an example, in our own solar system, Jupiter is responsible for a Solar radial velocity of approximately 12ms^{-1}, compared to the Earth's contribution of 0.1ms^{-1}.

Using this technique in the form of a survey to detect planets was first explicitly suggested by Struve (1952), who hypothesised that close-in Jupiter-mass planets could potentially be detected even with the observational resources available over half a century ago[4]; this was the scenario realised by Mayor and Queloz (1995) in their historic discovery of the first main-sequence extrasolar planet. Since then, this method has accounted for around 30% of all confirmed extrasolar planets (see table 1.2).

For geometric reasons, of course, use of radial velocity data alone can only ever yield a value for $m_\text{p} \sin i$ where m_p is the mass of the planet and i is its orbital inclination measured from the plane of the sky; thus we have a lower limit of mass. If radial velocity data is available for a transiting exoplanet, we are able to break this degeneracy for mass (as $i \approx \frac{\pi}{2}$ for a transiting planet by definition); furthermore, we can combine this with the measurement for the radius to obtain the density of the planet. The shape of the radial velocity curve allows us to also deduce the planetary eccentricity.

By astrometry A foreground star orbited by one or more planets will move in the plane of the sky relative to the stable background of fixed stars. Measuring this movement with sufficient precision would facilitate the indirect detection

[4]The author can find no such suggestion earlier in the literature. It is worth noting that Struve also suggests the method of transits as a means of exoplanet detection.

of any orbiting planets. No extra-solar planet detected by this method has yet been confirmed, but it is expected that the upcoming GAIA mission will be capable of detecting thousands of extra-solar planets around bright solar-type main-sequence stars within 200 parsecs (ESA, 2013; Casertano et al., 2008).

By microlensing If a foreground star approaches close to the line of sight between an observer and a distant star, the curvature of spacetime due to the mass of the foreground star will create a 'lens' effect, giving a distorted image of the distant star; formally, the distant star appears as a ring with radius equal to the Einstein ring radius of the foreground star. Without being able to resolve the lensing event, this appears simply as a characteristic increase in brightness of the distant star with respect to time, which reaches a peak and then decreases, with the magnitude of the increase determined by the geometry of the system and the mass of the foreground star.

A planet orbiting the foreground star will cause a secondary microlensing event to occur, the magnitude and timing of which will depend, again, on the geometry of the system and the masses of the bodies in it, including the planet. With unresolved photometry, this manifests itself as a further, shorter-lived increase in brightness; the magnification effect is greatest when the orbit of the planet takes it closest to the Einstein ring radius of its parent star. A microlensing event is shown in figure 1.2.

An advantage of detecting planets by this method is that as the events are random and even small planets cause detectable microlensing events, there is minimal bias to the planets detected and, as such, we are theoretically sampling the true underlying exoplanet population. It is also possible for relatively modest observational facilities to contribute to these detections by making independent measurements of brightness when a microlensing event is reported. However, these events occur only rarely, and it is not generally possible to follow up with other techniques or a repeat microlensing observation.

Through direct imaging While the direct detection by imaging of an extra-solar planet is the most conceptually simple of the methods listed here, it has to contend with practical difficulties given the overwhelming brightness of the parent star compared to any planetary companion.

Such a detection is easiest when the planet and the star are widely separated and when the detection is done in the infrared where the brightness ratio

between the star and the thermal emissions of the planet is most favourable. Young stars also retain residual heat from formation which can make them easier to detect. *Fomalhaut* and *HR 8799* (shown in figure 1.2) are examples of systems in which this method has detected planets (Marois et al., 2010).

Using timing variations Evidence of a planetary companion can be provided by variations in the arrival time of an expected signal, such as a pulse of light from a pulsar or minima in the light curve of an eclipsing binary. This method was responsible for the detection of the very first confirmed extrasolar planets in 1992 around a pulsar (Wolszczan and Frail, 1992).

1.1.2 Discussion

Before the detection of the first extrasolar planets, formation models for planetary systems had been devised with the solar system in mind; the goal was to devise a model which would produce a system with inner planets composed mainly of silicate rock, with giant planets of ice and other volatiles in the outer solar system, all on broadly coplanar orbits, surrounded by a reservoir of icy bodies in analogy to the Kuiper belt and Oort cloud in our own solar system.

As we see in figure 1.1, though, these do not appear to be general features common to all planetary systems. One of the greatest early surprises of the young field of exoplanet detection has been the large population of short-period massive planets ('hot Jupiters') orbiting close to their parent stars. The high temperatures and relative lack of material in the inner disc from which to form planets makes it very unlikely that they could have formed *in situ* and provides a compelling motivation to consider the possibility of significant post-formation evolution of planetary systems; specifically, the migration of planets through tidal interactions with the disc in which they are embedded. This is discussed further in section 1.5.

There is also evidence of multiple planet systems composed of compact, short-period planets of low and intermediate mass (super-Earths and Neptune-mass planets); examples of these systems include Kepler-11 with six planets (Lissauer et al., 2011), Kepler-20 with five (Gautier III et al., 2012), Kepler-62 with five (Borucki et al., 2013) and HD 10180 with up to seven detected by the HARPS spectrograph using the radial velocity method (Lovis et al., 2011). For the Kepler planets, at least, we can be certain that they are all coplanar.

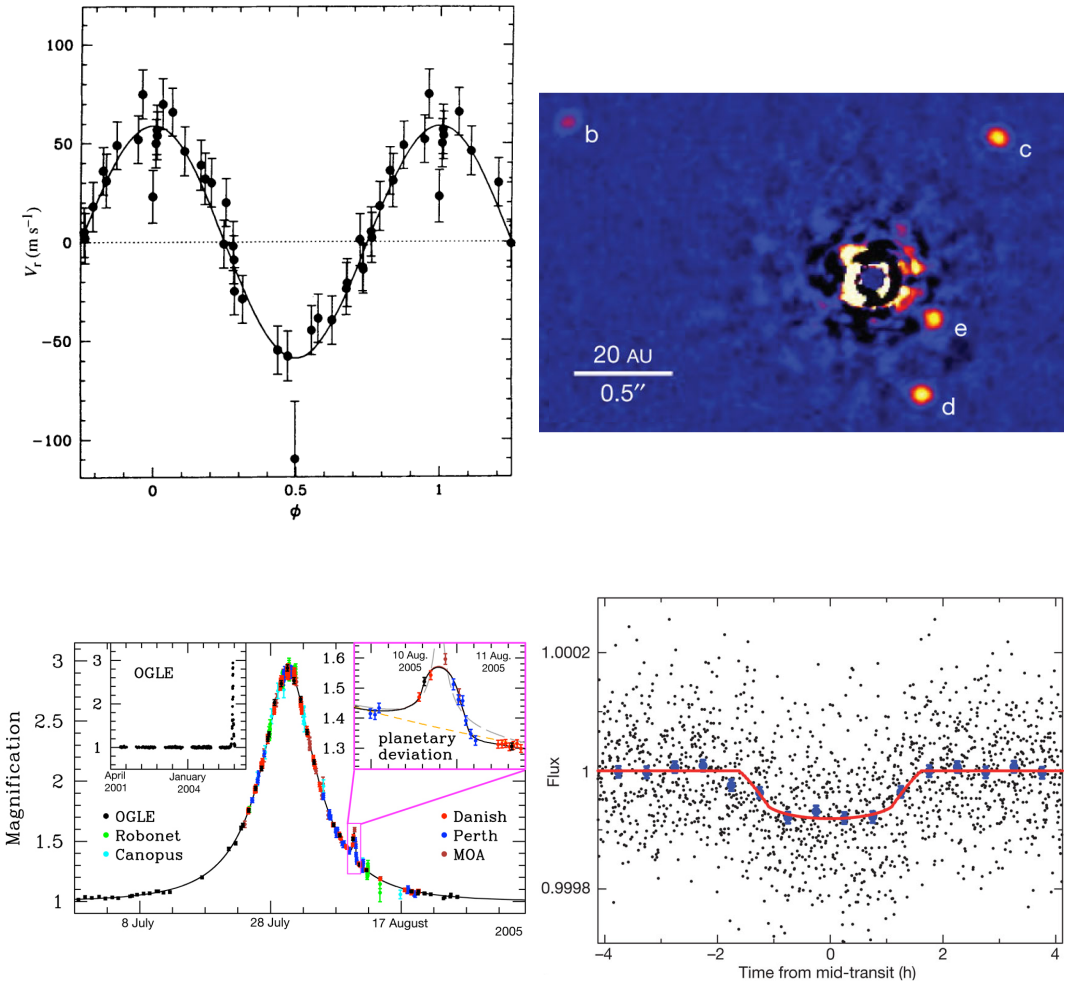

Figure 1.2: An illustration of some of the methods used to detect extrasolar planets: **Radial velocity (upper left)** radial velocity measurements of the star *51 Pegasi* 'folded' into a single orbital period (that is, plotted modulo 2π) after being corrected for long-term variation (image credit: Mayor and Queloz (1995)); **Direct imaging (upper right)** the system *HR 8799* as presented by Marois et al. (2010); **Microlensing (lower left)** the light curve of *OGLE-2005-BLG-390* showing the magnification effect of a microlensing event (image credit: ESO PR Photo 03b/06 (2006)); and **Transit (lower right)** Kepler photometry of the transiting planet Kepler-20e, folded into a single orbital period, where the blue dots are the binned data with 1σ error bars (image credit: Fressin et al. (2011)). These figures have been modified by the author for this thesis.

Other systems have been reported with planets of different masses; Endl et al. (2012), for example, present a mass determination using radial velocity and transit data for the planet ρ^1 *Cnc e* of $8M_\oplus$, which orbits a G-type star in a system with four other massive ($m_p \sin i$ =0.165, 0.17, 0.8 and 3.5 $M_{\rm Jupiter}$) planets detected by the radial velocity method. Similarly, Fabrycky et al. (2012) present detections of four planetary systems of multiple massive planets (*Keplers 29, 30, 31 and 32*); Lissauer et al. (2012) present data for the multiple planet *Kepler*33 system, in which all the planets are of multiple Earth radii; and S. Udry et al. (2007) report a system consisting of two close-in 'super-Earths' with a 'hot Neptune' detected with the HARPS spectrograph.

Given this population of multiple-planet systems, we might expect the formation histories of many planets to be affected, and even dominated, by planet-planet interactions. This is addressed in section 1.4.

Not all planetary systems consist of planets within a few astronomical units of their parents stars, however; the directly-imaged system *HR 8799* harbours four planets of several Jupiter masses which orbit between 14 and 68 AU from their parent star, much further away than the massive planets in our own solar system (Marois et al., 2010).

1.2 Protoplanetary Discs

While the detection of extrasolar planets is a relatively new development, the idea that these planets might form and evolve in a protoplanetary disc is one that dates back in a recognisable form at least to Immanuel Kant and his *Universal Natural History and Theory of the Heavens*, published in 1755, in which was set out the principle that the solar system formed from a large cloud which collapsed towards the Sun and in which formed the planets– the so-called *nebular hypothesis*. During the centuries since Kant, this idea has been refined in its details but not in its core concept; the Sun is believed to have formed from a collapsing cloud, which became a rotating disc of gas and dust through conservation of angular momentum.

We can see compelling evidence for this theory in our own solar system, where there are a number of planets and smaller bodies, all orbiting the sun in the same direction on approximately coplanar orbits. The massive gas and ice

giant planets can be found in the outer region of the solar system, and the less massive planets composed primarily of silicate rock can be found in the inner part of the solar system. This is consistent with formation in a protoplanetary disc with an inner region where it is too hot for volatiles to condense separated by the *ice line*[5] from the cooler outer disc where volatile elements provide a greater store of material for planet formation, though the existence of extra-solar planetary systems described above, particularly the population of 'hot Jupiters', suggests formation is often followed by a period of migration.

It is useful at this point to provide a brief account of the formation and evolution of protoplanetary discs, as those processes are currently understood, and review the available observational evidence. While only material relevant to the work in this thesis is presented here, Dullemond and Monnier (2010) provide a thorough review of literature regarding the inner ($\lesssim 1AU$) disc, and Williams and Cieza (2011) discuss in some detail the disc beyond that. In addition, Armitage (2011) reviews the theory of angular momentum transport as it applies to protoplanetary discs in much more detail than is possible here. The discussion below follows these authorities.

1.2.1 The observations

Discs contain material at a wide range of temperatures, and consequently emit at a range of wavelengths. This allows us to draw conclusions about different regions of the disc from unresolved phototometry, linking a wavelength to a temperature and so to a radial location in the disc.

The first studies of populations of protoplanetary discs were made possible by the *Infrared Astronomical Satellite* (IRAS), which was soon after complimented by the clear optical images taken in the visible by the *Hubble Space Telescope*, such as the one shown in figure 1.3, of discs silhouetted against their relatively bright background environment with their shapes readily apparent. Observational work was and is being continued by the *Infrared Space Observatory* (ISO), the *Spitzer Space Telescope* and, most recently, the *Herschel Space Observatory* and the *Atacama Large Millimeter/submillimeter Array* (ALMA).

New observations continue to provide insight into the evolution of protoplanetary discs; the recent measurement of misaligned discs around the stars in a

[5]Sometimes given as the *snow* or *frost* line.

binary system (Jensen and Akeson, 2014), for example, suggests that it will be necessary to understand the effect of a binary companion on a protoplanetary disc in order to explain the formation of planets in these systems.

1.2.2 The formation

A protoplanetary disc is formed after the collapse of a region of a molecular cloud under gravity. As the cloud collapses, the presence of more distant material carrying greater angular momentum causes the rapid ($\lesssim 10^4$ years) formation of a disc. This collapsing core leaves a spherical cavity in the molecular cloud, evidenced by lower extinction of mid-IR emissions than might otherwise be expected. Our system now consists of a protostar surrounded by a disc and a much more massive envelope of material, and we can begin to think of it as a star with a disc– a young stellar object– rather than a molecular cloud.

Young stellar objects (YSOs) fall into different classes, as described by e.g. Williams and Cieza (2011), separated by the gradient of the spectral energy distribution between about 2 and 25μm, which are believed to broadly map to different stages in the evolution of the disc. Class 0 YSOs exhibit no optical or near-IR emission; the envelope mass is much greater than that of the star or the disc. Class I YSOs show a positive gradient ($\alpha_{IR} > 0.3$, where $\alpha_{IR} = \frac{\mathrm{d}\log \nu F_\nu}{\mathrm{d}\log \nu}$, between ~ 2 and 25 μm) and correspond to a star with a massive disc, roughly the same mass as the remaining envelope. Class II YSOs show a negative gradient ($-0.3 > \alpha_{IR} > -1.6$) where the envelope is virtually depleted and the disc has a mass of $\sim 1\%\mathrm{M}_*$; these are accreting discs with strong Hα and UV emissions. Finally, Class III YSOs, with a strongly negative gradient ($\alpha_{IR} < -1.6$) have negligible envelopes and low-mass, passive discs, with no or weak accretion. Note that flat-spectrum sources ($0.3 > \alpha_{IR} > -0.3$), representing an intermediate stage between Class I and class II YSOs have also been discovered.

1.2.3 The properties

True protoplanetary discs arise after the Class I phase, with the end of the star formation process and dissipation of the gaseous envelope. The disc now contains a few percent of the mass of the star.

Lifetimes Based on studies of disc abundance in clusters of various ages, disc lifetimes are believed to be between 1 and 10Myr, with most sun-like stars having lost their discs by 6Myr according to results from the *Spitzer Space Telescope* by Hernández et al. (2007). This is discussed more in the review by Wyatt (2008) and shown in figure 1.3.

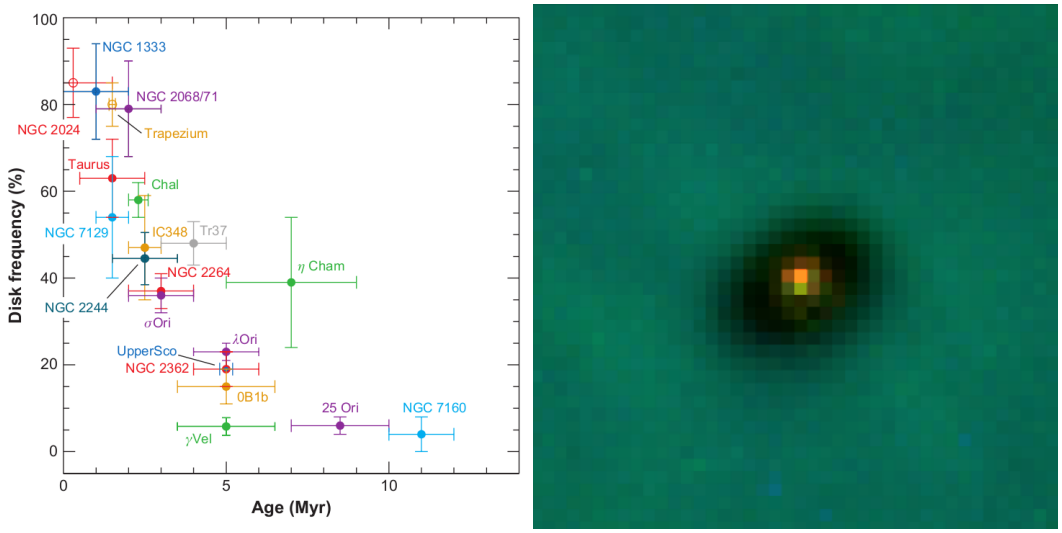

Figure 1.3: Protoplanetary discs: **(left)** the abundances of discs around sun-like stars (image credit:Wyatt (2008), based on Hernández et al. (2007)); and **(right)** an image taken by the *Hubble Space Telescope* showing a young star surrounded by its disc silhouetted against the background of the Orion Nebula (image credit: C.R. O'Dell/Rice University; NASA, news release STScI-1994-24, cropped by author).

Radial extent Vicente and Alves (2005) studied the silhouettes of discs in Orion and measured radii mostly ranging from 50 to 194 AU with two exceptional outliers of 228 AU and 621 AU. They estimate the radial extend of a number of other objects from the photoevaporative flows from their surfaces to get a mean of around 75 AU. The best fit to the intensity profiles of the silhouettes is found with a power-law surface density prescription, with an exponentially tapering factor to best fit the outer edge.

Density There is no universally accepted power-law profile that fits all observed discs, as all estimates rely on the tapering of the outer edge to obtain a value for the density profile further in.

As a crude model, Weidenschilling (1977) and later Hayashi (1981) were able to use the compositions of the planets and their present locations to estimate the minimum density distribution in the solar nebula required to form them;

the resulting density profile with a power law of $r^{-3/2}$ is known as the *minimum mass solar nebula* (MMSN). Weidenschilling gives the total mass as somewhere in range 0.01-0.07 solar masses. While this assumption of *in situ* formation is somewhat dubious, as we discuss in section 1.5, it provides us with at a starting point for disc density prescriptions. This can be compared with observational results, such as the submillimetre survey of Andrews and Williams (2005), who obtained a mean value for disc mass of 5×10^{-3} solar masses. They also quote a temperature profiles of $T \propto r^{-q}$, with q in the range $0.4 - 0.8$.

1.2.4 The evolution

There are two key physical processes governing the evolution of a protoplanetary disc, which each dominate during a different stage:

First, accretion onto the central star, which is driven by the transport of angular momentum through viscosity in the disc. Even without any embedded planets, a disc will evolve as a viscous fluid throughout its lifetime. As the disc ages, it will move inwards and be accreted onto the central star (e.g. Pringle, 1981; Papaloizou and Lin, 1984, 1995).

In order to derive accretion rates that match observations, we require a disc viscosity many orders of magnitude greater than that possible due to the interactions between molecules. The dominant physical process now believed to give rise to disc viscosity is the magnetorotational instability (MRI)[6] described by Balbus and Hawley (1991), which is set up due to coupling between the disc material and a weak magnetic field present in the disc, possibly brought in during the collapse of the molecular cloud. While this instability is believed to dominate hydrodynamic turbulent effects, for the required coupling to exist, the disc must be ionised.

Building on this idea, Gammie (1996) suggested a 'dead zone' ought to develop, in the region of the disc too cool to be susceptible to collisional ionisation and sufficiently well shielded to not be ionised by high energy stellar radiation or cosmic rays. The disc would then have vertical structure with viscous inner and outer regions, viscous 'active' surface layers and a shielded dead zone layer. This model is supported by modelling by, e.g. Terquem (2008), but there is as yet no observational confirmation.

[6]Also known as the Balbus-Hawley instability.

The existence of dead zones, or not, may have implications for planet formation models; Nelson and Gressel (2010) for example, simulate 3D MHD discs with embedded planetesimals with radii below 10km using both full discs and smaller 'shearing box' simulations. They find that the effect of significant MHD turbulence is to increase the velocity dispersion in the disc and cause a destructive effect on planetesimals. This suggests that planetesimal accretion is likely to operate primarily in dead zones of protoplanetary discs.

As a prescription for viscosity, we often use the so-called α-model, described in section 2.1.1, supported by Balbus and Papaloizou (1999).

The second key physical process operating in a protoplanetary disc is photoevaporation. High energy photons (FUV, EUV and X-ray) incident on the layers of the disc furthest from the midplane heat those regions to the point where they have sufficient thermal energy to escape the star; this is the origin of a photoevaporative flow from the disc surface.

Initially, accretion onto the central star is thought to be the dominant physical process with viscosity ensuring that the inner disc is replenished from the outer regions. As accretion decreases the disc mass, the accretion rate falls, and photoevaporation becomes important. When the rate of accretion falls below the rate of photoevaporation, material is being removed from the inner disc faster than it can be replenished by the outer disc and the inner disc becomes depleted on a viscous timescale ($\lesssim 10^5$years). With the depletion of the inner disc, the rest of the disc is no longer shielded from high-energy photons, which begin to impact and photoevaporate the outer disc. At this point, accretion no longer occurs (Clarke et al., 2001).

The rapid transition between Classical T Tauri Stars and Weak-line T Tauri Stars[7] leads us to believe that the photoevaporation occurs on a short timescale. With the removal of the disc, planet formation must proceed by dynamical processes, as disc-driven processes no longer occur. The later development of planetary systems is beyond the scope of this thesis.

[7]Often denoted CTTS and WTTS respectively, where the former is an optically-visible star showing clear signs of accretion where the latter shows none.

1.2.5 The structure

We are concerned with the protoplanetary disc phase during which planet formation takes place. In a real protoplanetary disc, an equilibrium is reached between gravitational and pressure forces acting on the disc, and between radiative heating and cooling and viscous heating. By considering a simple model disc, it is possible to derive a number of results that will be of later use and allow us to understand the structure of these objects. In what follows, r refers to the spherical distance between the central star of mass M_* and a disc element, θ is the altitude of the element, typically measured from the z-axis, R is the **cylindrical** distance to the disc element $= r\sin\theta$, z is the height of the element from the midplane. This is shown schematically in figure 1.4.

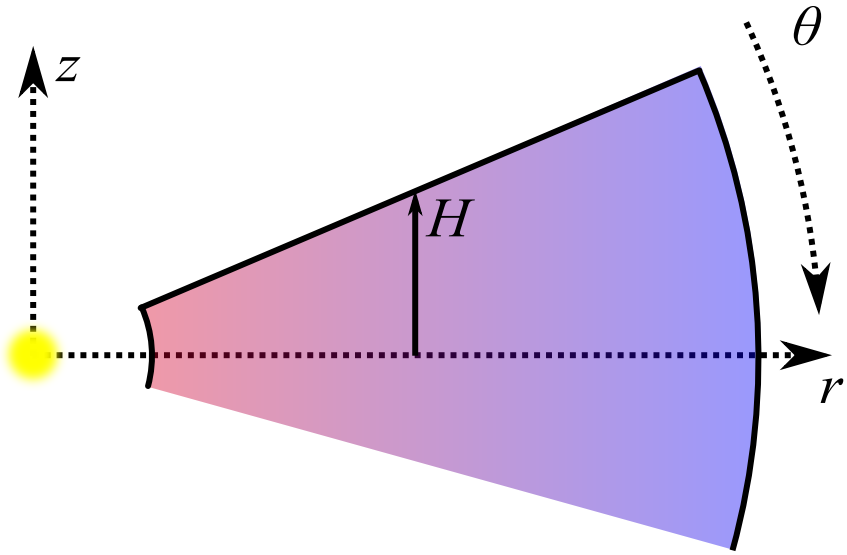

Figure 1.4: A schematic of an azimuthal slice of a disc. Note that the cylindrical radius, R, is related to the spherical radius, r, by $R = r\sin\theta$. H is the scale height of the disc, discussed in the text.

By noting that inter-molecular forces can be neglected, we first assume the ideal gas law, writing it as

$$P = \frac{\mathcal{R}}{\mu} T\rho, \tag{1.1}$$

where P is the pressure, T is the temperature, ρ is the density, $\mathcal{R}$ is the molar gas constant and μ is the mean molecular weight of the gas. From the ideal

gas law, we immediately obtain the isothermal sound speed if we assume that T is constant (an assumption which implies a rapid balance between heating and cooling);

$$c_{\mathrm{s,iso}}^2 = \left.\frac{\mathrm{d}P}{\mathrm{d}\rho}\right|_T = \frac{\mathcal{R}}{\mu}T. \tag{1.2}$$

Similarly, the sound speed in an adiabatic disc can be derived from the equation governing an ideal gas undergoing an adiabatic process, $P = K(s)\rho^\gamma$;

$$c_{\mathrm{s,adi}}^2 = \left.\frac{\mathrm{d}P}{\mathrm{d}\rho}\right|_{K(s)} = \gamma\frac{\mathcal{R}}{\mu}T. \tag{1.3}$$

Let us consider a protoplanetary disc in which temperature and midplane density are simple power law functions of R such that

$$T(R) = T_0\left(\frac{R}{R_0}\right)^q, \tag{1.4}$$

and

$$\rho_{\mathrm{z}=0}(R) = \rho_0\left(\frac{R}{R_0}\right)^p. \tag{1.5}$$

By employing this simple model, we can derive the equilibrium density and angular velocity for our disc by equating the R and z components of the centripetal acceleration, the graviational force and the pressure force in the disc;

$$R\Omega^2 - \frac{GM_*R}{(R^2+z^2)^{\frac{3}{2}}} - \frac{1}{\rho}\frac{\partial P}{\partial R} = 0, \tag{1.6}$$

$$-\frac{GM_*z}{(R^2+z^2)^{\frac{3}{2}}} - \frac{1}{\rho}\frac{\partial P}{\partial z} = 0, \tag{1.7}$$

which can be solved to give

$$\rho(R,z) = \rho_0 \left(\frac{R}{R_0}\right)^p \exp\left[\frac{GM_*}{c_s^2}\left(\frac{1}{\sqrt{R^2+z^2}} - \frac{1}{R}\right)\right], \tag{1.8}$$

and

$$\Omega^2(R,z) = \Omega_k^2\left(\left(\frac{H}{R}\right)^2(p+q) - \frac{qR}{\sqrt{R^2+z^2}} + (1+q)\right). \tag{1.9}$$

Note that using the thin disc approximation ($z \ll R$), we can perform a binomial expansion on the inverse square root and thence reduce the expression to

$$\rho(R,z) = \rho_0 \left(\frac{R}{R_0}\right)^p \exp\left[\frac{GM_*}{c_s^2}\left(-\frac{1}{2}\frac{z^2}{R^3}\right)\right], \tag{1.10}$$

or, by introducing the quantity H such that $H^2 = c_s^2R^3/GM_* = c_s^2/\Omega^2$,

$$\rho(R,z) = \rho_0 \left(\frac{R}{R_0}\right)^p \exp\left[-\frac{z^2}{2H^2}\right]. \tag{1.11}$$

From this, it is clear that in the thin disc regime the disc density decays in a Gaussian fashion away from the midplane and that $H = c_s/\Omega$ is a measure of disc thickness. Since $c_s^2 \propto T$ by equation 1.2 and $T \propto R^q$ by equation 1.4, we have a radial dependence of H of

$$H = c_s/\Omega \propto R^{q/2}/R^{-3/2} = R^{(q+3)/2} \tag{1.12}$$

which can be expressed as

$$h = \frac{H}{R} = R^{(q+1)/2}. \tag{1.13}$$

This non-linear (in general) relationship between H and R is known as disc "flaring" and has implications for planetary migration– a process that depends strongly on the local h of the disc, as discussed in section 1.5.

The inner edge of the dust in the protoplanetary disc is believed to be determined by the sublimation temperature of around 1,500K, supported by observational evidence in the form of a near-infrared 'bump' at a wavelength consistent with that temperature. Interior to this, the disc is much hotter and more optically thin such that the inner edge appears as a discrete boundary. This is discussed in much greater detail by Dullemond and Monnier (2010).

1.3 Formation of Planets

There are two commonly cited models of planetary formation; the *core accretion* model and the *gravitational instability* model. It should be noted that these models are not mutually exclusive; they operate in different regimes and that one or other, or both, could be expected depending on the disc properties.

1.3.1 Core accretion

This model originated with the work of Safronov (1969)[8] and has been investigated using numerical simulations (e.g Pollack et al., 1996; Movshovitz et al., 2010); a recent review has been published by Hubickyj (2010).

Under the standard model of core accretion, dust and volatile compounds

[8]Here cited in translation.

which have condensed out of the protoplanetary disc settle in the disc mid-plane, clump together and grow by collisions (Helled et al., 2013). As these grains grow into planetesimals, the more massive ones begin to grow significantly faster than those that are less massive because of *gravitational focusing*; that is, the increase in collisional cross-section by a factor $\sqrt{1 + v_{\text{esc}}^2/v^2}$ due to the effect of its gravity (where $v_{\text{esc}} = \frac{2GM}{R}$ is the escape velocity of the body dependent on its mass and radius and v is the velocity of a body being accreted) which favours the bodies of a larger initial mass.

The rate of mass accretion of such a planetesimal of mass M and radius R will be given by the cross-section derived from the effective radius of accretion R_{eff}, the number density of surrounding bodies being accreted n and their average mass and velocity, m and v.

$$\frac{\mathrm{d}M}{\mathrm{d}t} = nmv\pi R_{\text{eff}}^2 = nmv\pi R^2 \left(1 + v_{esc}^2/v^2\right) \tag{1.14}$$

As a small number of bodies become considerably more massive than the rest, such that their escape velocities dominate the average velocity in the disc, we find a mass doubling time of $\Delta t \propto M^{-1/3}$; that is, the most massive planetesimals grow the most rapidly. This is known as *runaway* growth.

Eventually, these larger planetesimals stir the velocity dispersion in the disc such that $v \approx v_{\text{esc}}$. In this regime, the doubling time[9] goes as $M^{1/3}$. This is the much slower stage of evolution known as *oligarchic growth*, where these bodies grow by accreting material in their 'feeding zones' until they reach their isolation masses. Protoplanets formed by this process beyond the ice line are able to reach greater masses due to condensed volatiles in that region of the disc.

After this, protoplanets in the inner disc continue to grow by giant impacts, while protoplanets in the outer disc are massive enough to accrete a gaseous envelope.

While the core accretion model provides a roadmap for the formation of both silicate rock and giant and icy planets and nicely explains planetary metallici-

[9]The doubling time Δt can be obtained by: $\frac{2M-M}{\Delta t} \approx 2nmv\pi R^2$ if $v_{\text{esc}} \approx v$. Then $\frac{M}{\Delta t} \propto M^{2/3}$ and $\Delta t \propto M^{1/3}$.

ties, it depends on the coagulation process whereby grains grow into planetesimals and then embryos which is, as yet, poorly understood.

1.3.2 Gravitational Instability

Kuiper (1951) first put forward the idea that if a protoplanetary disc were to be sufficiently massive, it would be unstable to gravitational collapse under its own gravity against the effects of pressure and azimuthal shear. This effect is quantified by the Toomre instability parameter,

$$Q = \frac{c_s \Omega}{\pi G \sigma}, \tag{1.15}$$

where c_s is the sound speed in the disc, Ω is the orbital frequency and Σ is the gas surface density. When $Q \lesssim 1$, the disc is susceptible to gravitational collapse. In general, Q will vary through the disc such that gravitational collapse will be more likely in cooler, more massive regions than in less massive, warmer regions. Gammie (2001) has also shown that planet formation by this method requires the rapid cooling of clumps when they form.

The gravitational instability model provides a particularly good explanation for the existence of massive planets at large distances from their parent stars (e.g. in the *HR 8799* system). However, the prevalence of discs in which self-gravity is an important effect and the process of fragmentation are still not fully understood; nor does this method easily explain the existence of intermediate-mass planets. A recent review of research in this area has been published by Mayer (2010).

1.4 Evolution of Planetary Systems

The two most widespread models of planetary formation are the core-accretion model and the gravitational instability model described above.

However, as Mayor and Queloz (1995) noted of the planet they had discovered; *The very small distance between the companion and 51 Peg is certainly not pre-*

dicted by current models of giant planet formation. Those models had assumed that giant planets would be found in the outer part of the solar system, as in our own, due to the much greater amount of material available beyond the ice line for planet formation. In fact, as we see from figure 1.1, there is a large population of very massive planets close to their parent stars which provides compelling evidence to believe that there is a considerable amount of post-formation evolution of planetary systems, caused by interactions between planets, the disc and the central star.

We can consider these different types of interaction separately:

Planet-Planet Interactions Planets can interact with each other in a number of ways, as discussed by e.g. Davies et al. (2013). They can collide and catastrophically disrupt, or join together. They can interact with each other through resonances in a number of ways. Planets may be locked into mean-motion resonances, for instance, which constrain them to migrate in step with one another (Snellgrove et al., 2001); Terquem and Papaloizou (2007) find in simulations of such systems that near commensurability can be maintained and that hot super-Earths and Neptunes might not be expected to be isolated– a result consistent with observational evidence discussed in section 1.1.2.

The eccentricities of one or more planets may be excited to much higher levels (e.g. Cresswell and Nelson, 2006), potentially leading to planets being ejected from the system. There is also the Kozai mechanism by which eccentricity and inclination can be exchanged; Wu and Murray (2003), for example, have suggested that the presence of a binary companion in the system *HD 80606* could facilitate Kozai oscillations, potentially explaining the planet in that system of eccentricity 0.93. Chatterjee et al. (2008) have shown that planet-planet interactions can reproduce the observed exoplanet eccentricity distribution.

Planet-Star Interactions A planet orbiting close to its parent star can have its eccentricity damped through *tidal circularisation*, or be *tidally locked* such that its rate of rotation about its axis is equal to its orbital time and one of its sides always faces the star. This was discussed by, for example, Jackson et al. (2008).

Planet-Disc Interactions As the main focus of the work in my thesis, this is discussed more thoroughly in section 1.5 below.

1.5 Disc-Planet interactions

The gravitational interaction between an embedded protoplanet and its parent protoplanetary disc can change the orbital parameters of the protoplanet (as discussed by, e.g. Chambers, 2009). Large changes in the planet's semi-major axis are referred to as *planetary migration*, a process which can occur in a number of ways. Depending on the mass of the planet, the star and the disc, the migration will fall into one or other of the following regimes (*types*) of migration based on the nomenclature developed by Ward (1997).

Planet-disc interactions can also cause planetary ecccentricity and inclination to change, as discussed briefly in section 1.5.5.

Recent thorough reviews of this material include those by Kley and Nelson (2012) and Baruteau et al. (2013).

1.5.1 Type I migration

If the ratio of the planet's mass to the mass of the central star, $q \ll h^3$, where h is the ratio of the disc scale height to radius, then the perturbation to the disc due to the presence of the planet is small and the structure of the disc is not significantly altered (Korycansky and Papaloizou, 1996). For a disc with $h = 0.05$, this corresponds to a planet mass of much less than $40\mathrm{M}_\oplus$, typically planets up to Neptune-mass ($15 - 20\mathrm{M}_\oplus$).

Lindblad torque

Locations in the disc where material regularly encounters the planet's potential and experiences a periodic forcing are known as *Lindblad resonance* radii; at these locations, the planet's potential causes waves to be launched in the disc, transferring angular momentum between the planet and disc material. Neglecting pressure and self-gravity, in a Keplerian disc with a planet on a circular orbit, these occur at radii given by

$$r_L = \left(\frac{m}{m \pm 1}\right)^{\frac{2}{3}} a_p, \tag{1.16}$$

for positive integer m, where a_p is the planet's semi-major axis. However, the effect of pressure in a disc is to cause a 'pile-up' of Lindblad resonance locations for $m \gg 1$ at $r_L = a_p \pm \frac{2}{3}H$; this has the effect of attenuating the contribution of the high m modes to the total Lindblad torque, known as the 'torque cut-off' (Artymowicz, 1993).

The cumulative torque due to all these launched waves is known as the *Lindblad* (or *wave*) torque, and the associated density perturbation in the disc takes the form of a spiral density wave (Ogilvie and Lubow, 2002). Physically, we can think of the inner wave, leading the planet, pulling the planet 'forward'. This acts as a positive torque with the effect of causing outward migration; analogously, the density wave in the outer disc applies a negative torque. The resultant torque on the planet is the residual of the two; the *differential* Lindblad torque, often just called the Lindblad torque.

Theory developed by Goldreich and Tremaine (1979) allows an analytic expression for the total torque on the planet due to this interaction to be derived by considering a Fourier decomposition of the planet's potential and calculating the torque due to the superposition of potential modes by using the linearised equations of hydrodynamics. These linear perturbation equations have also been solved numerically by Korycansky and Pollack (1993).

Paardekooper et al. (2010) found that for 2D discs with a surface density profile $\sigma \propto r^{-\alpha}$ and a temperature profile $T \propto r^{-\beta}$, the linearised fluid equations of Paardekooper and Papaloizou (2008) yield the following expression for the Lindblad torque

$$\gamma \frac{\Gamma_L}{\Gamma_0} = -2.5 - 1.7\beta + 0.1\alpha, \tag{1.17}$$

where γ is the disc adiabatic exponent and the normalisation of the torque is

$$\Gamma_0 = \frac{q^2}{h^2} \sigma_p r_p^4 \Omega_p^2, \tag{1.18}$$

where q is the ratio of the planet's mass to that of the central star, $h = H/r$, and a subscript p indicates a quantity to be evaluated at the planet's location.

This agrees well with work by Masset (2011) for generalised temperature and density profiles.

Parameter space has not yet been thoroughly explored in three dimensions, due in part to the computational complexity of such a problem, with only simulations of isothermal discs having been studied in detail by Tanaka et al. (2002). It should be noted that a correct gravitational softening parameter (that is, a correction to the distance term in the planet potential of $d^2 = \Delta x^2 + \Delta y^2(+\Delta z^2) + b$) is necessary in order for 2D and 3D simulations to be comparable (Müller et al., 2012).

We expect a (region of a) disc which can cool effectively to approach the isothermal regime ($\gamma \rightarrow 1$), whereas an inefficiently cooling region would be best modelled by the adiabatic result given. Paardekooper et al. (2011) demonstrated that an effective γ can be defined, based on the thermal diffusion coefficient, to model regions with intermediate thermal diffusion for which neither an isothermal nor an adiabatic model is entirely appropriate.

For typical values[10], an Earth-mass planet at 1 AU would be expected to migrate inwards on a timescale of 4×10^5 years. A Neptune-mass planet at the same initial orbital radius would migrate in more rapidly (as the Lindblad torque increases with planet mass) on a timescale of just 2×10^4 years. This is two orders of magnitude shorter than the expected disc lifetime and, without considering other effects, presents problems for theories of planet formation.

Papaloizou and Larwood (2002) have shown that for eccentric planets, the differential Lindblad torque becomes more positive with increasing eccentricity, reversing direction and becoming positive overall for typical disc profiles at $e \approx 1.1\frac{H}{r}$. It should be noted, however, that Cresswell et al. (2007) demonstrated that a positive torque does not necesarily lead to an increase in semi-major axis due to the energy being removed from the planetary orbit by eccentricity damping.

Corotation torque

In addition to the interaction at Lindblad resonances, a strong interaction also occurs between the planet and material at approximately the same orbital

[10] Assuming a solar mass star, $h = 0.05$ and $\sigma = 2000(r_p/1\mathrm{AU})^{-3/2}\mathrm{gcm}^{-2}$

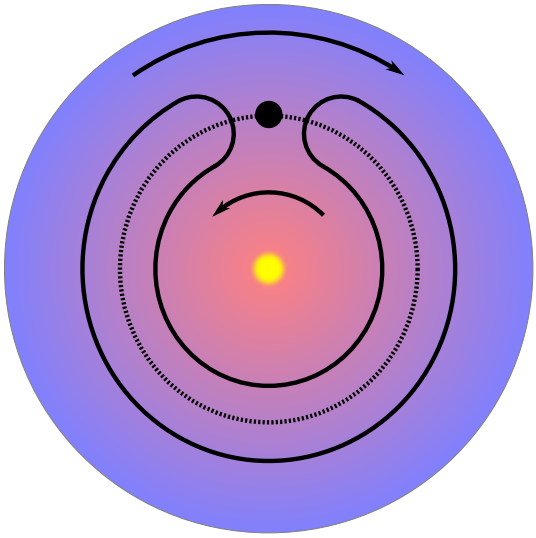

Figure 1.5: This figure shows a schematic of a disc, divided into different regions. Material librates on horseshoe trajectories relative to the planet (shown in black). One of these trajectories is shown, with the direction of the disc material, as seen in the corotating frame, indicated on the disc. The disc is divided into the warm inner disc, the corotation region and the cool outer disc.

radius. Goldreich and Tremaine (1979) used the same linear theory described above to derive expressions for the so-called *linear corotation torque*. Tanaka et al. (2002) showed, however, that in typical disc surface density profiles, this linear torque is dominated by the Lindblad torque.

A different approach to considering the corotation region was developed by Ward (1991), using the fact that disc material that is nearly co-orbital with the planet will librate on so-called horseshoe trajectories[11] relative to the planet, being moved from the inner to the outer disc, or vice versa, with each planetary encounter (see the schematic in figure 1.5). Such trajectories are missing from the linear theory in which horseshoe turns do not exist. An asymmetry between exchanges of material from the inner to the outer disc on one side and from the outer to the inner on the other results in a torque on the planet. This torque is known as the *vortensity-related horseshoe drag*, as the asymmetry is fuelled by the vortensity[12] gradient in the disc.

The relationship between the linear theory and the horseshoe drag model was clarified by Paardekooper and Papaloizou (2009b) and Paardekooper and Pa-

[11]Often known as 'horseshoe orbits' for brevity. More on such orbits can be found in Murray and Dermott (1999).

[12]Vortensity being specific vorticity, $= (\frac{1}{\sigma}\nabla \times \vec{v})|_z$.

paloizou (2009a); in a disc where horseshoe turns occur, the horseshoe drag replaces the linear corotation torque except in the case where a significant viscosity is present, with the horseshoe drag being an order of magnitude greater than the linear corotation torque in the limit of zero softening. **In this thesis, the phrase *corotation torque* can be taken to refer to the total torque arising from the interaction between the planet and disc material in the corotation region, unless otherwise explicitly stated.**

A second contribution to the non-linear corotation torque also exists in adiabatic discs fuelled by conservation of entropy. This *entropy-related corotation torque* manifests itself as an increase (or decrease) in density of disc material recently moved from the cool exterior (warm interior) disc to the warm inner (cool outer) disc in order to maintain hydrostatic equilibrium (Paardekooper and Mellema, 2006; Baruteau and Masset, 2008; Paardekooper and Papaloizou, 2008). The existence of a localised region of high density ahead of the planet and low density behind (see figure 1.7) causes the planet to experience a positive torque.

Paardekooper et al. (2010) calculated the following expression for the full, non-linear horseshoe drag on a planet in a disc with a surface density profile given by $\sigma \propto r^{-\alpha}$, a temperature power law profile given by $T \propto r^{-\beta}$ and an adiabatic exponent γ;

$$\gamma \frac{\Gamma_c}{\Gamma_0} = 1.1 \left(\frac{3}{2} - \alpha \right) + 7.9 \frac{\xi}{\gamma}, \tag{1.19}$$

where ξ is the entropy exponent, given by $\beta - (\gamma - 1)\alpha$ and the first and second terms on the right hand side correspond to the vortensity- and entropy-related corotation torques respectively. This result is comparable to similar work by Masset and Casoli (2009).

Saturation In an inviscid disc, the corotation region is a finite reservoir of angular momentum which will eventually be depleted when the horseshoe exchanges of disc material have mixed the corotation region such that the vortensity gradient has been flattened. When this occurs, the corotation torque will no longer be applied; this process is known as the saturation of the corotation torque. In a viscous disc, the disc is continuously seeking to relax back to its initial vortensity profile, maintaining the vortensity-related corotation torque.

In a similar way, thermal diffusion is required to unsaturate the entropy-related corotation torque. Without it, in an adiabatic disc, cool disc material moved to the inner disc will remain cool until moved back to the outer disc– the asymmetry of the horseshoe exchanges will be lost and the entropy-related corotation torque will saturate. In section 2.6.4, this is discussed further in the context of my simulations. Ideally, for an optimally unsaturated corotation torque, one would like displaced disc material to return to its equilibrium state on a timescale of some fraction of a horseshoe libration period. This is illustrated in figures 1.6 and 1.7 where the density perturbation at corotation can be observed to reach approximately half an orbit from the planet.

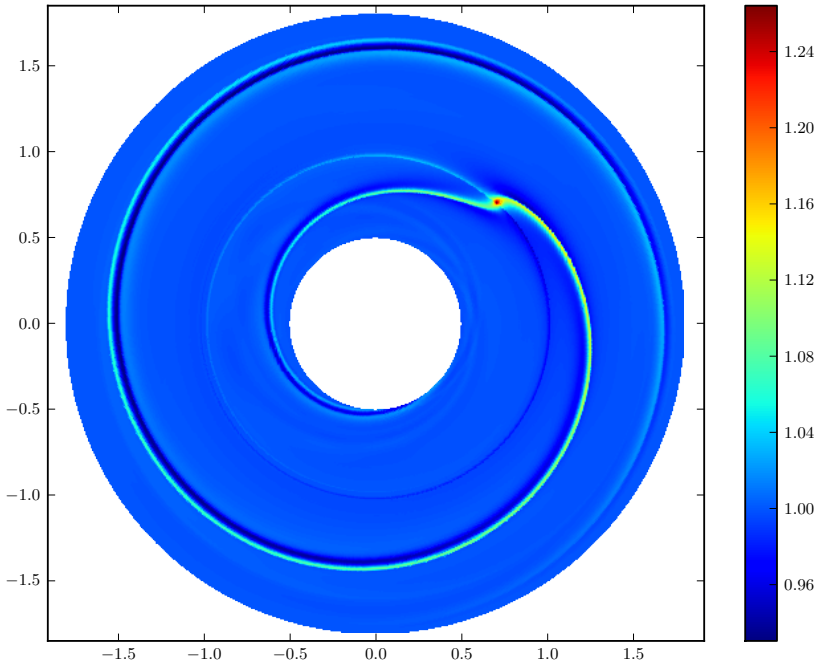

Figure 1.6: A $5M_{\oplus}$ planet embedded in a 2D disc with $H/r = 0.05$, with a kinematic viscosity of $\nu = 5.0 \times 10^{-6}$ and the entropy relaxation timescale (see section 2.6.4) has been set to 11 orbits. The disc is shown after 25 orbits. Note the distinctive spiral density wave pattern, and the density perturbation in the corotation region, which returns to its equilibrium value before encountering the planet again. The quantity shown is the perturbation to the equilibrium density, ρ/ρ_0. Wave reflection has been damped at the inner and outer boundaries (see section 2.5.1).

In a locally-isothermal disc, the entropy-related corotation torque tends towards its linear value, just as for a disc with rapid viscous evolution, the

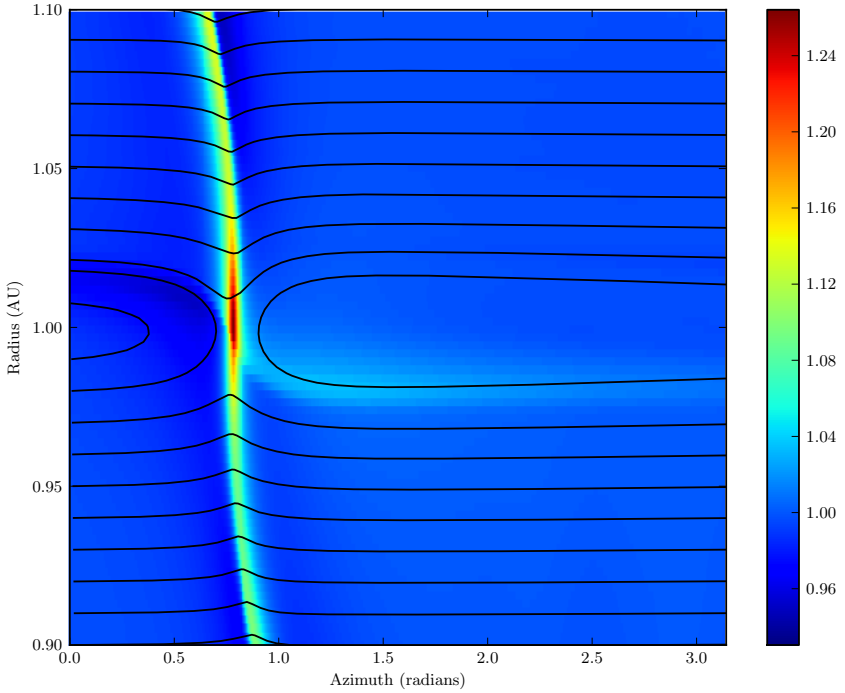

Figure 1.7: The corotation region of a disc with an embedded $5M_\oplus$ planet after 25 orbits. $H/r = 0.05$, with a kinematic viscosity of $\nu = 5.0 \times 10^{-6}$ and the entropy relaxation timescale (see section 2.6.4) has been set to 11 orbits. Horseshoe trajectories are plotted; note how material close to the planet librates. Note also the density perturbation confined to this region and the offset between the location of the planet and the 'centre' of the streamlines. The quantity shown is the perturbation to the equilibrium density, ρ/ρ_0.

vortensity-related corotation torque tends towards its linear value. In an adiabatic disc, the corotation torque saturates. For some values of viscosity and thermal diffusion, the total corotation torque reaches a maximum. Masset and Casoli (2010) and Paardekooper et al. (2011) have studied the transition between the isothermal and adiabatic regimes, and developed torque formulae to take into account partial or complete torque saturation.

Horseshoe Width and Morphology

A number of different prescriptions exist for defining the half-width of the corotation region (that is, the "horseshoe width") away from the planet. Paardekooper and Papaloizou (2009b) derive one such analytic expression of

$$\frac{x_s^2}{r_p^2} = \frac{16q}{3\pi h}\int_0^\infty \frac{K_0(r)r}{\sqrt{4r^2+b^2/h^2}} E\left(\frac{3r^2}{4r^2+b^2/h^2}\right)\mathrm{d}r, \tag{1.20}$$

where K_0 is the Bessel function, and E is the complete elliptic integral of the first kind, which they observe reduces in the limit of zero softening to

$$\frac{x_s}{r_p} \approx 1.68\sqrt{\frac{q}{h}}, \tag{1.21}$$

or in the case of $b \gg h$ to

$$x_s \sim \sqrt{\frac{8q}{3b}} r_p \tag{1.22}$$

These authors note that this is expected to reduce by a factor of $\gamma^{0.25}$ in the case of an adiabatic disc, and that an even further reduction can be expected due to back pressure from Lindblad wakes and other density features separated from corotation by a pressure scaleheight, H. Paardekooper et al. (2010) confirm this and derive the numerical result

$$x_s = \frac{1.1}{\gamma^{0.25}}\left(\frac{0.4}{b/h}\right)^{0.25}\sqrt{\frac{q}{h}}, \tag{1.23}$$

from 2D disc simulations, applicable for $b/h > 0.3$.

This same back pressure is the cause of the offset between the planet and the 'stagnation point' of the horseshoe streamlines, which Paardekooper and Papaloizou (2009b) find goes as $\sim br_p$ in their two dimensional simulations.

Zero-torque radii

Given an unsaturated outward corotation torque comparable to the inward Lindblad torque, the possible existence of *zero-torque radii* (also known as *convergence zones*) arises; locations in the disc, dependent on planet and disc properties, where the corotation torque exactly cancels the Lindblad torque and there is no resultant torque on the planet, and therefore no migration. Such locations could potentially act as planet 'traps', and catalyse the formation process by bringing raw materials for planet formation to one location (Cossou et al., 2013; Hellary and Nelson, 2012).

As the local disc structure may differ from the simple power-law prescription commonly assumed (due to, say, a massive planet opening a gap elsewhere in the disc), many local zero-torque radii may exist. Planets of differing masses will also have different zero-torque radii.

1.5.2 Type II migration

Gap-opening criterion

In the case of low-mass planets, the torque they exert on the disc is balanced by the pressure and viscous forces in the disc such that the disc density is not significantly depleted around the planet's location.

Lin and Papaloizou (1986a) noted that if the torque applied to the disc by the planet exceeds the capacity of the viscosity in the disc to transport angular momentum (in other words, exceeds the viscous torque due to disc spreading), then an annular gap will be 'carved' around the planet's orbital radius. Crida et al. (2006) refined this model, showing that a pressure torque also exists due to density waves launched by the planet that carry away some of the gravitational torque rather than depositing it locally. They showed that a gap will be opened if the following condition is satisfied;

$$\frac{3}{4}\frac{H}{r_{\mathrm{H}}} + \frac{50}{qR} \lesssim 1, \tag{1.24}$$

where $r_{\rm H} = r_p(q/3)^{1/3}$ is the planet's Hill radius and $R = r_p^2\Omega_p/\nu$ is the Reynolds number of the disc, determined by the disc's kinematic viscosity, ν. If we adopt the common alpha model for viscosity of Shakura and Sunyaev (1973), as described in section 2.1.1, the gap-opening criterion reduces to

$$\frac{h}{q^{\frac{1}{3}}} + \frac{50\alpha h^2}{q} \lesssim 1. \tag{1.25}$$

It should be noted that this is consistent with the requirement that $q \ll h^3$ in section 1.5.1 for the planet's perturbation of the disc to be small. For typical disc parameters of $h = 0.05$ and α of a few $\times 10^{-3}$, this corresponds to a requirement of a mass comparable to or greater than Jupiter's. In regions of the disc where the viscosity is expected to be much less (e.g. dead zones), a much lower mass would be sufficient.

Work by Muto et al. (2010) has shown that in the case where a planet remains on a fixed orbit for a long period (either artificially in a simulation where the planet has been held on a fixed orbit or naturally due to it being at or near a zero-torque radius), gap opening is possible when the quantity on the right hand side in equation 1.25 is some fraction of unity– potentially as low as 0.1– due to non-linear steepening of the density waves.

Typically, the half-width of a planetary gap is not much more than $2r_{\rm H}$. A planet that has opened a gap in its disc is shown in figure 1.8.

Migration

Building on their work described in the previous section, Lin and Papaloizou (1986b) noted that a planet which opened a sufficiently deep gap would be repelled by both sides of the gap and constrained to orbit in the gap centre. The migration of the planet is then controlled by the viscous evolution of the disc and occurs at the timescale of the same, $\tau_\nu = r_p^2/\nu$. If the planet is more massive than the disc outside the gap, then the planet will slow down the viscous accretion rate.

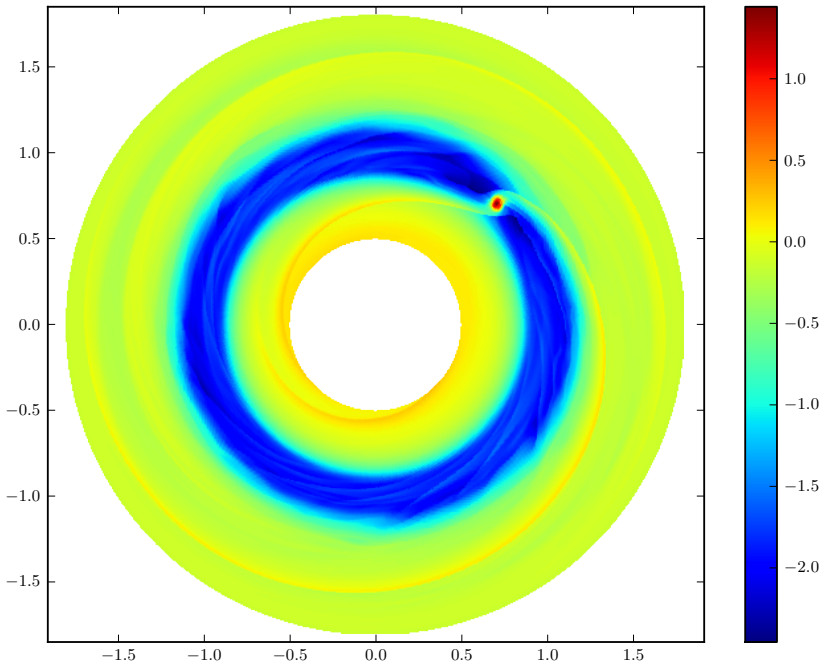

Figure 1.8: A $2M_J$ planet in a disc with $H/r = 0.05$ and a kinematic viscosity of $\nu = 5.0 \times 10^{-6}$ after 477 orbits. The quantity shown is the perturbation to logarithm to the base 10 of the density. Notice the depletion of the disc material in the region around the planet. Wave reflection has been damped at the inner and outer boundaries (see section 2.5.1).

1.5.3 Type III migration

A third regime of planetary migration was discovered by Masset and Papaloizou (2003). In this Type III migration (also known as *runaway migration*) regime, an inwardly migrating planet with a depleted gap preferentially moves material from the inner disc to the outer disc, experiencing a overall negative corotation torque which scales with the drift rate. This feedback effect between drift rate and corotation torque allows such migration to be extraordinarily rapid, varying the planet's semi-major axis by as much as 50% over a few tens of orbits. Typically, this type of migration occurs for Saturn-mass planets. This regime of migration is not discussed further in this thesis.

The regimes in which the three different types of migration operate is shown schematically in figure 1.9.

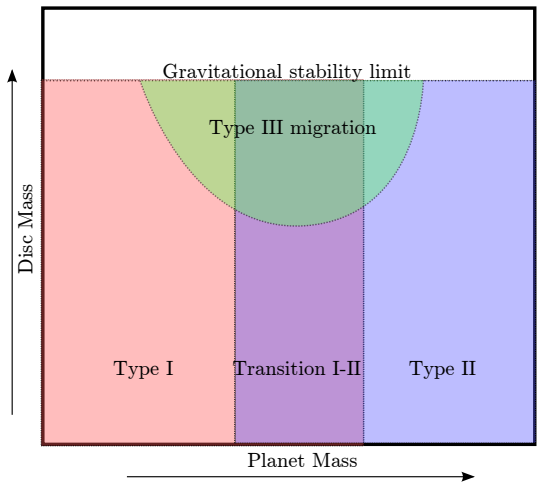

Figure 1.9: A schematic illustrating the different migration regimes' dependence on planet and disc mass. This schematic is after figures 12-14 by Masset and Papaloizou (2003). The transition region, where even very low mass planets can begin to deplete the corotation region, depends strongly on the disc aspect ratio. The transition region exists for $H/r = 0.03$, is narrower for $H/r = 0.04$ and does not exist for $H/r = 0.05$. Typical values for the 'peak' of the Type III regime are masses of a few $\times 10^{-4}$ solar masses.

1.5.4 Multiple planets

In much of the above discussion, the assumption has been that any disc will only have one planet interacting with it at any time. We know from observations, however, that multiple-planet systems are by no means uncommon, and we should expect protoplanetary discs to contain multiple forming planets. The precise evolution of such a disc would depend on the masses and locations of the planets, as well as the properties of the disc, and has been investigated by e.g. Hellary and Nelson (2012). Complex behaviours can occur, such as planets migrating into resonance through disc interactions and then migrating further in resonance (Snellgrove et al., 2001), or less massive planets migrating under the influence of the density perturbations of a massive planet. Less massive planets may also be scattered out of the system (e.g. Fogg and Nelson, 2009).

As described earlier, planets can also excite each other's eccentricities (e.g. Cresswell and Nelson, 2006), against disc eccentricity damping, reaching higher eccentricities than would otherwise be possible. For the work in this thesis, I have investigated single planets in protoplanetary discs, but it should be noted that the higher eccentricities I consider might be connected with the presence

of other embedded planets.

1.5.5 Eccentricity and inclination

Typically, the interaction between the disc and an embedded protoplanet is to damp eccentricities (Goldreich and Tremaine, 1980; Papaloizou and Larwood, 2002). However, Goldreich and Sari (2003) suggest that a planet's eccentricity might be excited by interactions with the disc at Lindblad resonance locations and at corotation in the absence of any other planets in the disc, because corotation torques that damp eccentricities might be saturated.

In recent work, Bitsch and Kley (2010) found an attenuation of corotation torque for a $20M_\oplus$ planet embedded in a protoplanetary disc with $H/r = 0.037$, in 3D simulations of radiative, viscous discs with a surface density[13] profile of $r^{-1/2}$, to the extent that migration reversed direction from outward to inward at an eccentricity of $e = 0.1$.

Particularly with what we know of zero-torque radii as described above, understanding the dependence of the corotation torque on planetary eccentricity is vital to a qualitative understanding of the evolution of eccentric planets; this is the question addressed by the author in chapter 3. In the next chapter, the computational tools we will use to tackle this problem are introduced.

[13]See chapter 4 for a discussion on the difference between midplane and surface density.

Summary

- The currently known population of extrasolar planets includes close-in massive planets ('hot Jupiters') which suggest post-formation migration, and systems of multiple planets which suggest planet-planet interactions occur during the formation process in many systems. Such interactions are known to excite eccentricities.
- Protoplanetary disc are believed to exist for $\sim$ 6Myr around sun-like stars and evolve through viscous evolution and photoevaporation.
- Two widely-cited models of planet formation exist; the core accretion model and gravitational instability model.
- Disc-planet interactions fall into the categories of type I migration, for low-mass planets, type III migration for intermediate-mass planets and type II migration for massive planets that open a gap.
- The direction of type I migration is dependent on the vortensity and entropy gradients in the corotation region and recent work has suggested it may attenuate for non-zero eccentricity.

Chapter 2

Numerical Methods

In this chapter, I describe the equations of hydrodynamics and outline in principle two different numerical methods for their solution; the finite-difference advection method used by the NIRVANA *code and the finite-volume Godunov scheme used by the* PLUTO *code. I then present all the necessary elements of a hydrodynamic disc simulation.*

Please note that both of these codes have been developed by the authors cited in this chapter, and that my work consisted of modifying these codes with the appropriate boundary conditions, gravitational potential, thermodynamic model and so on for the problems of interest to me, described in chapters 3, 4 and 5.

2.1 The Equations of Hydrodynamics

For a fluid with density ρ, pressure P, velocity $\vec{v}$ and total internal energy per unit volume e, the following system of equations can be derived, following any standard undergraduate text, from the requirements of conservation of mass, momentum and energy respectively;

$$\frac{\partial \rho}{\partial t} + \nabla \cdot (\rho \vec{v}) = 0, \tag{2.1}$$

$$\frac{\partial}{\partial t}(\rho \vec{v}) + \nabla \cdot (\rho \vec{v}\vec{v}) = -\nabla P - \rho \nabla \Phi, \tag{2.2}$$

$$\frac{\partial e}{\partial t} + \nabla \cdot (e \vec{v}) = -P \, \nabla \cdot \vec{v} + \mathcal{Q} - \Lambda, \tag{2.3}$$

where Φ is the external potential acting on the fluid and $\mathcal{Q}$ and Λ are heating and cooling terms. The system of equations is closed by an equation of state. For our purposes, where finite molecular size and inter-molecular attraction can be neglected, the ideal gas law is perfectly acceptable and can be written as

$$P = \rho e(\gamma - 1). \tag{2.4}$$

2.1.1 Viscosity

The redistribution of angular momentum by viscosity in a protoplanetary disc is a key process governing its long term evolution, a well as one that is necessary to unsaturate the corotation torque as discussed in chapter 1. After Landau and Lifshitz (1987), we can make use of summation notation to express the effect of viscosity as

$$\frac{\partial}{\partial t}(\rho v_i) = \frac{\partial}{\partial x_k} \sigma'_{ik}, \tag{2.5}$$

where σ'_{ik} is the viscous stress tensor defined as

$$\sigma'_{ik} = \eta \left(\frac{\partial v_i}{\partial x_k} + \frac{\partial v_k}{\partial x_i} - \frac{2}{3} \delta_{ik} \frac{\partial v_l}{\partial x_l} \right) + \zeta \delta_{ik} \frac{\partial v_l}{\partial x_l}, \tag{2.6}$$

with η being the dynamic viscosity, related to the kinematic viscosity, ν, by $\nu = \eta \rho$. Analogous expressions can be derived in other coordinate systems; for curvilinear coordinates, for example, see Landau and Lifshitz (1987, p.48).

Viscosity is also responsible for viscous energy dissipation; that is, the mechanical work done by viscous forces which is converted to internal energy. This acts as a heating term.

The α-model of viscosity

Hydrodynamic eddy turbulence has been proposed as a means of producing greater viscosity in accretion discs than is possible by considering purely molecular viscosity as discussed in section 1.2.4. Without detailed knowledge of these turbulent processes, Shakura and Sunyaev (1973) used a dimensional argument to determine that such turbulence should depend on the height of the disc, H, as the characteristic mean scale of such turbulent eddies and the speed of their propagation, αc_s, where α is a dimensionless constant and c_s is the sound speed in the disc. From this, we have the α model of viscosity, widely used in disc simulations;

$$\nu = \alpha c_s H. \tag{2.7}$$

Under this scheme, typical viscosities used in disc simulations correspond to α-values in the range $10^{-4} - 10^{-2}$.

2.2 Solution Methods

The equations of hydrodynamics are formally a set of coupled hyperbolic partial differential equations (which become mixed hyperbolic-parabolic with the introduction of viscous diffusion). For this work, two distinct types of solution method were employed; the finite difference, advection type solution used in the NIRVANA code and the finite volume, Godunov method solution used in PLUTO. A comparison of the finite difference method as compared to the finite volume method is presented in this section. A more thorough comparison, including the finite element method not discussed in this thesis, has been published by Peiró and Sherwin (2005).

Both these codes are what we call grid-based, *Eulerian* codes, meaning they

operate on a grid of discrete cells through which material is advected, the size of which may be constant across the domain, may vary according to some mathematical function (logarithmic grid cell sizing, for instance) or be defined such that the area of interest is resolved by a greater resolution. These codes are distinct from the so-called *Lagrangian* codes, in which the advection of the fluid changes the grid, or in which there is no grid all (e.g. the smoothed-particle hydrodynamics (SPH) paradigm). Such schemes are not discussed in this thesis.

Before introducing the two solution methods, it is necessary to briefly introduce the concept of *operator splitting*, to which the later discussion refers.

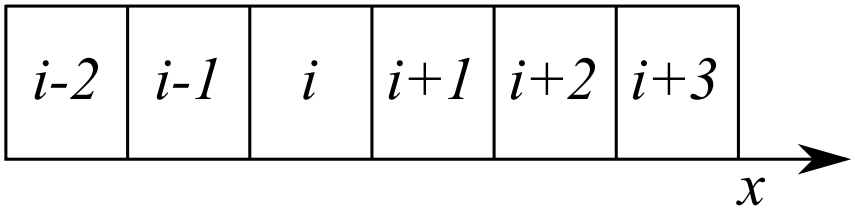

Figure 2.1: A schematic of cells in a hydrodynamic simulation, referred to in the text; in reality, the cells may very in size as a function of x, and there are likely to be multiple dimensions.

2.2.1 Operator splitting

If we consider the equation

$$\frac{\partial u}{\partial t} = Au + Bu, \tag{2.8}$$

where A and B are differential operators, it can be shown that treating the operators separately and then recombining them can provide an acceptable approximation to the true solution, as well as being computationally much easier.

As a simple, linear example of this principle, we can consider the ordinary differential equation,

$$\frac{\mathrm{d}u}{\mathrm{d}t} = 1 + u, \qquad u(0) = 1, \tag{2.9}$$

with the simple(st) operator splitting algoritm,

$$\begin{aligned} \frac{1}{2}\frac{\mathrm{d}u_A}{\mathrm{d}t} &= u \qquad \Longrightarrow \qquad u_A = \exp(2t), \\ \frac{1}{2}\frac{\mathrm{d}u_B}{\mathrm{d}t} &= 1 \qquad \Longrightarrow \qquad u_B = 1 + 2t. \end{aligned} \tag{2.10}$$

We then integrate the original equation to a value t either by using the solution u_A between 0 and $t/2$ and then u_B between $t/2$ and t, or by using the solution u_B between 0 and $t/2$ and then u_A between $t/2$ and t[1]. The two different solutions are shown in figure 2.2 along with the true solution.

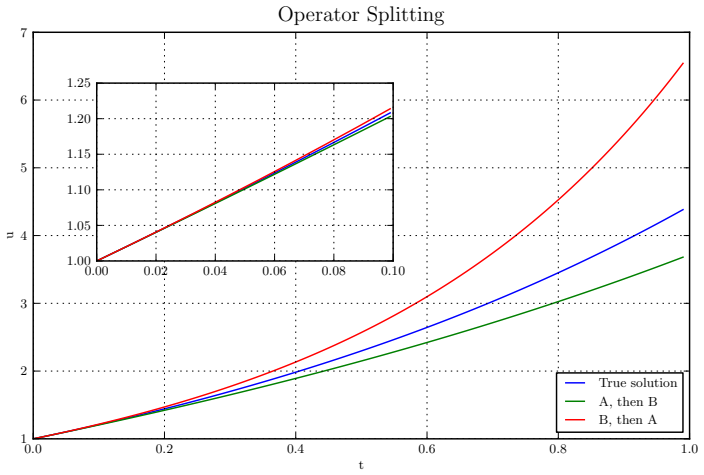

Figure 2.2: A comparison of the analytic solution to equation 2.9 with the two reconstructions of this solution using the simple operator splitting algorithm descriibed in the text. Note that for small t, the reconstructions provide a good approximation to the true solution.

While this is only a simple example, it serves to illustrate that for sufficiently small time integrations, it is possible for even a very simple operator splitting algorithm to give a reasonable accurate approximation to the correct solution.

Operator splitting is often used to extend a 1D hydrodynamic solution algorithm to higher dimensions, by splitting the operators of the different spatial dimensions and treating them separately. It is also used in the advection-type codes to separate the pressure source term from the simple advection equation.

[1]More sophisticated reconstruction schemes are also possible in practice, with the timestep being broken into more than two parts.

2.2.2 Advection solvers

The advection type method employed by the NIRVANA code can be understood by noting that the fluid equations can be rewritten as independent advection equations of the form

$$\frac{\partial q}{\partial t} + \frac{\partial}{\partial x}(qu) = 0, \tag{2.11}$$

where q is any of the hydrodynamic conserved quantities (mass, momentum, energy), with additional source terms due to pressure forces and external potentials.

Many algorithms exist capable of solving problems of this kind. Here, we consider finite-difference codes, where the differences between q of a cell and of its neighbours at one timestep are used to generate the q at a later time. Typically, some kind of *flux limiter* is used to ensure that higher-order schemes do not yield an unphysically large flux between one cell and another near discontinuities.

We can then solve the equations using the technique of operator splitting; we first solve the advection equations for all the hydrodynamic conserved quantities (mass, momentum, energy), and then separately solve for the source terms.

In multiple dimensions, advection in different directions can either be treated separately by operator splitting the different dimensions and treating each as a one dimensional problem (thereby allowing the trivial extension of algorithms developed for one dimension) or by using an algorithm which solve the multiple dimensions in the same process (with the associated complexity of designing and implementing a suitable algorithm).

It is important to note that in this scheme, all propagation is through advection at the advection speed of the disc material; this is the crucial difference between this method and that described in the next section.

2.2.3 Godunov solvers

The hydrodynamic equations 2.3 can be rewritten in the form

$$\frac{\partial \vec{q}}{\partial t} + J\frac{\partial \vec{q}}{\partial x} = 0, \tag{2.12}$$

where $\vec{q}$ is a vector of hydrodynamic conserved quantities, J is the Jacobian matrix to allow the partial derivatives with respect to space and time to operate on the same quantity and where the system has also been reduced to one dimension, x, for clarity. Note that rather than considering, and advecting, each of the hydrodynamic conserved quantities separately, we are now considering the state of the system as a whole.

If we find the eigenvalues and eigenvectors of this Jacobian, we could decompose any state vector, $\vec{q}$, (corresponding to any state of the system), into components along the eigenvectors. The evolution of the set of eigenvectors (the 'eigenstates') is determined by a diagonal Jacobian– in other words, each of the eigenvector components of the decomposition evolves independently, each at its own velocity given by its eigenvalue.

It can be shown that the eigenvalues in the case of the one dimensional set of hydrodynamic equations including an energy equation are $u - c_\mathrm{s}$, u and $u + c_\mathrm{s}$ where $c_\mathrm{s} = \sqrt{\frac{\gamma P}{\rho}}$, the adiabatic sound speed (cf. equation 1.3).

In our advection scheme described in the previous section, we propagated all quantities at the velocity of material advection, u, *neglecting* the sound waves propagating backwards and forwards at velocities of $u - c_\mathrm{s}$ and $u + c_\mathrm{s}$ respectively. Treating the sound waves correctly requires a different approach, Godunov's method, outlined here but described more thoroughly by LeVeque (2002) and in Toro (2009).

Consider a boundary between two cells. On one side of this boundary, the hydrodynamic conserved quantities have values $\vec{q_1}$ and on the other, $\vec{q_2}$. This discontinuity is an example of a *Riemann problem*. Numerous algorithms, described in detail by the authorities referenced above and not discussed further here, exist to solve the Riemann problem at the boundary of two cells including the Roe solver, the HLL family of solvers and the Piecewise Parabolic Method. This solution consists of a prescription for how the state vectors, $\vec{q}$ evolve as a function of time around the boundary. As time goes on, the solution will propagate further from the boundary, forwards and backwards as shown schematially in figure 2.3. We cannot allow this solution to propagate

to the point where it co-exists with a solution from an adjacent boundary (as the two solutions were developed without knowledge of each other), and so this provides us with a natural limit to the length of a timestep, illustrated by the dashed circle in the figure.

Having propagated our locally derived solutions away from the boundaries as far as we can, we use the current composition of each cell (consisting of, in 1D, a region modified by the solution from the left boundary, a region unmodified by either boundary and a region modified by the solution from the right boundary) to generate a new state. We then repeat the algorithm for the required number of iterations.

The development of the algorithms to appropriately solve the Riemann problem at the boundary is a non-trivial exercise and the details are beyond the scope of this thesis.

The major advantage of this scheme of solver is that shocks, contact discontinuities and other small-scale flow features are preserved sharply. A notable disadvantage is that it can be difficult to select and implement boundary conditions that correctly balance external forces (e.g. gravity), with gas pressure (Zingale et al., 2002).

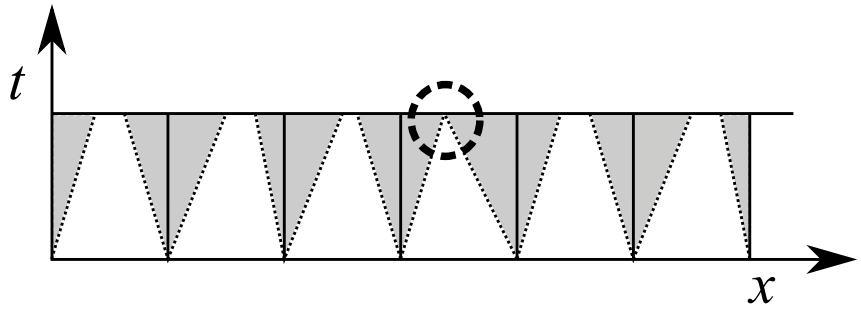

Figure 2.3: In Godunov's method codes, a solution is computed to the Riemann problem at each cell boundary. The solution is them propagated into the neighbouring cells for a time determined by requirement that solutions from neighbouring cells should never overlap (the dotted circle), as they were derived without reference to each other. This sets a natural limit on the length of a timestep in such a code.

2.2.4 The Courant-Friedrich-Lewy (CFL) condition

To maintain numerical stability in a grid-based difference code, we must ensure that the timestep with which we integrate the system is sufficiently small that information cannot propagate beyond a single cell in a single timestep. More precisely, Courant et al. (1928)[2] showed that, depending on the algorithm, a necessary but not necessarily sufficient condition for the solution of the discretised difference equation to converge to the solution of the partial differential equation is that

$$\frac{u\Delta t}{\Delta x} < c_{\max}. \tag{2.13}$$

This is known as the Courant-Friedrich-Lewy (CFL) condition. Usually, the timestep is chosen such that $\frac{u}{c_{\max}}\frac{\Delta t}{\Delta x}$ is less than a chosen *Courant factor*, which must be less than 1.

For simulations in more than one dimension, the constraint is more strict;

$$\Delta t \sum_{i=1}^{N} \frac{u_{x_i}}{\Delta x_i} < c_{\max}, \tag{2.14}$$

where $i = 1, 2, 3$ are the different spatial dimensions.

Naïvely, assuming $\frac{u_{x_i}}{\Delta x_i}$ is constant for all i, this reduces to

$$\frac{Nu\Delta t}{\Delta x} < c_{\max}, \tag{2.15}$$

where there are N dimensions. This yields a maximum Courant factor of $1/N$.

It is also possible to increase the timestep by careful treatment of the material transport velocities. Simulating in the corotating frame as described below is one such treatment; the FARGO algorithm described in section 2.2.6 is another.

[2] An English translation has since been published by Fox (1967).

2.2.5 Corotating frame

Simulations in polar coordinates are often performed in a frame of reference rotating with the same angular velocity as some point of interest in the grid (in our case, the planet, or the guiding centre of the planet's epicyclic motion); this helps ensure that the fluid velocities are minimised around the area of interest and so the code suffers from a smaller numerical diffusitivity.

The rate of change of a vector function, $\vec{F}(t)$ in a rotating reference frame will depend not only on the change of the function with time, but also with the change of the coordinate system of the function with time;

$$\left.\frac{\mathrm{d}\vec{F}}{\mathrm{d}t}\right|_{\text{intertial}} = \left.\frac{\mathrm{d}\vec{F}}{\mathrm{d}t}\right|_{\text{rotating}} + \vec{\Omega} \times \vec{F}. \tag{2.16}$$

When acceleration is expressed in the rotating frame, for example, the fictitious Coriolis and centripetal forces appear; these are added separately to the hydrodynamic equations.

2.2.6 The FARGO algorithm

The FARGO[3] algorithm was developed by Masset (2000) to increase the time step in disc simulations limited by rapid orbital motion at the inner boundary. Simulating a disc in polar coordinates involves two advection steps, separated by operator splitting; one in the radial direction and the second in the azimuthal direction.

The FARGO algorithm divides the azimuthal advection step further into two: First, an azimuthal transport step with the velocity $v_\theta - \overline{v_\theta}$, where v_θ is the azimuthal velocity at a cell and $\overline{v_\theta}$ is the average azimuthal velocity of the radial annulus of the cell. Second, an additional azimuthal advection step a velocity of $\overline{v_\theta}$; this is effectively 'rotating' the entire annulus uniformly by the average azimuthal velocity after using the deviations from this velocity to move material between cells within the annulus.

[3]Standing for "Fast Advection in Rotating Gaseous Objects".

The result is a greater timestep because the second step of rotating the solution amounts to a straightforward copying of information from one grid cell to another, and a smaller numerical diffusivity. The validity of the FARGO model was tested and confirmed more recently by Kley et al. (2012), who tested a series of codes with and without the FARGO algorithm.

2.3 The Codes

2.3.1 The NIRVANA code

The NIRVANA code, developed by Ziegler (1998) is a finite-different magnetohydrodynamic code. It is based in principle on the ZEUS code as developed by Stone and Norman (1992a), which included magnetohydrodynamic functionality (Stone and Norman, 1992b) and a radiative solver (Stone et al., 1992), and later the capacity for parallelisation (Norman, 2000).

NIRVANA allows simulations to be run in one, two or three dimensions and in different coordinate systems. Magnetohydrodynamics may be included. Simulations may be run in a rotating frame or an inertial frame.

The version of the code used for the work described in this thesis should not be confused with the redesigned code of the same name released by the original developer (Ziegler, 2008). The new version features adaptive mesh refinement to allow greater resolution in regions of interest, and a Godunov-type solver.

2.3.2 The PLUTO code

The PLUTO code, developed by Mignone et al. (2007), is a shock-capturing Godunov-type code designed to simulate hypersonic flows in one, two or three dimensions with different coordinate systems. The code supports simulations using just hydrodynamics, with relativistic hydrodynamics, with magnetohydrodynamics or with relativistic magnetohydrodynamics. The code can be configured for use with adaptive mesh refinement, and the FARGO algorithm is included. Simulations may be run in a rotating frame or an inertial frame.

Radiative hydrodynamic modules for PLUTO have been developed by Flock et al. (2013), building the flux-limited diffusion approach of Commerçon et al. (2011) and including irradiation, and by Kolb et al. (2013).

2.4 Parallelisation

Parallelisation is the name given to the process whereby large, computationally expensive calculations are distributed among many computer processors. In the case of our simulations, the domain of a hydrodynamic simulation can be broken down into a number of regions. Each region is then integrated independently, in parallel, yielding a significant increase in speed. In order to integrate cells at the boundary of each computational domain, information about the state of cells in the domain of another processor is needed; this information is exchanged at the end of each timestep and stored in so-called *ghost cells*.

For example, in figure 2.1, cells $i-2$, $i-1$ and i might be integrated by processor n and cells $i+1$, $i+2$ and $i+4$ might be integrated by processor $n+1$. In an algorithm with two ghost cells (that is, one where data about two neighbouring cells is needed for each integration) the current state of cells $i-1$ and i would be sent from processor n to $n+1$ to be used but not modified. Similarly, the values of cells $i+1$ and $i+2$ would be sent to processor n.

It is important when using parallelised codes to ensure that the speed increase from the smaller domain size is not negated by the increased time required to pass data between processors. Typically, the number of ghost cells should be much smaller than the number of cells in each processor's domain.

A very commonly used standard for parallelisation, which allows communication between processors, is the *Message-Passing Interface* (MPI), described by e.g. Gropp et al. (1999) and implemented in a large number of compilers and languages. In this paradigm, each processor runs the same program, but each will be assigned a different *processor rank* which can be stored in a program variable. Processors can, for example, send messages to other processors (MPI_SEND), wait to receive such messages before continuing (MPI_RECV) or wait until all processors reach the same stage in the computation (MPI_BARRIER).

2.5 Boundary Conditions

The algorithms discussed above all use the current state of the grid to calculate the state at a later time; specifically, the nearest neighbours of a cell are used to determine how it evolves. At the boundaries, however, we have no surrounding cells on one side, which is a problem typically dealt with by adding more ghost cells at each boundary. These are similar to those described above in the section on parallelisation, but for which we prescribe a state based on the behaviour we want at that boundary.

The number of ghost cells required depends on the number of neighbour cells required by the algorithm being used and it should be noted that not all variables of state need to share the same boundary conditions. Similarly, boundary conditions in different dimensions are independent. Typically, in simulations of the kind in this thesis, we require that the edges of a simulation do not strongly influence the area of interest.

If we consider, as an example, a variable q on a one-dimensional grid of cells $x_1, x_2, x_3, ..., x_N$, where x_1 and x_N are ghost cells, we can describe a number of ways of handling boundaries:

Periodic Where $q(x_1) = q(x_{N-1})$ and $q(x_N) = q(x_2)$. This has the effect that material leaving the domain through one boundary enters again through the other. In polar coordinates, for example, this would be used for the azimuthal coordinate.

Extrapolation We can set the value of $q(x_1)$, thereby imposing a *zero-gradient condition* at that bounday. Similarly, we can use the gradient of q between $x = x_2$ and x_3 to extrapolate an appropriate value for x_1 by linear regression; or we can use a higher order scheme to extrapolar a regression of a higher power, or fitting some function (an exponential decay, for example).

Hydrostatic We can choose our boundary to satisfy the hydrostatic equilibrium equation, ensuring that the edge cells remain unchanged after the integration;

$$\nabla P = -\rho \nabla \Phi. \tag{2.17}$$

Reflecting Where material leaving through one boundary immediately enters again through the same boundary; its velocity perpendicular to that boundary is reversed while its other properties are unmodified.

Outflow Not strictly a boundary condition but rather a modifier to a boundary condition, we may impose an outflow condition: Typically with the zero-gradient boundary described above, we require no material to enter the grid from outside and so we impose the additional condition that if the velocity in the ghost cell, x_1, is positive, it is set to zero. Similarly, a negative velocity in cell x_N would be set to zero. Velocities directed out of the computational domain at either boundary would be unaffected.

We might also employ damping regions employed below.

2.5.1 Damping regions

With reflecting boundary conditions, waves launched by the planet in the disc will be reflected back into the domain of interest in a non-physical way. In order to minimise this effect, we can use damping or *wave-killing regions*, as described by de Val-Borro et al. (2006), close to the boundaries. With this technique, physical properties (velocity, density, pressure) generically represented here by x are damped in the wave-killing regions according to

$$\frac{\mathrm{d}x}{\mathrm{d}t} = -\frac{x - x_0}{\tau} R(r), \tag{2.18}$$

where x_0 is the initial value of x (that is to say, the equilibrium value in the case without the presence of the planet), τ is the damping timescale (typically some fraction of the orbital period at the boundary) and $R(r)$ is a parabolic function which is one at the boundary and zero at the edge adjoining the rest of the computational domain.

2.5.2 Internal boundaries

In the boundary cells, properties are changed as necessary to ensure that the simulation behaves as desired in the region we are interested in. It is some-

times necessary to form similar modifications to cell properties away from the boundary, in order to capture relevant physics. A pertinent example might be an imposed change in cell density by a subroutine modelling accretion of disc material near a planet. These are sometimes known as *internal* boundaries, to indicate the prescribed nature of the changes in cell properties that take place there.

2.6 Thermodynamic Models

In order to accurately solve the evolution of the disc, we need to select an appropriate thermodynamic model, being aware that more accurate models come at the cost of greater computational complexity. A number of such models are reviewed in this section in the context of disc simulations.

2.6.1 Locally isothermal

If we assume T is a simple function of R, we can trivially use the ideal gas law to relate P and ρ, with $\gamma \to 1$. This is conceptually simple and removes the need to integrate the energy equation. However, it assumes a very rapid thermal relaxation timescale, such that material returns to its equilibrium temperature instantaneously. In regions with a high optical depth, this will not be a realistic model, as relaxation back to the appropriate equilibrium temperature at a given radius in the disc will take much longer. The instant relaxation also means that the entropy-related corotation torque in such a disc will reach towards its smaller, linear value.

2.6.2 Adiabatic

If the temperature distribution is more complex, we must solve the fluid energy equation given above. By doing this, we are simulating an adiabatic (or isentropic) disc; material remains at the same temperature as it is moved around the grid, with no heating or cooling due to its environment. This corresponds to an infinitely long thermal relaxation timescale, which is unlikely to be physically realistic at all disc radii. For our work, an adiabatic disc means

the corotation torque will saturate as the corotation region becomes mixed, as described in chapter 1.

The adiabatic exponent, γ, defined as the ratio of the specific heat at constant pressure C_p to the specific heat at constant volume C_v, is related to the number of degrees of freedom f of the fluid by

$$\gamma = \frac{C_p}{C_v} = \frac{f+2}{f}. \tag{2.19}$$

Typical values in the literature for disc simulations are between $\gamma = 7/5$ (assuming a diatomic molecule) and $\gamma = 5/3$ (assuming atomic gas).

2.6.3 Radiation transport

In a real protoplanetary disc, the temperature profile is determined by the balance of viscous heating, radiative heating and cooling. Irradiation from the central star should also be included. In an attempt to reproduce this computationally, it is possible to transport energy through radiation in the disc. The flux-limited diffusion model is one approach as implemented by, among others, Commerçon et al. (2011). Such techniques are computationally intensive. We describe such a scheme in chapter 5.

2.6.4 Entropy Relaxation

As a computationally efficient alternative to a full radiative transfer model, we can implement an adiabatic disc with a simple Newtonian cooling scheme that constantly relaxes the entropy (or temperature) in the disc back toward its initial value on a specified time scale, $\tau_{\rm ent}$. The value of $\tau_{\rm ent}$ can be chosen through successive trials to, for instance, optimally unsaturate the corotation torque. Given that P/ρ^γ is a constant along each adiabat and is therefore a function of entropy, s, we can use the function

$$K(s) = \frac{P}{\rho^\gamma}, \tag{2.20}$$

and integrate it at each timestep according to

$$K_{i+1}(s) = K_i(s) - (K_i(s) - K(s_0))\frac{\Delta t}{\tau_{\rm ent}}, \tag{2.21}$$

where $K(s_0)$ is the initial value of the entropy function and Δt is the time-step size. From this, the internal energy density is recalculated using the ideal gas law

$$e = K(s)\frac{\rho^\gamma}{\gamma - 1}. \tag{2.22}$$

This allows us to strike a balance between the instantaneous thermal relaxation of a locally isothermal disc model and the infinitely slow thermal relaxation time of a pure adiabatic disc, while at the same time avoiding the complexity of implementing a full-blown radiative transfer scheme.

2.7 Our Simulations

There are a number of other features that we make use of in our simulations; in this section, these are introduced and discussed.

2.7.1 Potential

We use the following prescription for the gravitational potential that the disc evolves under, where the three terms are, respectively, the potential of the central star, the potential of the planet and the indirect term due to the centre of the coordinate system being at the centre of the central star and not at the centre of mass of the system;

$$\Phi = -\frac{GM_*}{r} - \frac{Gm_p}{d} + \frac{Gm_p}{r_p^3}\vec{r_p}\cdot\vec{r}, \tag{2.23}$$

where r is the magnitude of the distance to the disc element $\vec{r}$, where $\vec{r} = (x, y, z)^{\rm T}$, and $d = \sqrt{(x - x_p)^2 + (y - y_p)^2 + (z - z_p)^2 + b}$ is the distance be-

tween the planet and the disc element, where b is the so-called 'softening' term. In 2D simulations, this softening accounts for the three dimensional nature of the real disc and should be some fraction of the scale height ($b = 0.4h$ has been found to agree well with 3D simulations and has been used by, e.g. Paardekooper et al. (2010)). In 3D simulations, the softening should be on the order of a grid cell and serves only to prevent numerical singularities. Kley et al. (2009) has suggested the use of a cubic potential with a characteristic softening for problems in 3D to accurately model disc material behaviour close to the planet; this is not employed in this work.

2.7.2 Accretion model

In order to form gaps around massive planets in a disc in a self-consistent manner, we can allow a small embedded planetary core to accrete mass from the surrounding disc within the Hill radius. Material closer to the planet can be accreted at a greater rate than that further away. The rate of accretion is chosen to allow growth to take place sufficiently slowly to not significantly perturb the disc but rapidly enough to take place within the limits set by the computational resources available. This approach is after that of Kley (1999), who finds that for kinematic viscosities of $\nu > 1 \times 10^{-6}$, the accretion timescale is less than that of the viscous evolution of the disc[4].

We describe such a model in section 5.5, where we implement it into the PLUTO code.

2.7.3 Density floor

We typically include a density floor to avoid very low density regions causing high velocities and so a small maximum timestep. The value of this is usually chosen to be sufficiently small that any remaining mass at this level will have a negligible effect on the rest of the system.

[4]Note that kinematic viscosity has dimensions $\frac{\mathrm{L}^2}{\mathrm{T}}$ and that viscosities in this thesis are given in code units; if $r = 1$ corresponds to 1 AU, then ν has units $\frac{\mathrm{AU}^2}{2\pi \times \mathrm{years}}$.

2.7.4 Hill sphere exclusion

Disc material very close to the planet will be bound to it gravitationally, or be accreted. In either case, it will not apply a torque on the planet. Rather than model the interactions between the planet and nearby material, which would require a much higher resolution, we simply exclude all material within the Hill sphere when calculating the torque experienced by the planet. As the movement of the planet through the grid (whether due to epicyclic motion in the corotating frame or due to orbital motion in the inertial frame) may cause grid cells to be suddenly counted or not counted as they move inside or outside this limit, we implement a scheme such that the torque from all cells is weighted by

$$f = 1 - \exp\left(-\frac{d^2}{2s^2}\right), \tag{2.24}$$

where d is the distance from the planet to the cell in Hill radii and s was chosen such that average torque was comparable to the case with no scale factor. A good value was found to be 0.5, by comparing the torque on planets on circular orbits using both this prescription and a binary torque inclusion/exclusion model.

2.8 Disc simulations

Having described the principles and components of a hydrodynamic protoplanetary disc simulation, I discuss in this section the context of those simulations in terms of what is currently possible and the compromises we must make in the interests of efficient use of available computational resources.

There are a number of approaches we can use to model planets in protoplanetary discs. In all cases, there is a trade-off between speed and complexity.

N-body simulations can simulate a planetary system evolving under gravity for many millions of orbits, with the disc (if modelled) assumed to be azimuthally symmetric and being represented by a simple one-dimensional viscous evolution model. Such a model can calculate the torques applied on both the

planet and the disc and effectively handle realistic gap opening and type II migration. Modelling type I migration, however, requires precise heuristics to allow the torque on the planet to be calculated given the disc conditions. This type of model has been used by Fogg and Nelson (2007) and Hellary and Nelson (2012), among others, and is currently the only way we can generate a statistically significant number of artificial planetary systems to test against observations.

To increase the physical realism, we can use a two-dimensional hydrodynamic disc model, in which our planets move under the action of an N-body solver and the disc material is modelled as a fluid. This fluid (or continuum) approximation is acceptable as long as the length scales we are interested in (AUs) are much greater than the molecular interaction scale.

Planets now distort the disc by the effect of their gravity on the disc. A softening parameter (discussed in section 2.7.1) is used to allow a 2D model to represent a 3D disc; the details of this model must be tuned to match 2D simulations. A canonical example of such a model is that of Nelson et al. (2000), who ran simulations of Jovian mass plants in locally isothermal protoplanetary discs over thousands of orbits at a resolution of up to 130×384 ($N_r \times N_\phi$) with three different hydrodynamic codes, and found inward migration occured on a timescale of $\sim 10^4$ years.

A final option is to run a simulation in three dimensions, with the disc modelled using hydrodynamic equations, with the associated extra computational cost of the extra dimension. It is important to note that at any size scale, the resolution of the simulation must be sufficiently high that the relevant physical features are resolved. An investigation of the corotation region, for instance, must at a minimum resolve the corotation region with enough cells to obtain meaningful results. Such global 3D simulations include those by, for example, Bitsch and Kley (2010).

It is possible to simulate a smaller region of a disc for a longer time and to a higher degree of complexity, but such models must be carefully validated against global models to ensure the behaviour is the same (Nelson and Gressel, 2010).

In addition to increasing the number of dimensions, more physics can increase the computational complexity of the problem being tackled. An alpha viscosity

model, for instance, is much less computationally intensive than modelling the disc processes such as the magneto-rotational instability believed to give rise to the effective viscosity in the disc. Similarly, a simple Newtonian cooling approximation allows a simulation to run much quicker than a full radiative disc model, but at the risk of giving less physically realistic results.

Summary

- The equations of hydrodynamics are a set of coupled partial differential equations, closed by an equation of state.
- They can be solved numerically in a number of ways relevant to this thesis; by advection type codes like NIRVANA or by Godunov scheme codes like PLUTO. The latter have the ability to capture density features more precisely, but suffer from temperamental boundaries.
- A number of thermodynamic models exist that can be used to prescribe appropriate behaviour for the evolution of the thermal structure of the disc, including the model of entropy relaxation.

Chapter 3

The Corotation Torque for Eccentric Planets

In this chapter, the first of the projects that make up my PhD is presented; an investigation of the attenuation of the corotation torque with increasing eccentricity. The simulations are described and then the results presented and discussed. An empirical relation between the eccentricity and the corotation torque is derived.

This work has been published in the Monthly Notices of the Royal Astronomical Society by Fendyke and Nelson (2014) and this chapter closely follows that paper.

In section 3.1 we define the aims and scope of the investigation; in section 3.2 we remind the reader of the relevant pieces of background information from the introductory chapters; in section 3.3 we describe our simulation setup; in section 3.4 we justify our choice of resolution; in section 3.5 we test our code against previous work; in section 3.6 we describe our suite of simulations; in section 3.7 we present our results for optimising the corotation torque; in section 3.8 we discuss in detail our three methods for measuring the corotation torque; in section 3.9 we discuss time-averaged disc density features associated with the torque; in section 3.10 we present our empirical fit; in section 3.11 we discuss our results; in section 3.12 we study the effect of the choice of softening parameter; and finally in section 3.13 we present our conclusions.

3.1 The Aims

The aim of this project was to empirically ascertain the corotation torque experienced by an embedded low-mass planet on an eccentric orbit, for a range of disc scale heights, to establish a fitting formula analogous to those produced be Paardekooper et al. (2010), if possible, suitable for use in N-body simulations of planet formation and to attempt to link this behaviour to changes in the streamline morphology and density structure of the disc.

3.2 Background

The current dataset describing the observed population of extrasolar planets displays a broad diversity in physical and orbital properties. Taken as a whole, these planetary systems are likely to contain substantial mass in heavy elements, such that their existence is difficult to explain using *in situ* formation scenarios because most disc models contain insufficient inventories of solid material at small radii (e.g. Hayashi, 1981; Weidenschilling, 1977). Large scale migration, possibly coupled with continuing mass growth, would appear to provide the most compelling explanation for many of these systems, although N-body models coupled with disc-driven migration have so far not managed to reproduce short-period multi-planet systems that are particularly similar to those observed (e.g. McNeil and Nelson, 2010). (See section 1.1).

While planet-planet gravitational scattering coupled with tidal interaction with the central star may explain some short-period planets, the compact, low mutual-inclination, short-period systems such as *Kepler-11* appear to be best explained through gas disc-driven migration. Low mass planets whose Hill radii are smaller than the local scale height (such that they do not carve out deep, tidally-truncated gaps) experience type I migration, driven by a combination of Lindblad and corotation torques (Goldreich and Tremaine, 1980; Ward, 1997; Tanaka et al., 2002). Particular interest has focussed on the role of corotation torques since it was first realised that they may counterbalance the rapid inward migration driven by Lindblad torques. In particular, strong positive gradients in disc surface density can cause the corotation torque to stall migration due to the associated gradient in vortensity (Masset et al., 2006b), and a negative entropy gradient may also cause migration to stall

(Paardekooper and Mellema, 2006; Baruteau and Masset, 2008; Paardekooper and Papaloizou, 2008).

Strong corotation torques (also known as "horseshoe drag"; Ward, 1991) arise through interaction between the planet and gas that executes horseshoe orbits in a disc with a radial gradient in vortensity and/or entropy. Given that horseshoe streamlines are a non-linear phenomenon, horseshoe drag is also referred to as the non-linear corotation torque (Paardekooper and Papaloizou, 2008). The vortensity-related corotation torque is prone to saturation in the absence of viscosity, which maintains the vortensity gradient across the horseshoe region against the tendency of orbital phase mixing there to flatten it out. Similarly, thermal diffusion or cooling is required to maintain the entropy-related corotation torque against saturation. Torque formulae have been derived that allow the steady-state corotation torque to be calculated for a broad range of disc and planet parameters (Paardekooper et al., 2010, 2011; Masset and Casoli, 2010). (See section 1.5).

In addition to saturation in the absence of viscous or thermal diffusion, the corotation torque has been shown to diminish for a planet on an eccentric orbit (Bitsch and Kley, 2010). At present the physical reason for this decrease is not clear, and as yet there has not been an extensive analysis of how the dependence of the corotation torque on eccentricity scales with variations in disc and planet parameters. Given that planet-planet interactions during planet formation and migration lead inevitably to eccentricity excitation (e.g. Cresswell and Nelson, 2006), further exploration of these issues is important in order to fully understand the role of migration in planetary formation. Using simple N-body simulations of planetary accretion coupled with prescriptions for type I migration torques obtained from Paardekooper et al. (2011), Hellary and Nelson (2012) examined the possible influence of eccentricity excitation on the oligarchic growth of planets, and concluded that the ability of horseshoe drag to prevent rapid inward migration of growing planets is diminished strongly when the associated quenching of the corotation torque is accounted for. Further examination of this is clearly required to test the assumptions of how the torque scales with eccentricity adopted in this latter study.

In this chapter, we present results from 2D hydrodynamic simulations of eccentric planets of different mass embedded in protoplanetary discs with differing effective vertical scale heights. Particular challenges faced when analysing the results include the tendency for moderate gaps and vortices to form in low

viscosity discs with relatively small vertical scale heights (i.e. $H/r \lesssim 0.05$). To overcome these problems three different methods for estimating the unsaturated corotation torque were employed as part of this project. As expected from the earlier simulations of Bitsch and Kley (2010), we observe that the corotation torque decreases as the planet eccentricity increases. We provide an empirically derived analytic fit formula for our simulation results which shows that the corotation torque decreases exponentially with orbital eccentricity, with the e-folding eccentricity scaling linearly with the local disc scale height.

3.3 The Model

We use the NIRVANA code described in the previous chapter to simulate a two-dimensional disc in polar coordinates. We use a resolution of either 1020 or 1024 cells in radius and 2048 in azimuth on either 48 or 64 cores after conducting the resolution study described in section 3.4. The simulations are computed in a frame of reference corotating with the planet's guiding centre, such that the eccentricity manifests itself as epicyclic motion around this guiding centre.

We use a gravitational potential softening parameter $b = 0.4h$ for the majority of our simulations, though we change this to explore the effect of the softening parameter in section 3.11.2. We use an initial disc density profile of the form $\sigma = \sigma_0 r^{-0.5}$ and an initial temperature profile of the form $T = T_0 r^{-2}$ in order to get a strong enough corotation torque to measure without difficulty according to equation 1.19. We normalise our disc mass to 1.35×10^{-3} in units of the central stellar mass, although in the absence of self-gravity, this simply linearly scales the resultant torque. We set the adiabatic exponent, $\gamma = 1.4$.

The inner and outer radial boundaries of our grid have been set to $r = 0.5$ and $r = 1.8$ respectively so as to be sufficiently far from the planet as to avoid boundary effects at that planet's location, and we employ reflecting boundary conditions with damping zones inside $r = 0.6$ and outside $r = 1.6$ to minimise wave reflection, using the scheme described by de Val-Borro et al. (2006). In azimuth, we simulate the full 2π of the disc and employ periodic boundary conditions.

We try different values of damping timescale at the radial boundaries, as il-

lustrated in figure 3.1. We find that $\tau_{\rm damp} = 0.05$ works well for H/r of 0.03, 0.05 and 0.07, where 0.03 works better for $H/r = 0.1$. This is consistent with the greater sound speed in a thicker disc and the consequent requirement that the damping be more rapid.

Our planet is set to have a mass of 1.5×10^{-5} in units of the central stellar mass, equivalent to a $5M_\oplus$ planet around a solar-mass star, with a fixed location of $(r, \phi) = (1, \frac{\pi}{2})$ in the rotating frame.

We use a simple Newtonian cooling scheme, as described in section 2.6.4 as being much less computationally expensive than using full radiation transport while still being more realistic than using either an adiabatic or a locally isothermal disc model. In section 3.7, we discuss our choice of cooling timescale.

We do not want to include torque from material gravitationally bound to the planet, so we exclude material inside the Hill radius. However, if a planet crosses an arbitrary threshold (with no physical significance), suddenly new cells are counted and an artifical 'jump' in torque is observed. To counteract this, we reject the model of including or excluding cells and instead modify the torque contribution as described in section 2.7.4. where H is the Hill radius.

3.4 Resolution Study

By using equation 1.23, we can calculate the expected half-width of the corotation region (horseshoe width), x_s, for a $5M_\oplus$ planet at $r = 1$ in disc for which $H/r = 0.05$. By imposing the condition that the horseshoe region should be resolved by at least 10 cells, we find that the entire computational domain in radius from $r = 0.5$ to 1.8 should be resolved by at least 200 cells[1]. This is consistent with our simulation results shown in figure 3.2, where there is a marked difference in total torque between the simulations with the radial resolution less than and greater than 200. In that figure we are seeing the initial 'peak' of torque, corresponding to the Lindblad and corotation torques combined. This 'initial peak' is discussed more in section 3.8.3 on our method (iii).

[1] $x_s = 1.68\sqrt{\frac{1.5\times10^{-5}}{0.05}}$, $\Delta x = \frac{x_s}{5}$, $\frac{1.3}{\Delta x} \sim 200$.

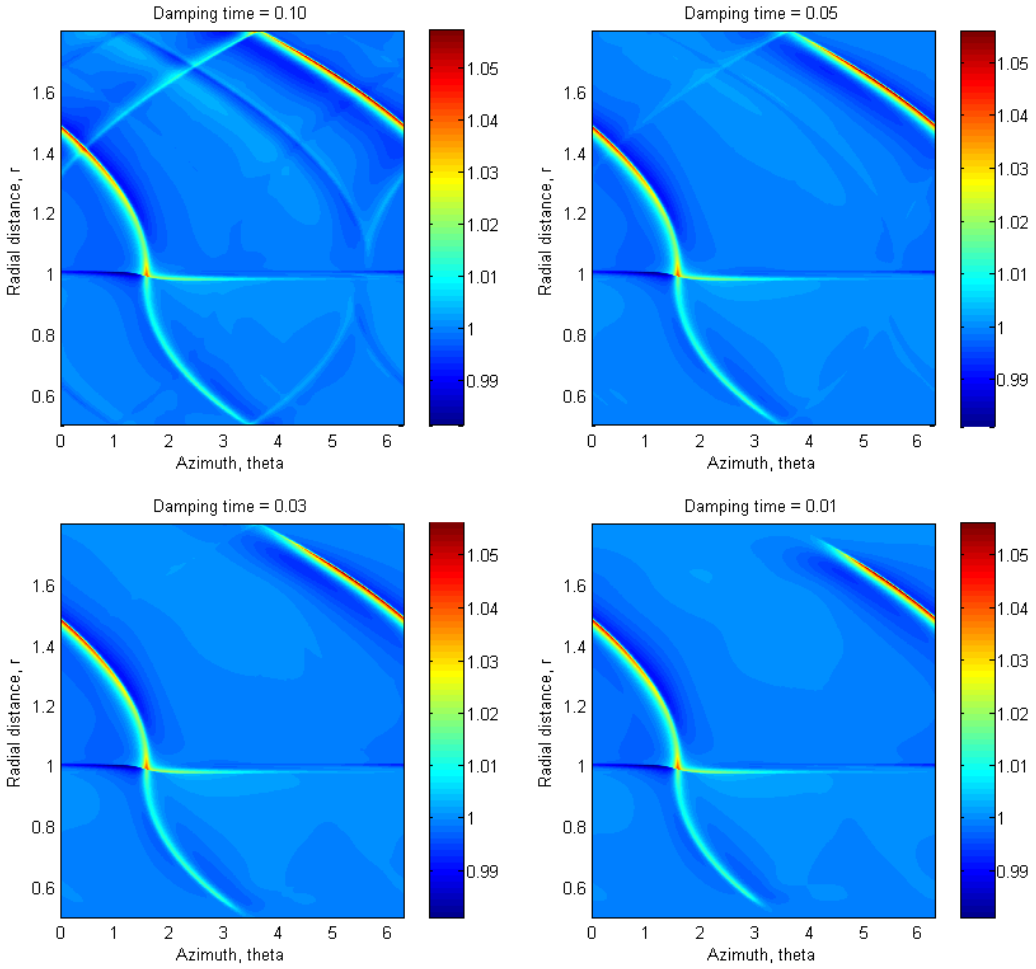

Figure 3.1: As an illustration of our choice of damping timecale, we see disc density perturbation profiles here for a $H/r = 0.1$ disc. The quantity being plotted is the perturbation to the initial density, ρ/ρ_0. Note that with the greater damping timescale, clear reflections are seen from the boundaries. These have the effect of changing the measured torque on the planet. In this case, the timescale of 0.03 was chosen.

We can see that the increase from 1024×2048 ($N_r \times N_\phi$) cells to 2048×4096 cells makes a negligible difference to the torque measured and that the resolution can potentially drop as low as 512×1024 while still giving comparable results.

Since we expect the morphology of the corotation region to change with increasing eccentricity, we select a resolution of 1024×2048 for our simulations to ensure that even a halving of horseshoe width will not cause any significant effects due to the lower resolution over the corotation region. Given the parallelised nature of our simulations and the need to efficiently use computation time by sensibly dividing the computational domain, we vary the radial resolution to 1020 in some cases.

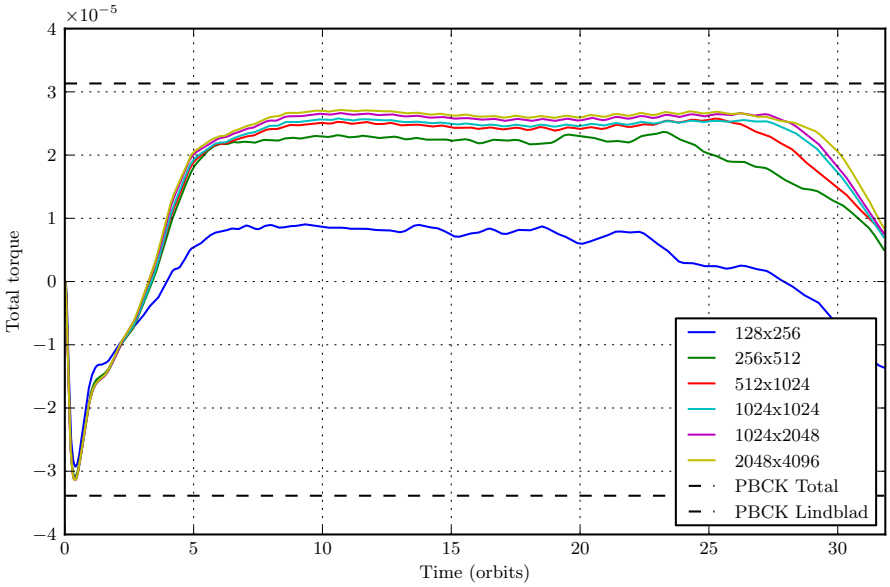

Figure 3.2: Resolution study, $r \times \phi$. For comparison, theoretical values for the total (Lindblad and corotation) torque and just the Lindblad torque calculated using the prescription of Paardekooper et al. (2010) are shown as dotted lines. The decrease in torque after $\sim$ 30 orbits is due to the onset of corotation torque saturation.

3.5 Testing code against previous work

We first test our code to ensure that we obtain torques comparable to those obtained by Paardekooper et al. (2010) in previous work, using those shown in figure 2 of their paper as our benchmark, both to preclude any major problems

in our code and also to confirm the applicability of their torque formulae, which we expect to hold. We set the kinematic viscosity[2] to be $\nu = 1 \times 10^{-7}$; low enough that we expect the corotation torque to saturate after many orbits. In these simulations, unlike in the rest of those performed for this project, the planet has a mass ratio of $q = 1.26 \times 10^{-5}$ (equivalent to 4.2 Earth masses around a solar-mass star) and the adiabatic constant $\gamma = 5/3$.

Our results are broadly consistent, with differences of only a few tens of percent, which we suggest might be explained by our use of a very low kinematic viscosity, allowing the corotation torque to saturate to a greater degree. Torque time-series from these simulations are shown in figures 3.3, 3.4 and 3.5.

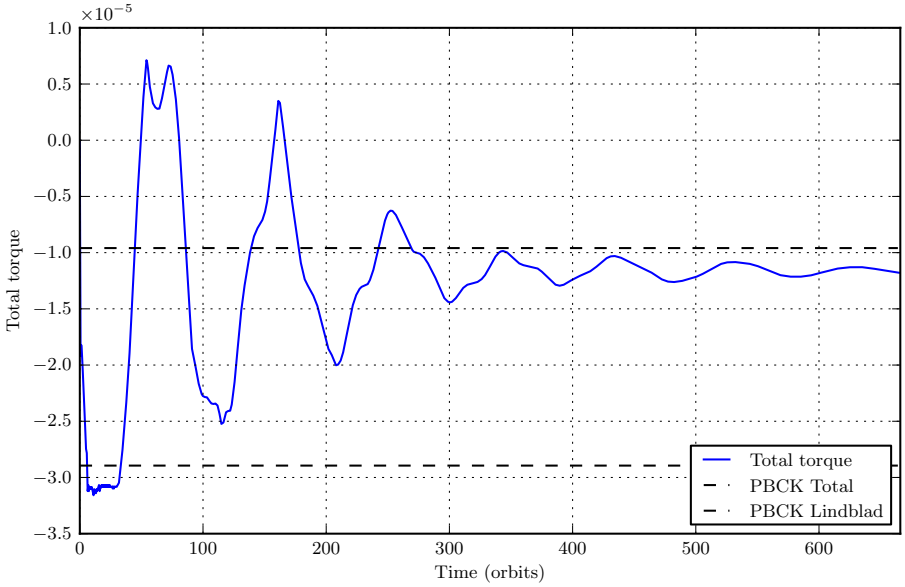

Figure 3.3: The test of our code against previous work by Paardekooper et al. (2010). For these simulations, we set the kinematic viscosity $\nu = 1 \times 10^{-7}$ and the gradients of density and temperature are $\alpha = 1.5$, $\beta = 0$. The planet has a mass of $q = 1.26 \times 10^{-5}$ and the adiabatic constant $\gamma = 5/3$.

[2]In code units, as described in section 2.7.2.

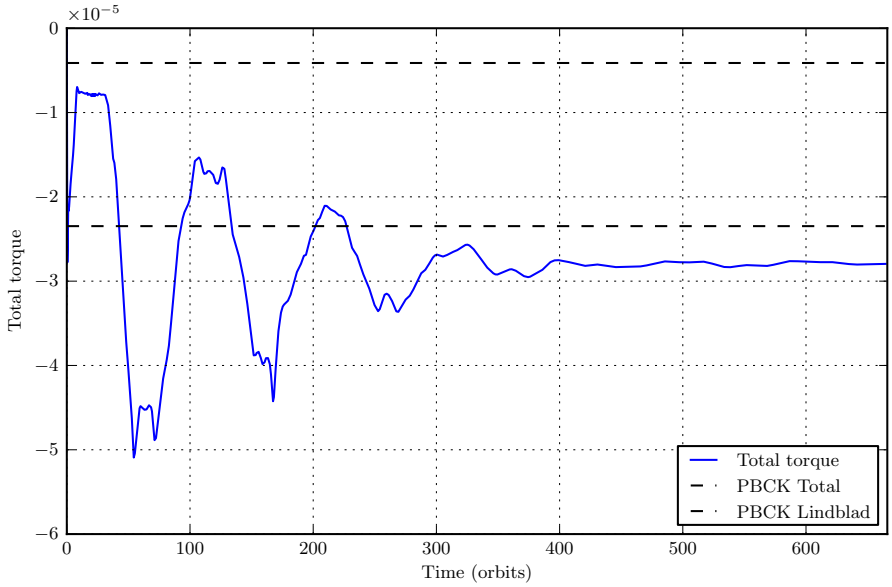

Figure 3.4: The test of our code against previous work by Paardekooper et al. (2010). For these simulations, we set the kinematic viscosity $\nu = 1 \times 10^{-7}$ and the gradients of density and temperature are $\alpha = 1.5$, $\beta = 2$. The planet has a mass of $q = 1.26 \times 10^{-5}$ and the adiabatic constant $\gamma = 5/3$.

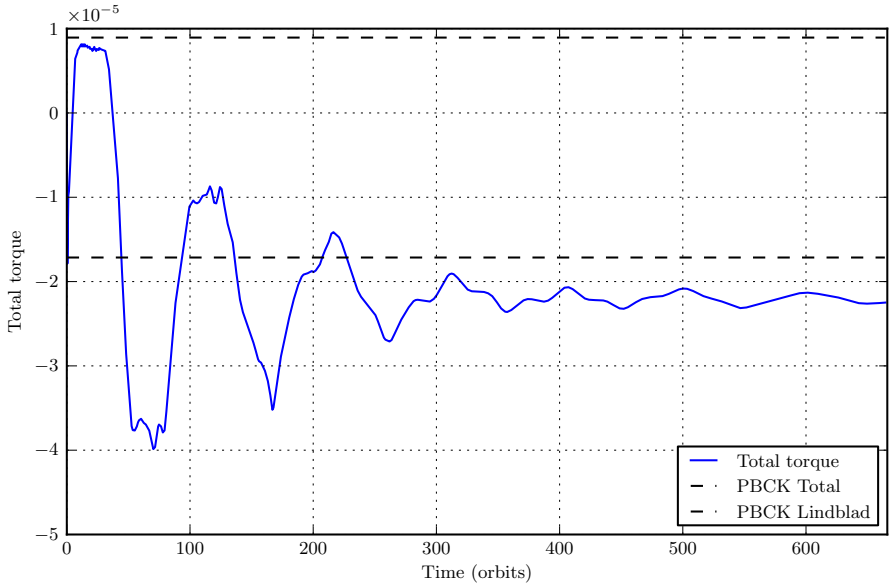

Figure 3.5: The test of our code against previous work by Paardekooper et al. (2010). For these simulations, we set the kinematic viscosity $\nu = 1 \times 10^{-7}$ and the gradients of density and temperature are $\alpha = 0$, $\beta = 1$. The planet has a mass of $q = 1.26 \times 10^{-5}$ and the adiabatic constant $\gamma = 5/3$.

3.6 The Simulations

We computed disc models with aspect ratios $h \equiv H/r = 0.03,\ 0.05,\ 0.07$ and 0.1. For each value of h, eccentricity values in the interval $0 \leq e \leq 0.3$ were considered. For each combination of h and e, we performed two separate simulations:

Set A An adiabatic disc with viscosity at the lowest value consistent with obtaining a well-behaved time series for the measured torque on the planet. We give these values in table 3.1. In the absence of this small viscosity we find that torque time series may become difficult to interpret due to strong time-dependencies introduced through the development of small vortices that form near the separatrices between circulating and librating material. A low viscosity adiabatic disc allows saturation of both the vortensity and entropy related contributions to the corotation torque as material in the horseshoe region becomes phase mixed and the vortensity and entropy gradients disappear. A torque time series from one of these simulations when the planet is on a circular orbit is shown in figure 3.6.

Set B A disc with viscosity and thermal diffusion set to values selected by successive trials to optimally unsaturate the corotation torque as described in section 3.7. We give the optimal values in table 3.1. The torque time series from such a simulation with a circular orbit is shown in figure 3.6, where all torques plotted are normalised by the quantity Γ_0/γ in which

$$\Gamma_0 = \left(\frac{q}{h}\right)^2 \sigma_{\rm p} r_{\rm p}^4 \Omega_{\rm p}^2, \tag{3.1}$$

as given in equation 1.18.

For all simulations, as the non-linear horseshoe drag is due to material undergoing horseshoe orbits, and the timescale for even the shortest horseshoe orbit is significantly longer than the planetary orbital period, we continually construct and record time-averaged density and velocity fields from the disc for further analysis. We also maintain a record of the contribution to the torque exerted on the planet by the disc as a function of radius in the disc.

For simulations in set A, it is assumed that after the total torque has reached

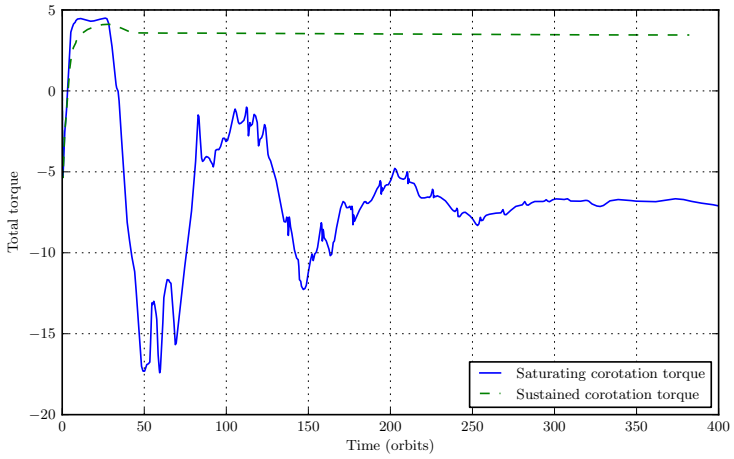

Figure 3.6: Here we see an example pair of simulations from sets A and B. In this method, we simply compare the steady-state values of the two torques, obtaining our estimate of the error from the residual variation in the signal beyond 250 orbits. This also serves as an illustration of our first method.

a steady-state, the corotation torque has saturated and only the Lindblad torque remains. For those in set B, we expect the steady-state total torque to approach the value predicted by the formulae of Paardekooper et al. (2010) for unsaturated corotation torques in the circular orbit case as seen in figure 3.6.

Using these two sets of simulations, we estimate the corotation torque for each different eccentricity using three methods described briefly here and then discussed in detail in the relevant later sections:

Method (i) By taking the difference between the long-term, steady-state, time-averaged torques obtained in the corresponding simulations from sets A and B. This method assumes that the Lindblad torque is the same in each simulation, such that the torque difference measures the unsaturated corotation torque obtained in the set B simulation directly.

Method (ii) By using time-averaged velocity fields to determine the extent of the region in which disc material is undergoing horseshoe orbits. We aggregate the torque contribution from this region by using time-averages of the torque versus radius data that we accumulate during the simulations.

Method (iii) By measuring the initial peak in the torque time series from simulations in set A associated with the initial growth of the corotation torque prior to its long-term saturation. This value is only reached after the horseshoe

trajectories have been set up but before any disc material has been returned to its original location– before phase mixing has taken place. This is the method most similar to previous measurements of the corotation torque (Paardekooper et al., 2010). The peak is then compared with the long-term steady torque which is assumed to comprise the Lindblad torque only due to saturation of the corotation torque.

3.6.1 Torque filtering

The torque time series for an eccentric planet consists of an average value, due to the motion of the planet's guiding centre, and a contribution due to the epicyclic motion that varies quasi-periodically on the planet orbital period. At high eccentricities, the contribution from the epicyclic motion dominates and obscures the averaged value that we require; that is, the value that would govern the planet's migration on long timescales, were it free to migrate. As this motion occurs on a much more rapid timescale than that of material within the corotation region, we use a Fourier transform filter to remove oscillations occurring on timescales more rapid than a few orbital periods. The choice of filter threshold was selected by trial, as shown in figure 3.7. The result of employing this procedure is shown in figure 3.8.

We can see that the resultant time series captures the averaged behaviour well, without the issues associated with running averaged, specifically the lack of data points to average over towards the start and end of the time series, which is a particular problem when the epicyclic oscillations are as large as they are in this case and we are interested in finding a peak at early times.

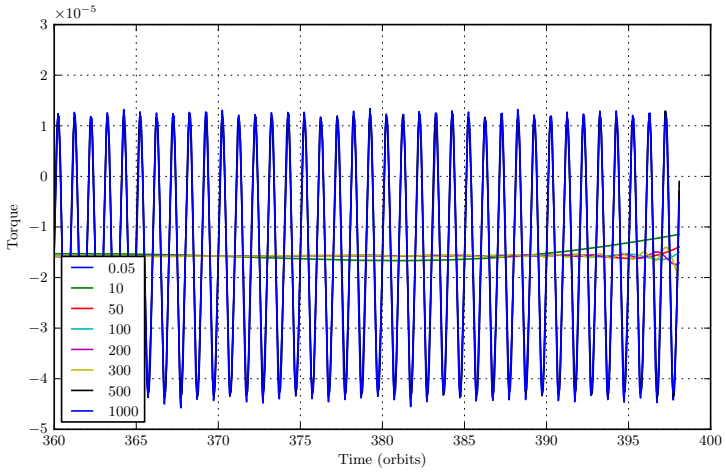

Figure 3.7: A comparison of the different filter thresholds tested to remove the highest frequency oscillations associated with the planet's epicyclic motion about its guiding centre, compared to the original signal. We select a parameter of 100.

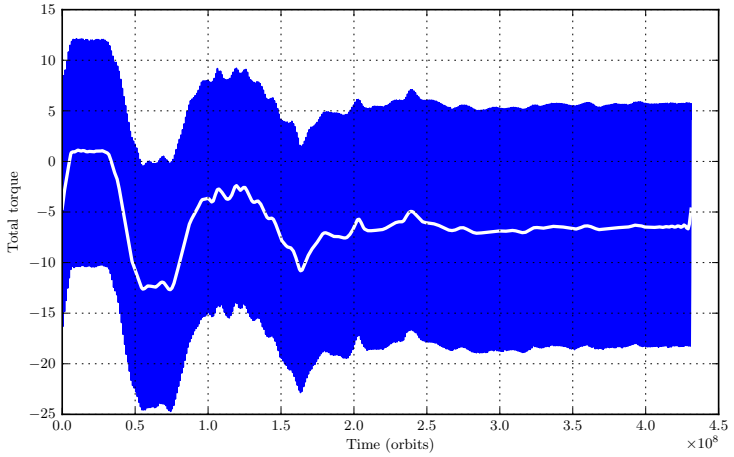

Figure 3.8: We use a simple Fourier transform filter to remove high frequency oscillations associated with the planet's epicyclic motion about its guiding centre and leave the long-term torque changes that we are interested in. Here we see the torque time series for $H/r = 0.07$ with $e = 0.02$ being filtered to remove the contribution of the epicyclic motion.

Table 3.1: Optimised entropy relaxation timescale, τ_{ent}, optimised kinematic viscosity, ν_{opt}, and minimum kinematic viscosity, ν_{min}, that allows for a quasi-steady flow for a planet on a circular orbit in a disc of various thicknesses. These values are obtained through numerical experimentation and are given in code units as described in section 2.7.2.

H/r	τ_{ent} (orbits)	ν_{opt}	ν_{min}
0.03	7	8×10^{-6}	2.5×10^{-7}
0.05	11	5×10^{-6}	1×10^{-7}
0.07	13	4×10^{-6}	1×10^{-7}
0.10	14	1.5×10^{-6}	1×10^{-8}

3.7 Optimising the corotation torque

Our first and second methods require that we have a simulation in which the corotation torque is nearly optimised, so as to give the greatest possible difference between the simulations in sets A and B and allow the corotation torque to be measured for high eccentricities.

We first run a series of simulations with no thermal relaxation, in which the entropy-related corotation torque is expected to saturate over many horseshoe libration periods. We then select different values of viscosity to find one which maximises the steady-state torque after many orbital periods. We consider this to be a value of viscosity which effectively unsaturates the vortensity-related corotation torque. This is illustrated in figure 3.9.

With this value of viscosity, we now select different values of thermal relaxation timescale and, again, look to maximise the steady-state torque, considering this unsaturate the entropy-related corotation torque as illustrated in figures 3.10 and 3.11.

When this technique is applied to a $H/r = 0.05$ disc as seen in figures 3.9, 3.10 and 3.11, we obtain $\tau_{\rm ent} = 11$ and $\nu = 5 \times 10^{-6}$. An analogous procedure is performed for all disc scale heights with results shown in table 3.1.

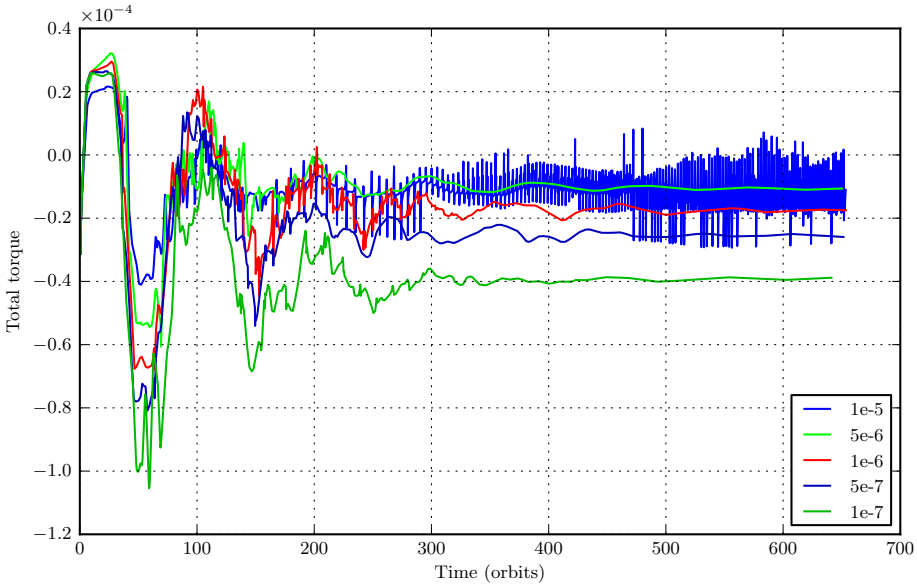

Figure 3.9: A torque time series for a $5M_\oplus$ planet on a circular orbit in a $H/r = 0.05$ disc, with no thermal relaxation and different values of kinematic viscosity, ν. We select $\nu = 5 \times 10^{-6}$ as being the greatest value consistent with a clean torque signal.

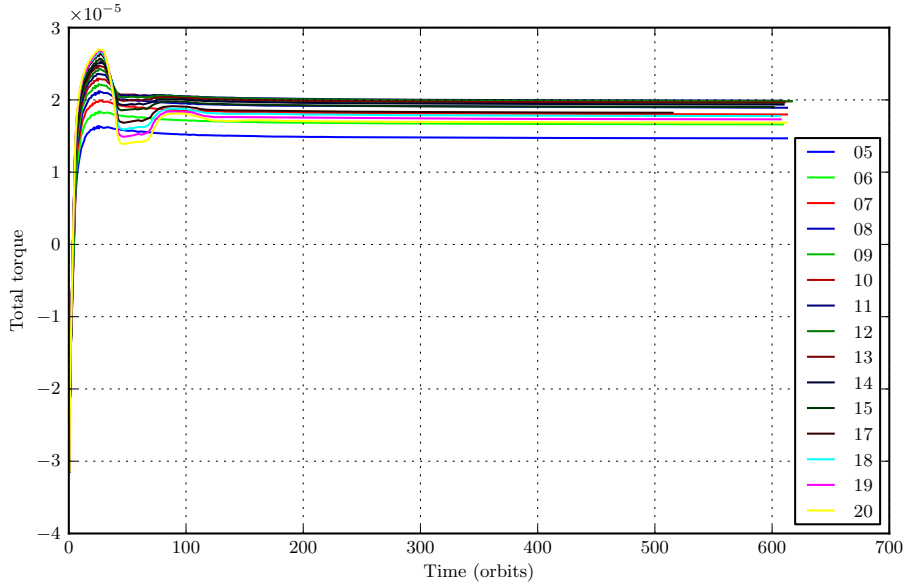

Figure 3.10: A torque time series for a $5M_\oplus$ planet on a circular orbit in a $H/r = 0.05$ disc, with kinematic viscosity, $\nu = 5 \times 10^{-6}$, and different values of thermal relaxation timescale (in orbits). Note the relatively small difference between the different plausible choices of timescale. We choose $\tau_{ent} = 11$, justified by figure 3.11.

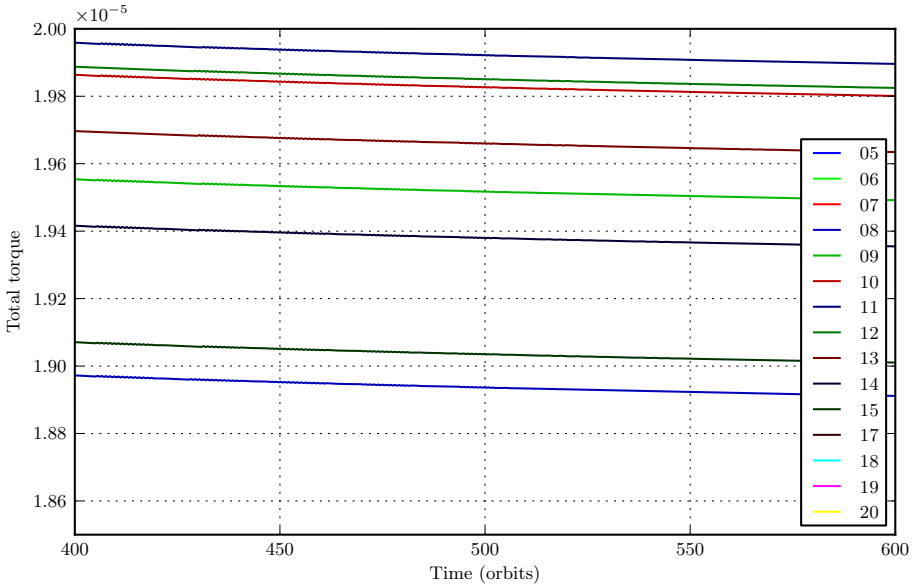

Figure 3.11: A torque time series for a $5M_\oplus$ planet on a circular orbit in a $H/r = 0.05$ disc, with kinematic viscosity, $\nu = 5 \times 10^{-6}$, and different values of thermal relaxation timescale (in orbits). Here we see a 'zoomed in' plot of figure 3.10, justifying our choice of $\tau_{ent} = 11$.

3.8 Measuring the Corotation Torque

In this section we present the results from the simulations on how the corotation torque varies with eccentricity and disc parameters, showing the results obtained with each of the methods used to estimate the corotation torque. We begin by presenting results for planet mass 5 $M_\oplus$ and disc models with $h = 0.03$, 0.05 and 0.07, followed by a model with 5 $M_\oplus$ and $h = 0.1$. Note that a final suite of simulations was conducted to test our results under a different conditions; these simulations of a mode with planet mass 10 $M_\oplus$ and $h = 0.1$ are presented in section 3.10.1. The steady state torque measured in all our simulations with planet mass 5 $M_\oplus$ is shown in figure 3.12, in which we see the expected Lindblad torque direction reversal as the eccentricity reaches Paploizou-Larwood regime of $e \gtrsim 1.1\frac{H}{r}$ (Papaloizou and Larwood, 2002). Some of the anomalous results are discussed in the next subsection, as these torques are used in method (i) to calculate the corotation torque. We can also immediately note from figure 3.12 that at large values of eccentricity, the two sets of torque values essentially coincide as the corotation contribution diminishes.

3.8.1 Method (i)

When using this method to estimate the steady corotation torque as a function of eccentricity, we first filter out high frequency oscillations in the torque time-series due to the epicyclic motion of the planet as described in section 3.6.1, and then take the difference between the results of simulations in sets A and B. In principle, the long-term steady torques in set A converge to pure Lindblad torques, and those in set B consist of the Lindblad plus sustained corotation torque, so we take the difference and use this as a measure of the corotation torque. The results obtained using this method are shown in figure 3.13, where we plot the estimated corotation torque value versus eccentricity. As there is residual time variation in the torque at the end of the simulations, we plot the mean torque (averaged between 240 and 350 orbits), and error bars showing three standard deviations about the mean.

The simulations from set B with thermal relaxation and viscosity produce smooth, well-behaved results that tend toward a well-defined steady state after sufficient run-time. There are a number of issues, however, affecting some low-viscosity disc models from set A that combine to make it difficult to obtain

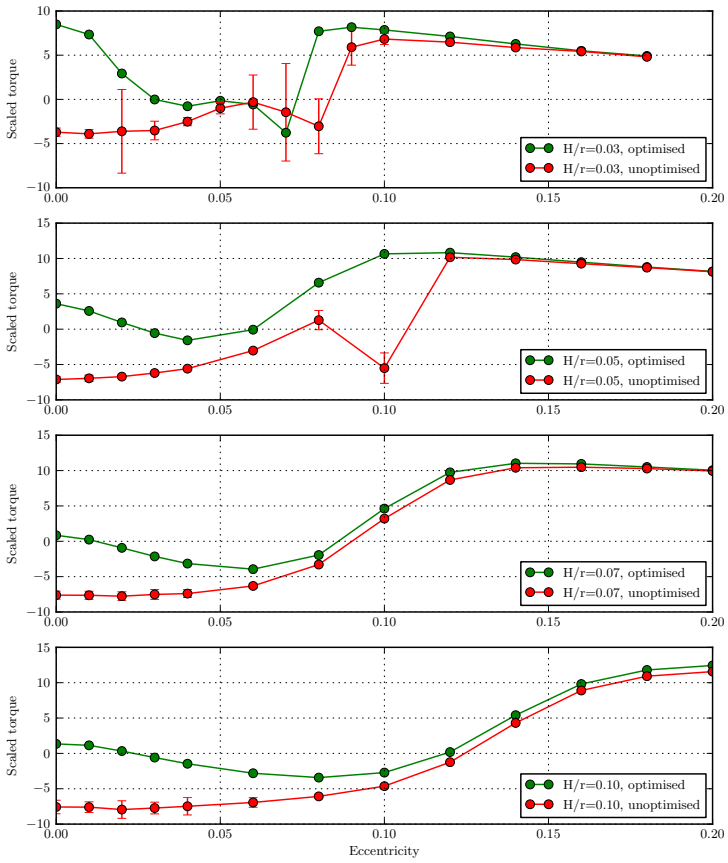

Figure 3.12: The total torque recorded in the steady state in all simulations with $H/r = 0.03$,0.05 and 0.07. Note the Lindblad torque reversal as we expect.

.

accurate estimates of corotation torques. They involve restructuring of the disc in some fashion. First, we find that the thinner, low viscosity disc models develop moderate gaps due to tidal torques from the planet. These have depth $\sim$ 10-20 % of the background surface density. Although these models do not satisfy the usual gap formation requirement that the planet Hill sphere size exceeds the vertical scale height (see e.g. Lin and Papaloizou, 1993; Crida et al., 2006), non-linear damping of the spiral waves deposits angular momentum in the disc near the planet and can cause a moderate annular dip to develop in the local surface density profile. This effect has been predicted analytically by Tanaka et al. (2002) and observed in simulations by Muto et al. (2010). The gap impacts on the estimate of the Lindblad torque in these cases, and

therefore affects the corotation torque estimate because a similar gap does not develop in the corresponding viscous disc model. This gap is shown in figure 3.14 where the azimuthally-averaged density profiles for $H/r = 0.03$ and 0.07 are compared at several eccentricities and the significant density perturbation in the thinner disc is clearly apparent.

The second issue is that for eccentricities $e \geq 0.06$ in the $h = 0.03$ runs, a large scale discrete vortex forms very close to the corotation radius of the planet guiding centre. This moves very slowly relative to the planet, but exerts a time-varying torque on it that is very difficult to average out because of the long run times that would be required. This clearly has an effect on our ability to measure the corotation torque using method (i). Finally, for some runs with $h = 0.03$ and 0.05, and for intermediate values of the eccentricity (i.e. $0.07 \lesssim e \lesssim 0.1$), we observe the development of discrete structures in the simulations. When the time averaged surface density is rendered as a colour map we observe these structures to sit in or at the inner edge of the horseshoe region close to the mean location of the planet. They do not appear to be vortices, but instead seem to be features related to the high density structure that forms behind the planet at pericentre. As can be seen in the middle panel of figure 3.13, for example, this is an issue that affects the torque in the range $e = 0.08$ to 0.1 cases this particular value of h. So far we have been unable to determine why only these specific runs give rise to this phenomenon.

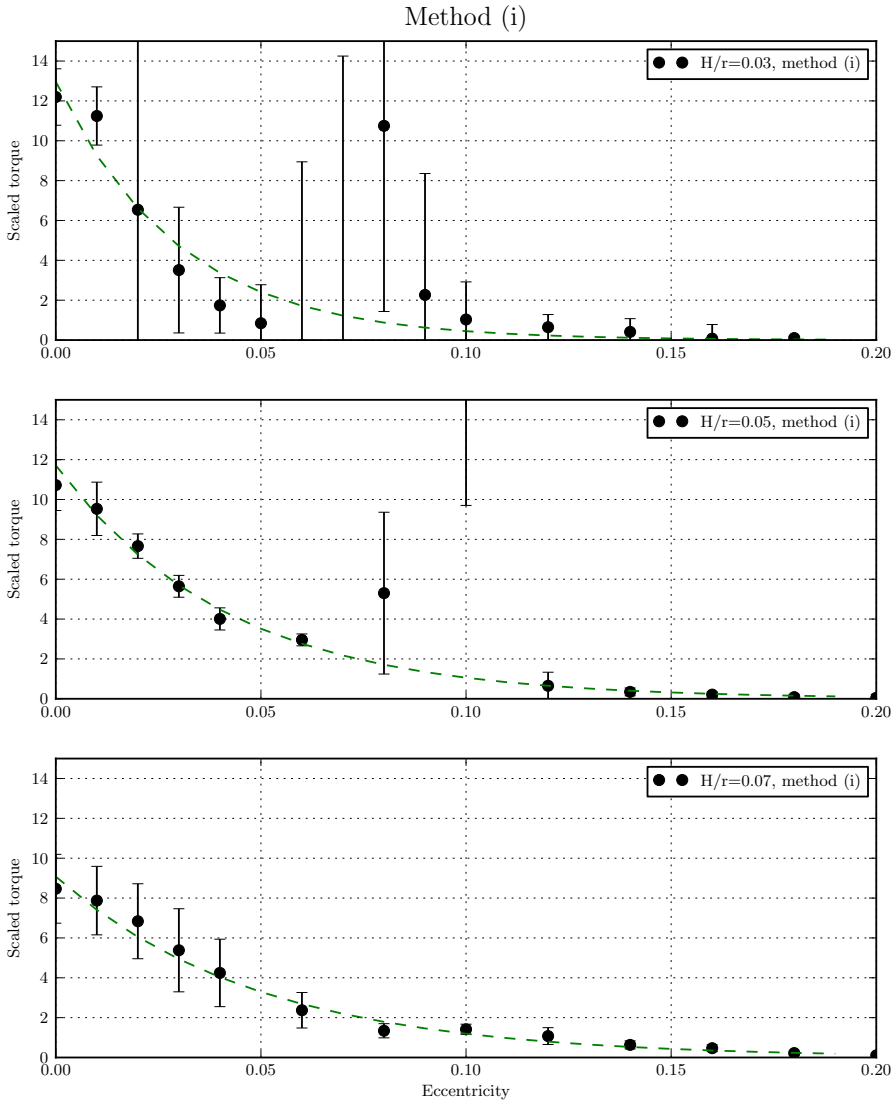

Figure 3.13: Here we plot the corotation torque value versus eccentricity as estimated by our method (i). As there is residual time variation in the torque at the end of the simulations, we plot the mean torque (averaged between 240 and 350 orbits), and error bars showing three standard deviations about the mean. The fits shown by the dotted lines are exponential decays, which we discuss in section 3.10.

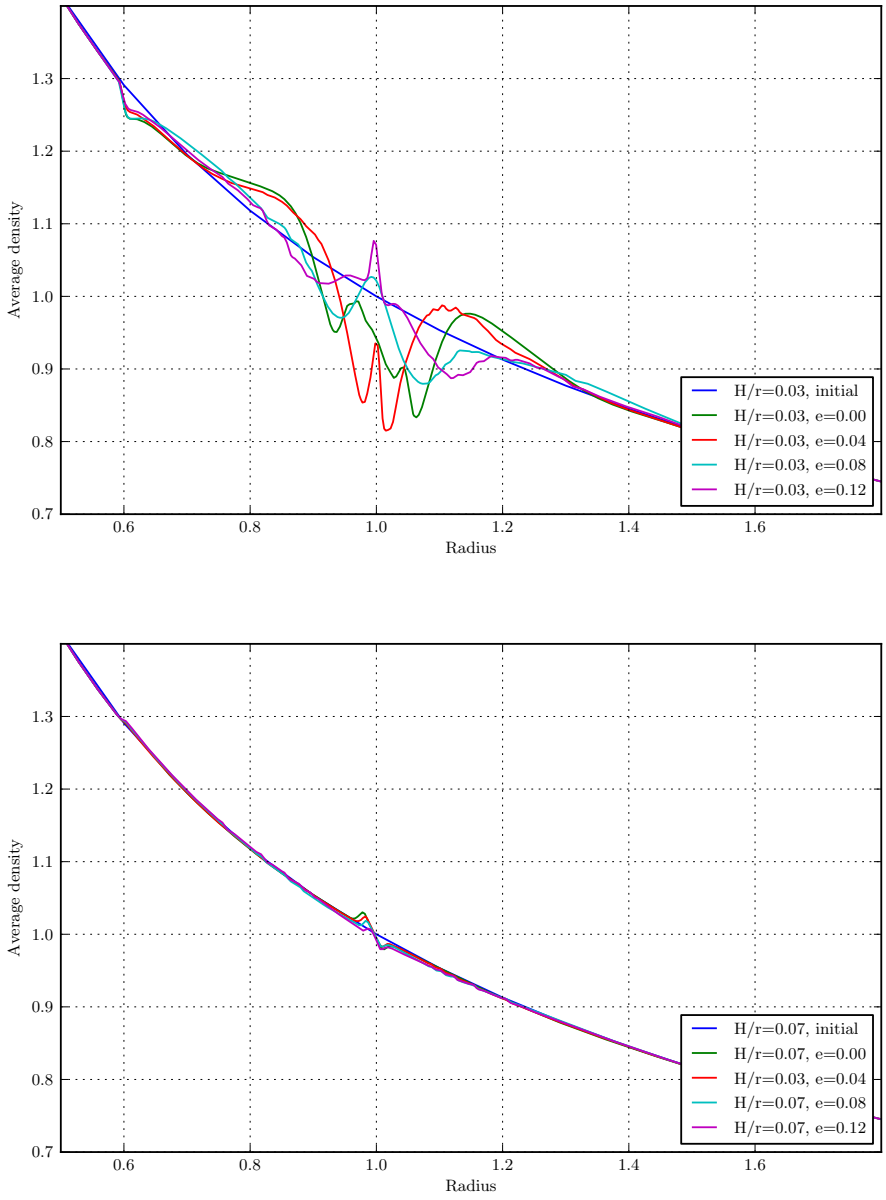

Figure 3.14: The perturbation to the azimuthally-averaged density profile in a $H/r = 0.03$ disc compared to a $H/r = 0.07$ disc. In the thinner disc, the density perturbation is much more signficant.

3.8.2 Method (ii)

This method estimates the corotation torque by defining a region of the disc to be the horseshoe region through inspection of fluid streamlines obtained from time averages of the disc velocity field taken over many orbits of the planet. A starting location is chosen in the disc from which we construct fluid streamlines by integrating the averaged velocity field. Linear interpolation is used to define the local velocity away from the centres of grid cells. By performing this integration for a large number of closely separated initial locations, we are able to precisely locate the region in which material undergoes horseshoe turns on average. In our parlance, the location between librating and circulating material is delineated by the 'last circulating streamline'. There is one interior and exterior to the planet's semi-major axis. In figure 3.15 we plot half the distance between the inner and outer last circulating streamlines as a function of azimuth for all models drawn from set B that we are considering in this section ($m_{\rm p} = 5$ M$_\oplus$ and $h = 0.03$, 0.05, 0.07). Each line corresponds to a simulation with different planet eccentricity, and we note the clear trend for the horseshoe region to narrow as e increases. The half-width of the corotation region is smallest for the most eccentric planets in the thickest disc, where $x_s \sim 0.01$, which we note is resolved by ~ 10 cells in our simulations. For the $h = 0.07$ disc, these streamlines are also shown in figures 3.22, 3.23, 3.24, 3.25 and 3.26. We discuss later how they narrow for increasing eccentricity, and that the density perturbations associated with the corotation torque are contained within the defined boundaries of the corotation region.

For the purpose of calculating the corotation torque using method (ii), the corotation region is taken to be an annulus whose width is defined to be the distance between the points on the inner and outer last circulating streamlines that are furthest from the planet's orbital radius. Once the corotation region has been defined, the gravitational force exerted by disc material on the planet from within that region is summed and time-averaged. Given that we are interested in measuring the steady corotation torque we apply this method to simulations in set B only. In general we expect the corotation torques to be localised within this horseshoe region, and the Lindblad torque to originate from beyond a distance to the planet equal to $2H/3$. In figure 3.16, we show the torque acting on the planet as a function of radius in the disc, demonstrating the localisation of the two torque contributions to these regions. Further features displayed in the figure are worthy of note. We see the magnitude of

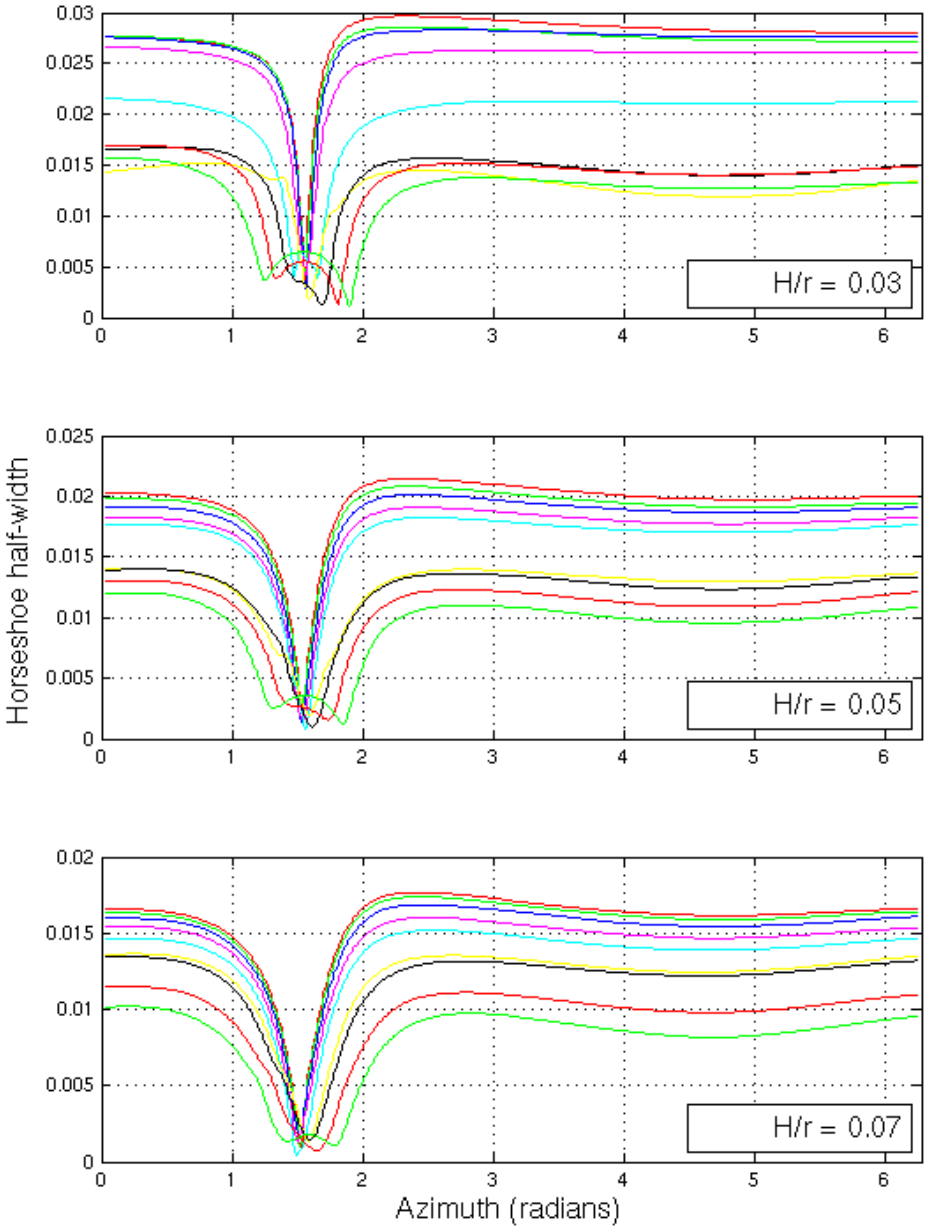

Figure 3.15: The horseshoe half-width, x_s, as a function of azimuth for all our set B simulations with $H/r = 0.03$, 0.05 and 0.07. Eccentricity increases in increments of 0.02 from 0.00.

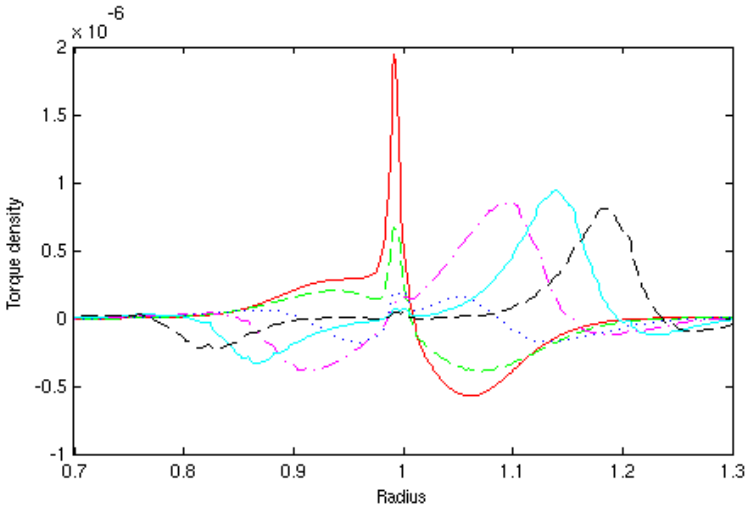

Figure 3.16: Torque as a function of radius for a disc with $h = 0.07$ and a sustained corotation torque. Eccentricities shown are 0 (red, solid), 0.04 (green, dashed), 0.08 (blue, dotted), 0.12 (magenta, dot-dash), 0.16 (cyan, solid), 0.20 (black, dashed). Note the Lindblad torque reversal for $e > 1.1h$ manifested as the reversal of the sign of the torque contributions from both the inner and outer disc. Also note the clear localisation of the corotation torque to the corotation region, centered around $r = 1$.

the corotation torque decrease with increasing eccentricity, and we also observe the Lindblad torque contributions from the inner and outer disc change sign as the eccentricity exceeds h. Furthermore, for the higher eccentricity cases we see the contributions from the inner and outer disc torques originate from the pericentre and apocentre of the planet orbit as we expect from the Papaloizou-Larwood model of the Lindblad torque at high eccentricities.

The estimates of the steady corotation torques for each of the models with planet mass equal to 5 $M_\oplus$ and $h = 0.03$, 0.05 and 0.07 are shown in figure 3.17. The filled circles represent values for the corotation torque obtained by taking a fiducial value for the width of the horseshoe region (the distance between the points on the inner and outer last circulating streamlines that are furthest from the planet's orbital radius). The error bars represent the fact that there is some ambiguity in the corotation torque because the last circulating streamlines used to define the boundary of the corotation region do not lie at constant distance from the corotation radius of the planet guiding centre. These error bars were obtained by moving the boundary of the corotation region 25% further away from the planet and 25% closer to it. This method is shown schematically in figure 3.18.

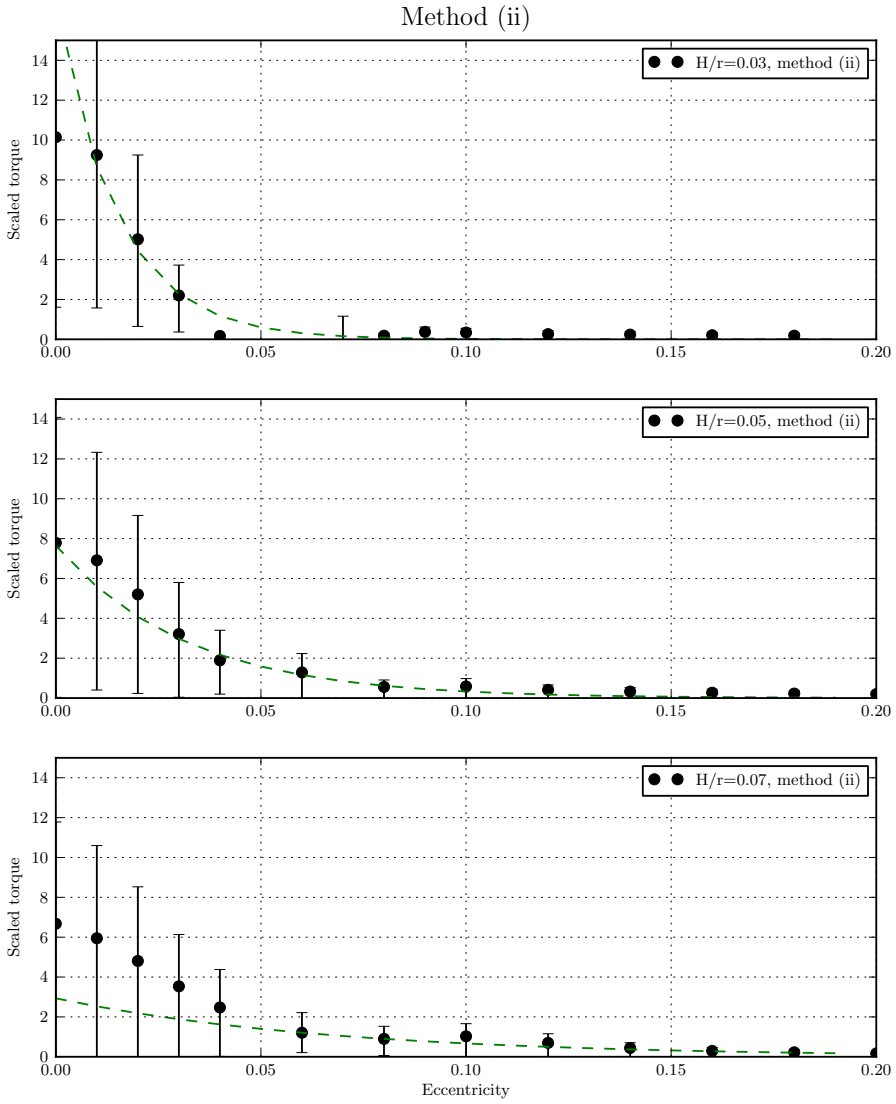

Figure 3.17: Here we plot the corotation torque value versus eccentricity as estimated by our method (ii). Error bars were obtained by moving the boundary of the corotation region 25% further away from the planet and 25% closer to it. The fits shown by the dotted lines are exponential decays, which we discuss in section 3.10.

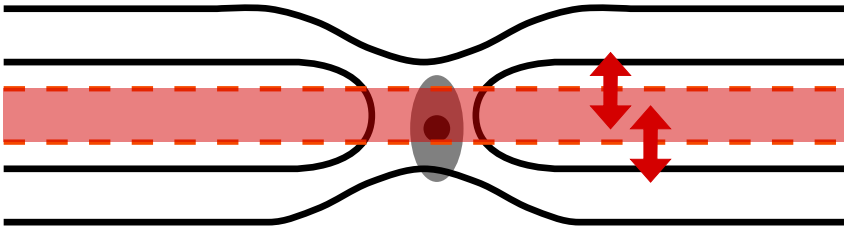

Figure 3.18: A schematic to illustrate the principle of our second method of determining the corotation torque. Note the offset between the location of the planet (the black circle) and the 'centre' of the velocity streamlines (solid black lines) as described by Paardekooper and Papaloizou (2009b). We select an area (shaded in red here and bordered by dotted lines) and calculate the torque due to material inside it. We call this the corotation torque. To explore the robustness of this method, we change the width of this area, as indicated by the arrows.

As with method (i) for estimating corotation torques, this method also suffers from a drawback, which is that high density material that forms close to the planet at apo- and pericentre can enter the defined horseshoe region. Even though these high density features are not related to the horseshoe drag, they nonetheless can contribute to the estimate of the torque using method (ii) because we have no way of excluding them from the torque calculation. In terms of the magnitude of the corotation torque estimate, this method gives a lower value than the other two because of this effect. We note, however, that this method gives a smoothly varying monotonic estimate of the corotation torque as a function of eccentricity, unlike methods (i) and (iii), demonstrating that the steady corotation torque in a viscous disc with cooling really does behave in the expected manner.

3.8.3 Method (iii)

This method is the most comparable to that used in previous work (e.g. Paardekooper et al., 2010). We begin by using a Fourier transform filter to remove high frequency oscillations from torque time series obtained from simulations in set A. We then measure the difference between the long-term steady state (Lindblad) torque in these low viscosity adiabatic discs, and the torque value immediately after approximately one horseshoe libration period has elapsed when the surface density perturbations in the horseshoe region have been set up through the advection of entropy and vortensity. This is the moment when the transient corotation torque reaches its maximum positive value, as shown for example by the line in figure 3.19. Corotation torque estimates obtained using this method are shown in figure 3.20. As with method (i), this method also has some drawbacks, because the long-term torque that is supposed to represent the Lindblad torque is influenced by the previously described gap and vortex formation.

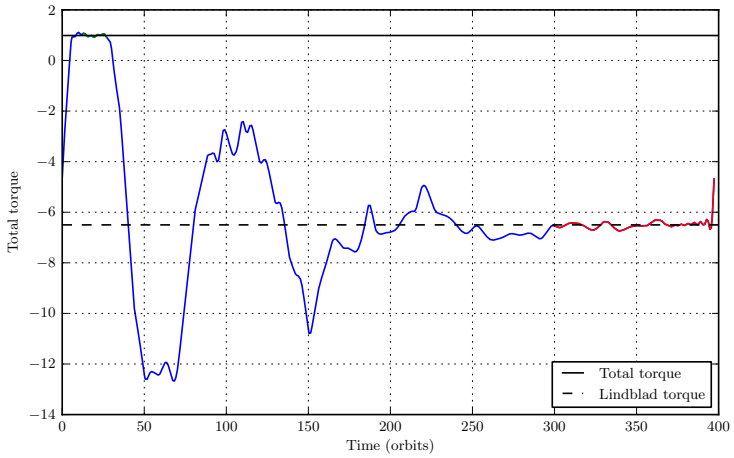

Figure 3.19: An illustration of our third method. Note that after approximately one horsshoe libration period, the total torque peaks, before relaxing on a timescale of hundreds of orbits to the Lindblad torque value as the corotation torque saturates. We measure the corotation torque from the difference between the torque torque and the steady-state value. Our measurements of the total and Lindblad torque are overplotted as the solid and dashed lines respectively.

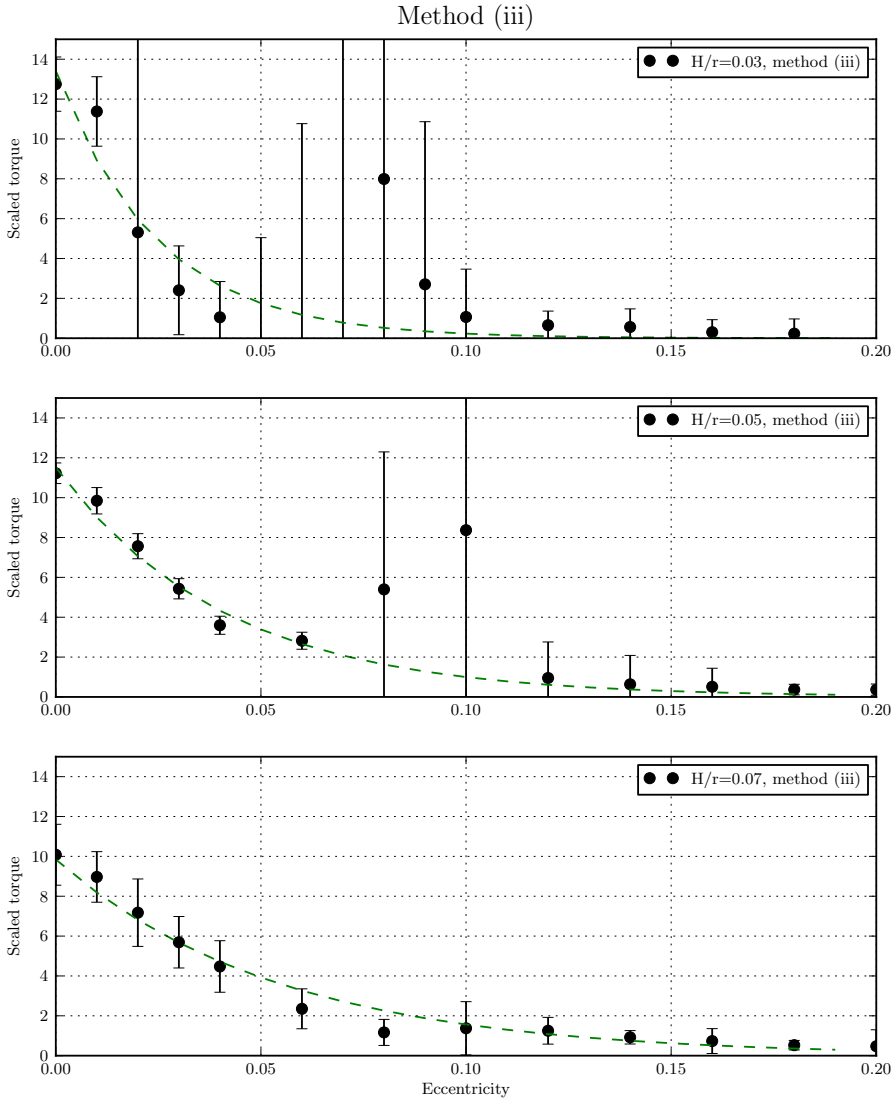

Figure 3.20: Here we plot the corotation torque value versus eccentricity as estimated by our method (iii). Error bars were obtained by combining the variation in the measurement of the total torque 'peak' with that in the steady-state Lindblad torque 'tail'. The fits shown by the dotted lines are exponential decays, which we discuss in section 3.10.

3.8.4 A thicker disc: $h = 0.1$

The simulations described above adopted discs with aspect ratios in the range expected for protoplanetary discs. Our results, however, show significant dependence on the disc thickness because of non-linear effects (e.g. gap opening), so we consider a thicker disc model with $h = 0.1$. We have repeated the corotation torque estimates obtained from methods (i), (ii) and (iii) for a broad range of eccentricities, and the corotation torque values are plotted in figure 3.21. The plots in this figure confirm the general trends noted for the thinner disc models: improvement in the behaviour of torque estimates as one employs thicker disc models; a tendency for method (ii) to produce a low estimate for the corotation torque; and clear decrease in corotation torque as the eccentricity increases.

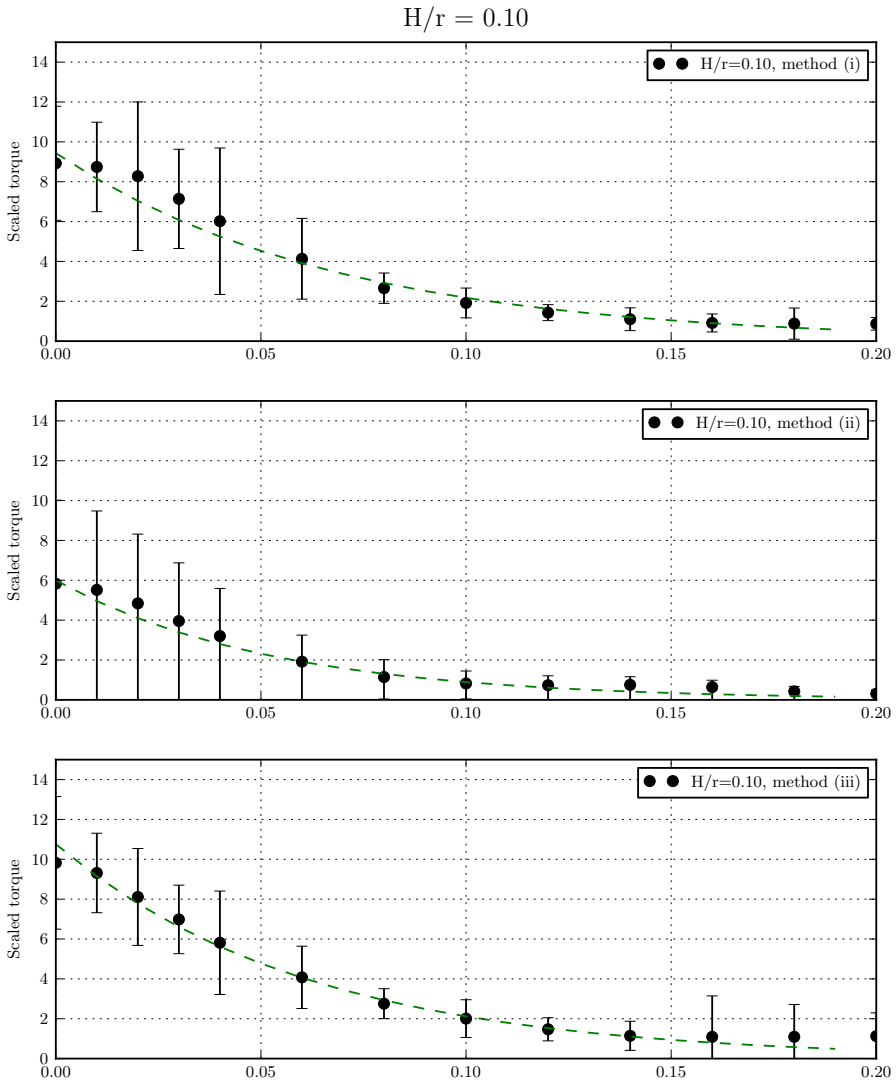

Figure 3.21: Here we plot the corotation torque against eccentricity for our simulations in $H/r = 0.10$ discs, as measured by all three methods.

3.9 Disc density fields

3.9.1 The corotation region morphology

In figures 3.22, 3.23, 3.24, 3.25 and 3.26 we show time-averaged steady-state surface density fields for the $h = 0.07$ discs with optimised, sustained corotation torques. Using the corresponding time-averaged velocity fields, we locate and superimpose the circulating streamline that sits closest to the horseshoe region (interior and exterior to the planet) where the gas is seen to librate rather than circulate (the 'last circulating streamline'). As such, this streamline acts as the boundary that separates the circulating and librating regions. Inspection of these figures shows clearly the tendency for the width of the horseshoe region to decrease as the eccentricity increases, with the horseshoe streamline u-turns broadly confined to the region outside the path of the planet's epicyclic motion. Furthermore, each panel shows the presence of a positive surface density perturbation within the horseshoe region that sits just ahead of the planet, and a negative perturbation that sits just behind it (in the inertial frame, the sense of motion in this figure would be from left to right). As has been discussed in previous work (e.g. Baruteau and Masset, 2008), these perturbations arise from the advection of fluid elements on horseshoe orbits that almost conserve their entropy (and vortensity) around the horseshoe u-turn (in the absence of viscosity, thermal relaxation or shocks these quantities should be conserved). Maintenance of local pressure equilibrium causes regions that receive low entropy material from the outer disc to contract. Regions behind the planet that receive high entropy material expand. The resulting surface density perturbations lead to the observed positive corotation torque, as shown earlier in figure 3.6, for example. This perturbation is present in all simulations presented in figures 3.22, 3.23, 3.24, 3.25 and 3.26, but diminishes as the eccentricity increases and the width of the horseshoe region decreases because the advected entropy introduces a reduced pressure perturbation.

3.9.2 Eccentric spiral density waves

Each of the panels in these figures shows the characteristic spiral density wave, but as the eccentricity increases the single wave that is present interior and exterior to the planet splits into two well-defined wake-like structures. This arises

because the epicyclic motion of the planet around its guiding centre causes the planet to travel more slowly than local disc material when at apocentre, and faster than local material when at pericentre. This leads to periodic excitation of inward and outward propagating wakes at these two phases of the orbit, as described for example by Kley and Nelson (2012). The relative motion between gas and planet at apo- and pericentre also leads to a reversal of the normally negative Lindblad torque when $e \geq h$. This is because orbiting gas is gravitationally focussed to a region that leads the planet at apocentre, creating a positive density perturbation in front of the planet that exerts a positive torque. This provides the dominant contribution to the orbit-averaged torque because the planet spends most of its time at apocentre. This reversal of the Lindblad torque for $e > h$ was first reported by Papaloizou and Larwood (2002), who presented torque calculations based on summing contributions from numerous eccentric Lindblad resonances.

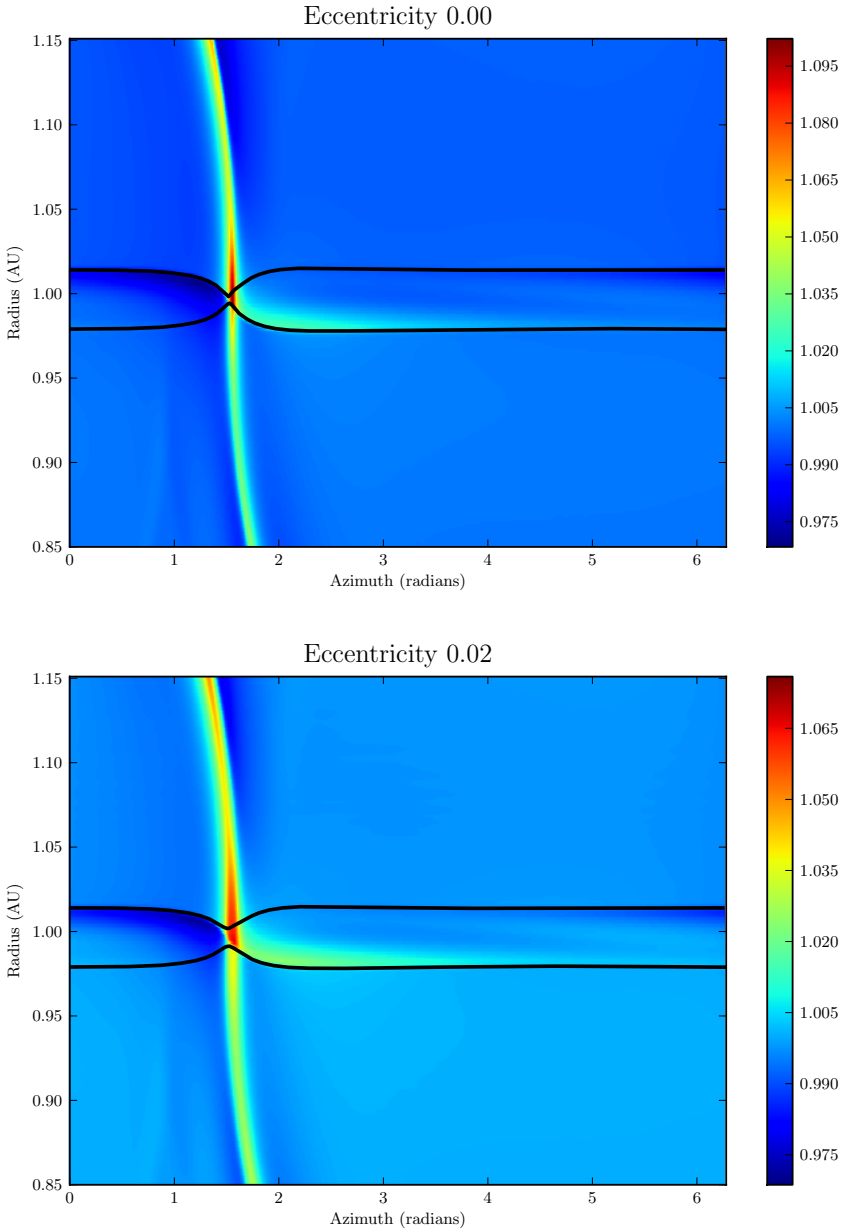

Figure 3.22: A $5M_\oplus$ planet in a $H/r = 0.07$ disc, with unsaturated corotation torque. Eccentricities of 0.00 and 0.02 are shown here. The quantity plotted is the perturbation to the equilibrium density ρ_0/ρ and the last circulating streamline on either side, as defined in the text, is overplotted.

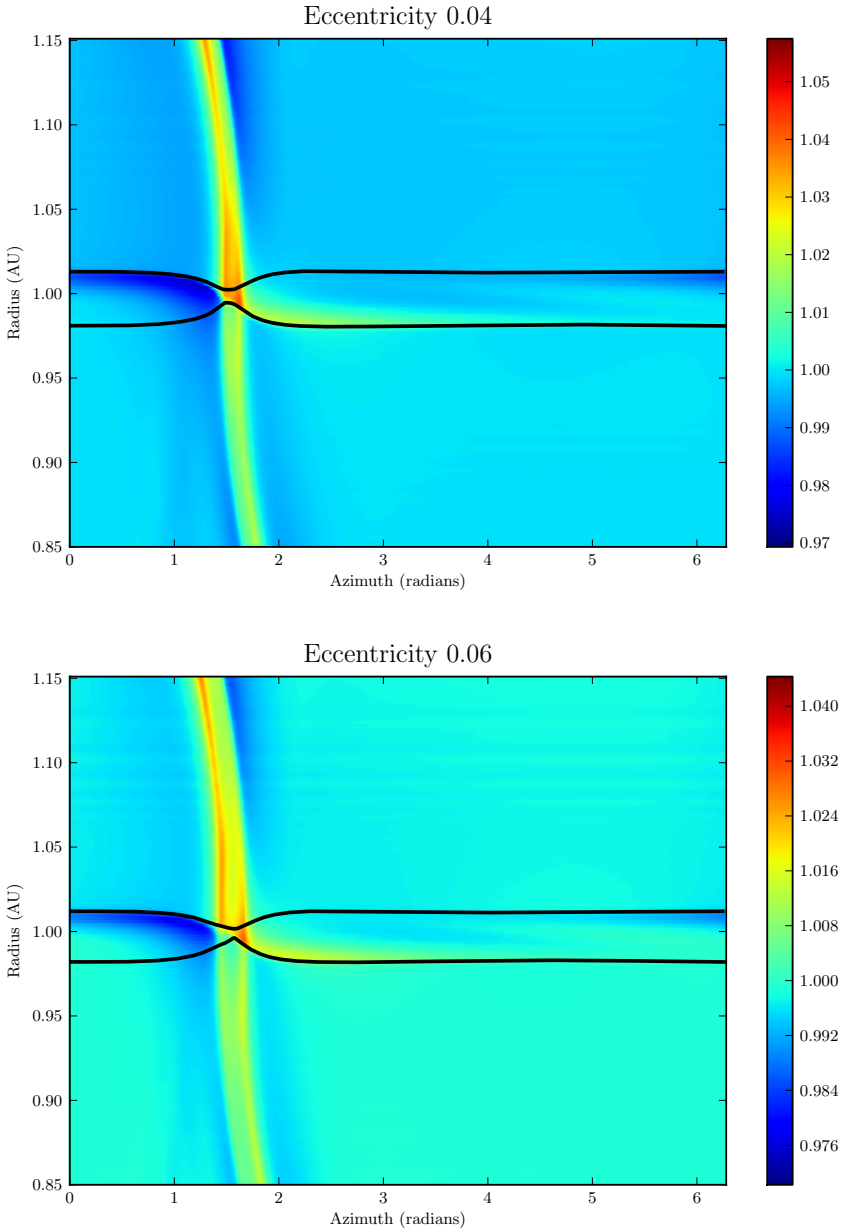

Figure 3.23: A $5M_\oplus$ planet in a $H/r = 0.07$ disc, with unsaturated corotation torque. Eccentricities of 0.04 and 0.06 are shown here. The quantity plotted is the perturbation to the equilibrium density ρ_0/ρ and the last circulating streamline on either side, as defined in the text, is overplotted.

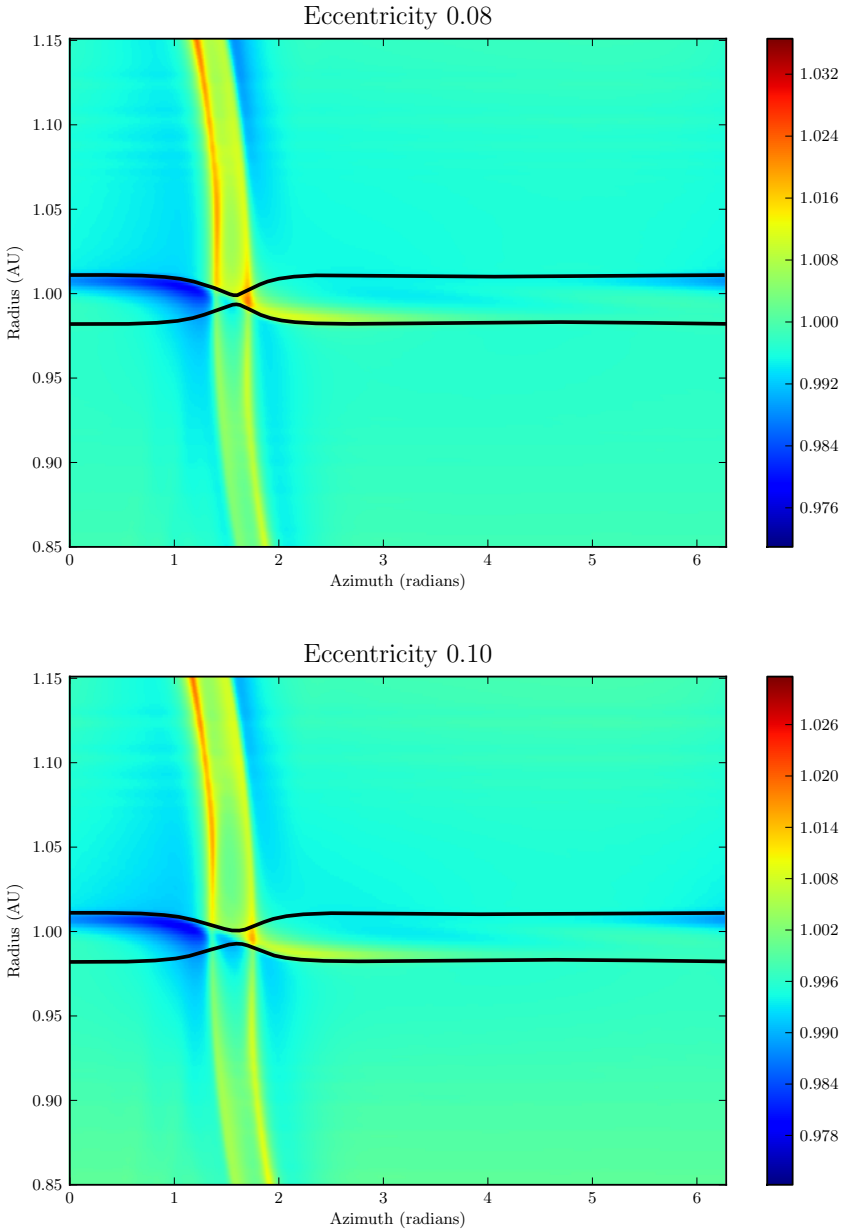

Figure 3.24: A $5M_\oplus$ planet in a $H/r = 0.07$ disc, with unsaturated corotation torque. Eccentricities of 0.08 and 0.10 are shown here. The quantity plotted is the perturbation to the equilibrium density ρ_0/ρ and the last circulating streamline on either side, as defined in the text, is overplotted.

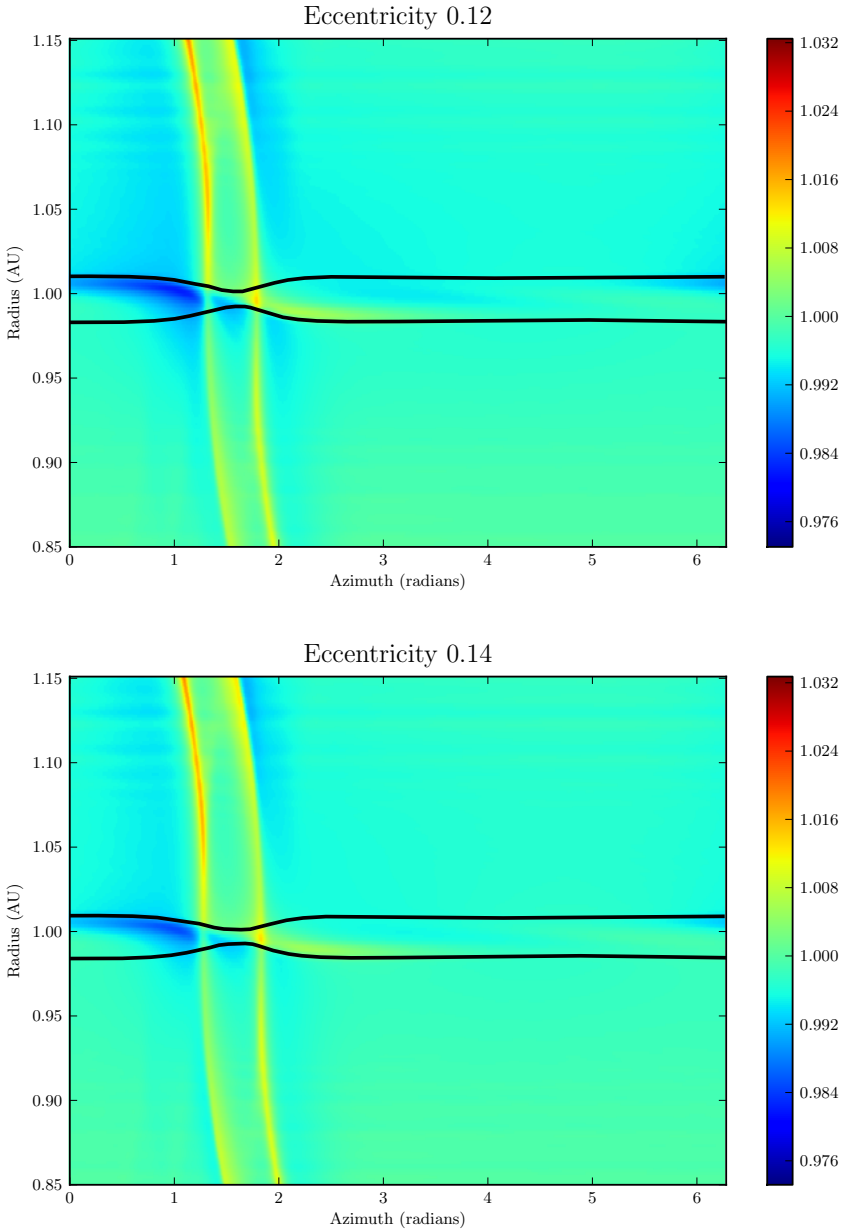

Figure 3.25: A $5M_\oplus$ planet in a $H/r = 0.07$ disc, with unsaturated corotation torque. Eccentricities of 0.12 and 0.14 are shown here. The quantity plotted is the perturbation to the equilibrium density ρ_0/ρ and the last circulating streamline on either side, as defined in the text, is overplotted.

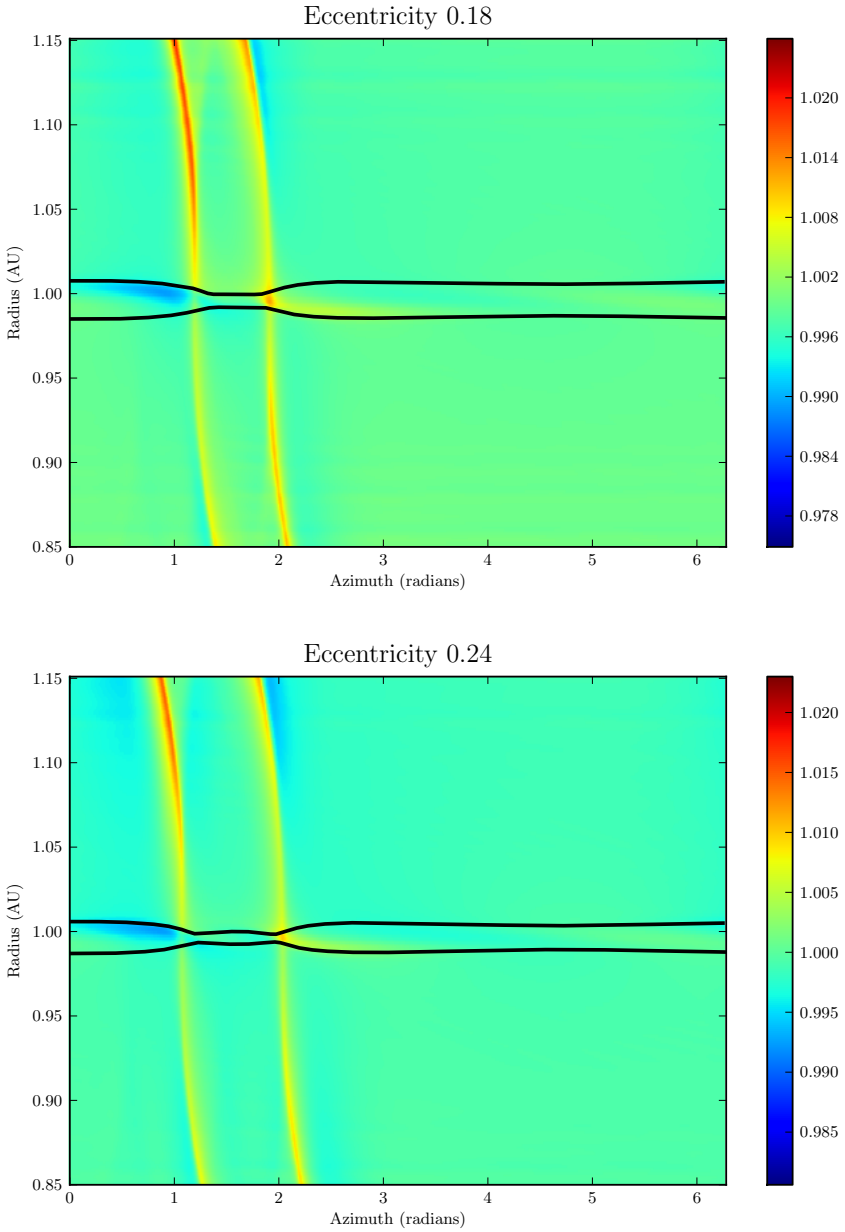

Figure 3.26: A $5M_\oplus$ planet in a $H/r = 0.07$ disc, with unsaturated corotation torque. Eccentricities of 0.18 and 0.24 are shown here. The quantity plotted is the perturbation to the equilibrium density ρ_0/ρ and the last circulating streamline on either side, as defined in the text, is overplotted.

3.10 Fitting formulae

.

In this section and the next, we analyse the fits that demonstrate exponential decay of the corotation torque with increasing eccentricity that we have shown in the figures presented in the previous sections, and discuss discrepancies between some of our simulation results and this trend. We also discuss some limitations of our experimental method, and go on to show how our results are broadly consistent with previous work relating the corotation torque to the horseshoe width.

Before discussing the fitting procedure, we recall that the total corotation torque is given as a sum of the barotropic and entropy-related contributions: $\Gamma_{\rm c} = \Gamma_{\rm c,baro} + \Gamma_{\rm c,ent}$ (Paardekooper et al., 2011). Furthermore, these contributions to the unsaturated horseshoe drag scale with the width of the horseshoe region according to $\Gamma_{\rm c} \sim x_{\rm s}^4$. Both $\Gamma_{\rm c,baro}$ and $\Gamma_{\rm c,ent}$ depend on the relative time scales associated with horseshoe libration and the viscous/thermal diffusion time scales, as these determine the level of torque saturation. As we have discussed already, the width of the horseshoe region, $x_{\rm s}$, depends on the planetary eccentricity, so we might expect the magnitude of the corotation torque for an eccentric planet in a disc with fixed thermal and viscous evolution times to decrease through the $x_{\rm s}^4$ dependence, and to also decrease compared to the circular orbit case through changes in the level of torque saturation; i.e. the difference in optimal viscosity and entropy relaxation timescale due to the narrower horseshoe region and the longer libration time for the material contained near the separatrix thereof.

In principle it is possible to disentangle these two effects when fitting the results of the simulations, but this would require a CPU-intensive programme of runs in which the optimal values for the viscosity and thermal relaxation are sought for each value of planet eccentricity. We avoid this complication by fitting a simple function to the simulation results.

Denoting the corotation torque for a zero-eccentricity orbit as $\Gamma_{\rm c,e=0}$, normalised by Γ_0/γ, where we remind the reader that Γ_0 is given by equation 3.1, we fit the torque as a function of eccentricity using the expression

$$\Gamma_{\rm c}(e) = \Gamma_{\rm c,e=0} \exp\left(-\frac{e}{e_{\rm f}}\right). \tag{3.2}$$

We note that because of the normalisation by Γ_0 (defined in equation 3.1), the zero-eccentricity corotation torque is expected to be independent of q and h when in the linear regime. This is because the horseshoe width is expected to scale as $x_{\rm s} \sim \sqrt{q/h}$, cancelling the $(q/h)^2$ dependence contained in Γ_0. For larger values of q, or small values of h, however, the width of the corotation torque increases because of its sensitivity to the relative strengths of planet gravity and thermal pressure (Masset et al., 2006a; Paardekooper and Papaloizou, 2009b). This causes $\Gamma_{\rm c,e=0}$ to increase in our simulations as h decreases, as shown in figure 3.27 where we plot $\Gamma_{\rm c,e=0}$ versus h. We note that for $h = 0.05$, our value of $\Gamma_{\rm c,e=0}$ obtained with methods (i) and (iii) agrees well with the canonical value of 11.25 shown in figure 17 of the paper by Paardekooper et al. (2010), who also examined this issue. Furthermore, in that paper it was suggested that as q increases or h decreases, it is appropriate to change the value of the coefficient C in the expression

$$\frac{x_s}{r_{\rm p}} = \frac{C}{\gamma^{0.25}} \left(\frac{b/h}{0.4}\right)^{1/4} \sqrt{\frac{q}{h}} \tag{3.3}$$

from $C = 1.1$ in the fully linear regime to, e.g., 1.3 in the quasi-nonlinear regime to account for this effect in the torque formulae. We discuss in section 3.11.5 our horseshoe width compared to the one expected from this expression.

We now consider fitting the characteristic e-folding eccentricity, $e_{\rm f}$. In figure 3.28 we plot the best fitting values of $e_{\rm f}$ obtained using each of the methods (i), (ii) and (iii) as a function of the disc aspect ratio h. Methods (i) and (iii) give very similar values, and method (ii) gives values that are offset slightly but with a similar slope. All methods give an approximately linear relation between $e_{\rm f}$ and h. The superimposed line in the plot is given by

$$e_{\rm f} = h/2 + 0.01, \tag{3.4}$$

Using this relationship, and the one in equation 3.2, it is possible to obtain the corotation torque attenuation experienced by an eccentric planet.

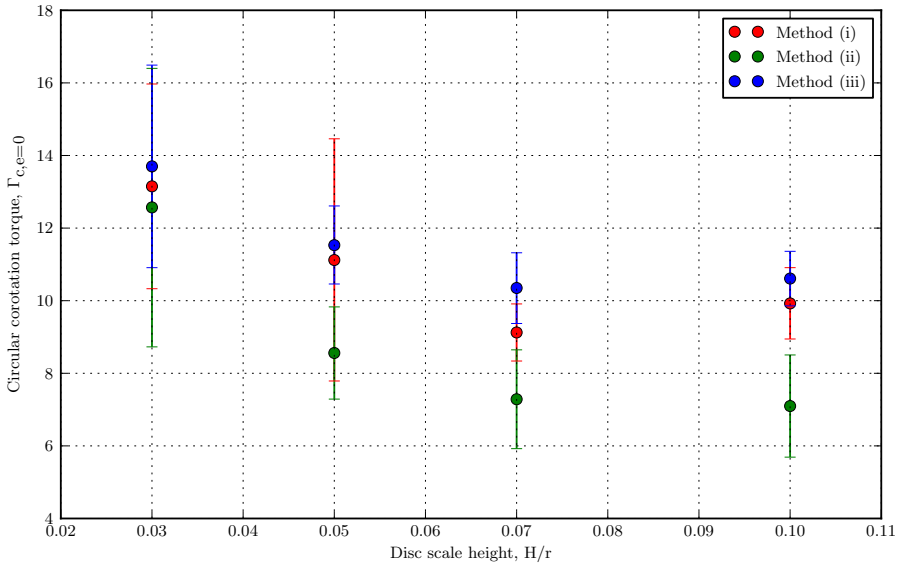

Figure 3.27: For the twelve simulations plotted as figures 4, 8, 9 and 10, we take the fits of the form $\Gamma_c(e) = \Gamma_{c,e=0} \exp\left(-\frac{e}{e_f}\right)$ and plot $\Gamma_{c,e=0}$ as a function of disc aspect ratio. Error-bars are taken from the 95% confidence intervals of the fits.

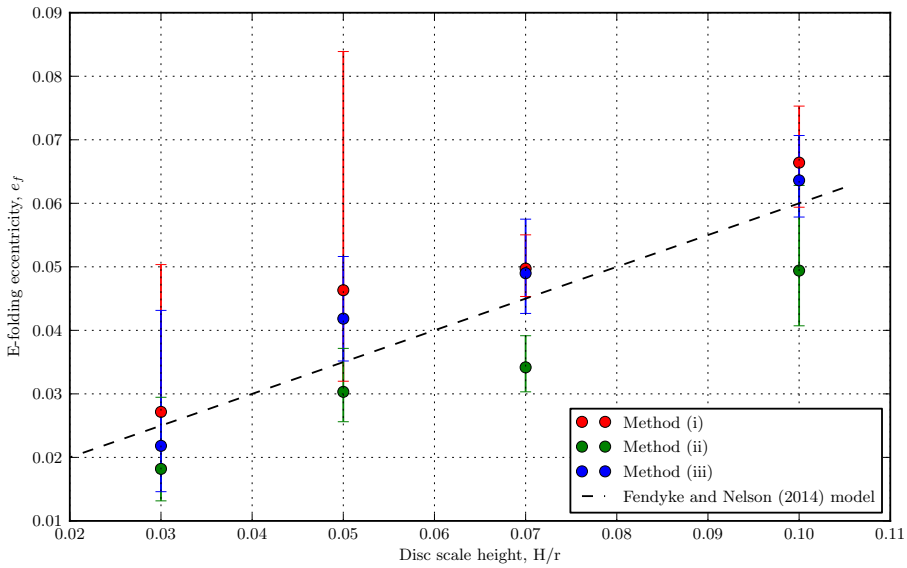

Figure 3.28: For the twelve simulations plotted as figures 4, 8, 9, 10, we take the fits of the form $\Gamma_c(e) = \Gamma_{c,e=0} \exp\left(-\frac{e}{e_f}\right)$ and plot e_f as a function of disc aspect ratio. Error-bars are taken from the 95% confidence intervals of the fits. We superimpose a simple linear fit of $e_f = h/2 + 0.01$.

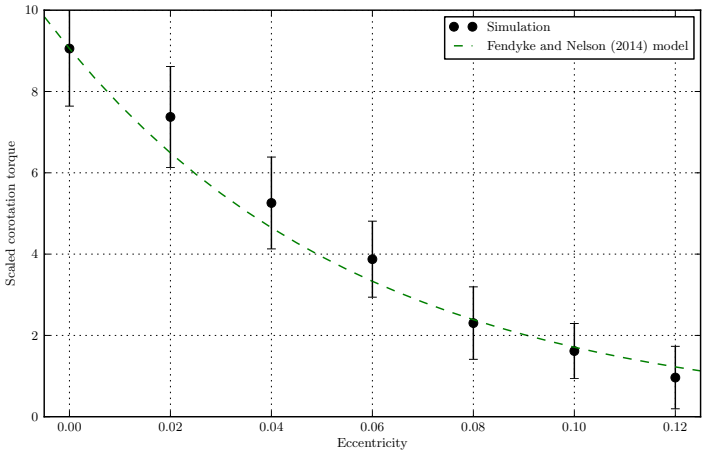

Figure 3.29: Corotation torque for a $10M_\oplus$ planet embedded in a $h = 0.10$ disc, measuring using our method (iii). Error bars are given to 1σ. We superimpose a fit of the form $\Gamma_c(e) = \Gamma_{c,e=0} \exp(-e/e_f)$, using e_f from equation 3.4, derived from a study of $5M_\oplus$ planets.

3.10.1 Test: A $10M_\oplus$ Planet.

So far we have only considered variations in the disc aspect ratio and planet eccentricity, for which the fitting formulae presented in the previous section provide good overall fits to the data, as shown in the figures 3.13, 3.17, 3.20 and 3.21. We now demonstrate that these fits also give good results when applied to a planet with $10M_\oplus$ instead of $5M_\oplus$; we select this planet mass for our test in order to ensure that the planet-disc interaction remains in the linear regime where we might reasonably expect the derived fitting formula to apply. Figure 3.29 shows the corotation torque estimated using method (iii) from simulations with $h = 0.1$ and a planet with $m_p = 10M_\oplus$. We observe that the fitting formulae given by equations 3.2 and 3.4 give very satisfactory results for this case, suggesting that they can be used for a broad range of planet masses, eccentricities and disc aspect ratios. In particular, we note that the characteristic e-folding eccentricity depends only on the disc aspect ratio and not on planet mass, at least for the range of parameters that we have considered.

3.11 Discussion

3.11.1 Physical interpretation

Material at the edge of the horseshoe region, orbiting at a radial distance of x_s from the planet's location, will have a horseshoe libration time of

$$\tau_{lib} = \frac{8\pi a_p}{3x_s\Omega_p}. \tag{3.5}$$

As this is much longer than the orbital period of the planet, and its epicyclic motion in the rotating frame, we can say that material in the horseshoe region interacts with the planet on time scales that are long compared to the orbital period. The planet's potential, as experienced by the material librating with respect to it on horseshoe orbits, may therefore appear 'softened' due to its periodic radial excursion from the corotation radius when averaged over one horseshoe libration period. We tentatively suggest that this softening of the potential is responsible for the observed narrowing of the horseshoe width, x_s, as the eccentricity increases. An alternative hypothesis for the observed narrowing of the horseshoe region is that the excursion in azimuth of the planet as it undergoes epicyclic motion causes the horseshoe streamlines that approach the planet most closely to be disrupted. Given that these streamlines are the ones that define the outer edge of the horseshoe region, this would cause the horseshoe region to narrow. We have examined the horseshoe streamlines in some detail for increasing values of the planet eccentricity and can confirm that this is not the case. Instead, we observe that as the eccentricity increases the azimuthal location of the horseshoe u-turns moves away from the planet in a smooth manner.

The interpretation that the corotation torque decreases with increasing eccentricity because of effective gravitational softening leads us to view the eccentricity as the dimensionless length scale associated with epicyclic motion. Consequently, we expect on physical grounds that the e-folding eccentricity, $e_{\rm f}$, will depend on a characteristic length scale in the problem. In a real three-dimensional disc there are only two natural length scales that may influence the corotation torque, these being the horseshoe width for a circular orbit, x_s, and the local pressure scale height, h. In earlier work, Hellary and Nelson

(2012) suggested that the decrease in the corotation torque with increasing eccentricity observed by Bitsch and Kley (2010) was due to the planet moving outside of the horseshoe region, leading to the assumption that the important parameter in the problem is e/x_s. The simulations of Bitsch and Kley (2010) adopted parameters such that $x_s \sim h$, so determining whether e/x_s or e/h is the important parameter is difficult from their work. Our simulations have been designed to specifically address this question, and show unambiguously that e/h is the important parameter because the e-folding eccentricity is a linear function of the scale height through $e_{\rm f} = h/2 + 0.01$. Indeed, x_s decreases as h increases due to the pressure in the disc acting as a buffer against the gravitational potential of the planet, so there is no room for doubt from our simulations about whether it is e/h or e/x_s that controls the rate at which the corotation torque decreases as the eccentricity increases. The buffering influence of the pressure explains why e/h determines the magnitude of the corotation torque: the eccentricity of the planet is competing with the pressure in determining the width of the corotation region, so for appreciable changes in x_s to occur it seems that e must be comparable to h.

3.11.2 The softening parameter: Investigation

In order for two dimensional hydrodynamic simulations to produce results comparable to those conducted in three dimensions, it is necessary to introduce a gravitational softening parameter, b, to compensate for absent 3D effects. This parameter is taken to be a linear function of the local height of the disc, typically on the order of a fraction of h. As described earlier, we use $0.4h$ for this work.

Given our tentative physical explanation of why the corotation torque decreases with eccentricity given in section, based on the idea that the epicyclic motion of the planet induces an effective softening of the planet potential, we are here motivated to examine whether or not the softening parameter, b, or the scale height, h, are most important for setting the scaling of $e_{\rm f}$, the e-folding eccentricity used in our analytical fits. To this end, we ran a series of simulations of a $5{\rm M}_\oplus$ planet embedded in a $h = 0.07$ disc, with values of b/h between 0.2 and 0.8. We again perform fits of the form $\Gamma_c = \Gamma_{c,e=0} \exp\left(-e/e_{\rm f}\right)$, and show these superimposed on the data in the left panel of figure 3.30. We note that using a small value of $b/h = 0.2$ can also lead to non-linear restruc-

turing of the disk, similar to described in section 3.8, explaining the outlying points at eccentricity values $e = 0.1$ and 0.12.

The values we obtain for the parameter $\Gamma_{c,e=0}$ are shown in the middle panel of figure 3.30. We note that in the circular orbit case, we expect the corotation torque to scale as x_s^4, and therefore as $\frac{1}{b/h}$, and our data are consistent with this. The e-folding eccentricity values, $e_{\rm f}$, are shown in the right panel of figure 3.30 as a function of b/h. We observe no obvious trend, and the best fitting values appear to be independent of b/h. We note, however, that using equation 10 ($e_{\rm f} = h/2 + 0.01$) yields a value $e_{\rm f} = 0.045$ for this $H/r = 0.07$ disc, which is consistent with the results shown in the lower panel of figure 3.30.

We discuss these results in the next subsection.

3.11.3 The softening parameter: Analysis

Our simulations are two-dimensional and require the use of a gravitational softening parameter, b, whose primary role is to allow two-dimensional results to agree with three-dimensional simulations by accounting for missing 3D effects. Normally, b is chosen to be a linear function of H, with values typically being on the order of $0.4H$ as in this work. The introduction of b brings another length scale into the problem that may influence the scaling of the corotation torque with eccentricity. We present a suite of runs in section 3.11.2 to examine this, where the scale height remains constant at $h = 0.07$, b/h takes values from 0.2 up to 0.8, and for each value of b/h the eccentricity takes on values between $e = 0$ and $e = 0.12$. We follow the same procedure described in section 3.10 in obtaining a fit to the corotation torque ($\Gamma_{\rm c}(e) = \Gamma_{c,e=0} \exp\left[-e/e_{\rm f}\right]$), and examine whether or not $e_{\rm f}$ can be expressed as a linear function of dimensionless b. Our results demonstrate that this is not the case. At best $e_{\rm f}$ is a very weak function of b, and is consistent with our original fit $e_{\rm f} = h/2 + 0.01$. This result demonstrates that it is the scale height, h, and not the softening, b, that determines the behaviour of the corotation torque as e increases in our simulations. Although the reason for this is not entirely clear, we suggest that the primary reason is that the width of the horseshoe region x_s is being controlled primarily by the scale height, h, rather than the softening parameter, b, in most of our runs, so that the softening effect introduced by increasing the eccentricity is competing with h rather than b. Some support for this inter-

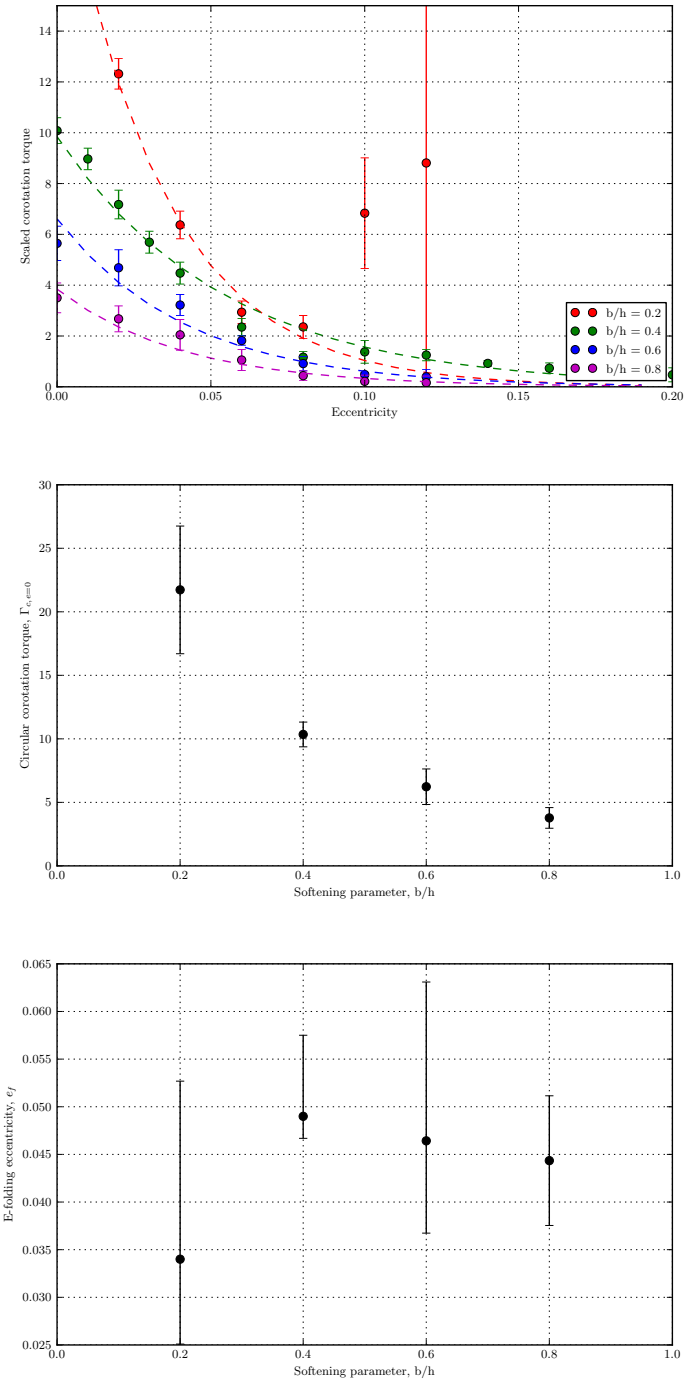

Figure 3.30: **Upper panel:** The corotation torque on a $5M_\oplus$ planet in units of Γ_0/γ obtained using method (iii). We superimpose fits of the form $\Gamma_c = \Gamma_{c,e=0} \exp(-e/e_f)$ over these data. **Middle panel:** We show the parameter $\Gamma_{c,e=0}$ from the fits shown in the left panel, as a function of softening, b/h. **Lower panel:** We show the parameter e_f from the fits shown in the upper panel, as a function of the softening, b/h.

pretation is provided by the fact that x_s has a stronger functional dependence on the scale height, h, than on the softening, b.

If this interpretation is true then it implies that there is a range of values of b for which the softening plays the most important role in controlling x_s, and for that range of values we would expect e/b to control the rate at which the corotation torque decreases as e increases. The values of b for which this is true are likely to be significantly larger that $0.4H$, meaning that this parameter regime lies outside of the range of models that closely mimic the behaviour expected for 3D simulations that require $b \sim 0.4H$.

We note that the previously mentioned gravitational softening due to the planet's epicyclic motion can be observed to operate in our simulations by comparing runs on a case by case basis. For an eccentric orbit the apparent softening length is $b_*^2 = b^2 + e^2a^2$. We therefore expect that, for example, a $5\mathrm{M}_\oplus$ planet on a circular orbit in a disc with $h = 0.07$ with $b/h = 0.8$ will exhibit the same corotation torque as a run with $b/h = 0.4$ and $e = 0.0485$, and this is indeed found to be the case in our runs within the margin of error involved in measuring corotation torques. This adds further weight to the physical interpretation described above.

We conclude that the key physical quantity that determines the behaviour of e_f is the disc scale height h. The softening parameter, b, plays the important role of allowing 2D simulations to produce results that are consistent with 3D simulations, but does not play an important role in determining how the corotation torque scales with orbital eccentricity. We test this further in the next chapter in which we conduct full 3D simulations of similar discs.

3.11.4 Horseshoe width against corotation torque

Finally, we now discuss how consistent our results are with the interpretation that the corotation torque decreases because the horseshoe width narrows with increasing eccentricity. As mentioned already in the analysis by Ward (1991), and later work by Masset (2001) and Paardekooper et al. (2010), the width of the corotation region is related to the corotation torque by the scaling:

$$\Gamma_c \sim x_s^4. \tag{3.6}$$

In figure 3.32, we attempt to fit just such a scaling to our torque measurements obtained using method (iii), normalised to match the measured torque at zero-eccentricity. Although the overall scaling, covering the full range of eccentricity values considered, is reasonably well captured by the curves, it is clear that the corotation torques in the simulations fall off faster than predicted by the x_s^4 scaling. One possible explanation for this is that the narrowing of the horseshoe region causes the thermal relaxation time and viscosity in the simulations to be no longer optimal for unsaturating the torque, leading to a further reduction in its value beyond the fall off predicted by the x_s^4 scaling.

3.11.5 Comparison to Paardekooper et al. (2010)

It should be noted that not only do we obtain a somewhat lower corotation torque in the circular case than expected from the torque formula of Paardekooper et al. (2010), but we also find that when the suggested parameter $C = 1.1$ is used in their euqation 44 to calculate horseshoe width, the result underestimates the value we obtain, as shown in figure 3.31. We find that for the simulations used here, $C = 1.3 - 1.4$ is found to be more appropriate for all disc thicknesses.

Using the prescription for corotation torque as a function of horseshoe width from the same paper, however, overestimates the corotation torque even when the parameter $C = 1.1$ is used. For this reason, we retain the scaling $\Gamma_c \sim x_s^4$ but normalise the resulting torque to our measured value, as shown in figure 3.32

3.11.6 Corotation torque set-up timescale

A planet on a circular orbit migrating because of tidal interaction with the disc will retain the material in the horseshoe region as it migrates. Consequently the corotation torque will evolve gradually as the semi-major axis changes. A planet that experiences a very rapid change in its position in the disc, however, due to planet-planet scattering, will set up a new corotation region with material undergoing horseshoe libration. The scattering will likely leave the planet in an eccentric orbit initially when it lands at the new semi-major axis, so the growth of the new corotation torque will occur on the time scale

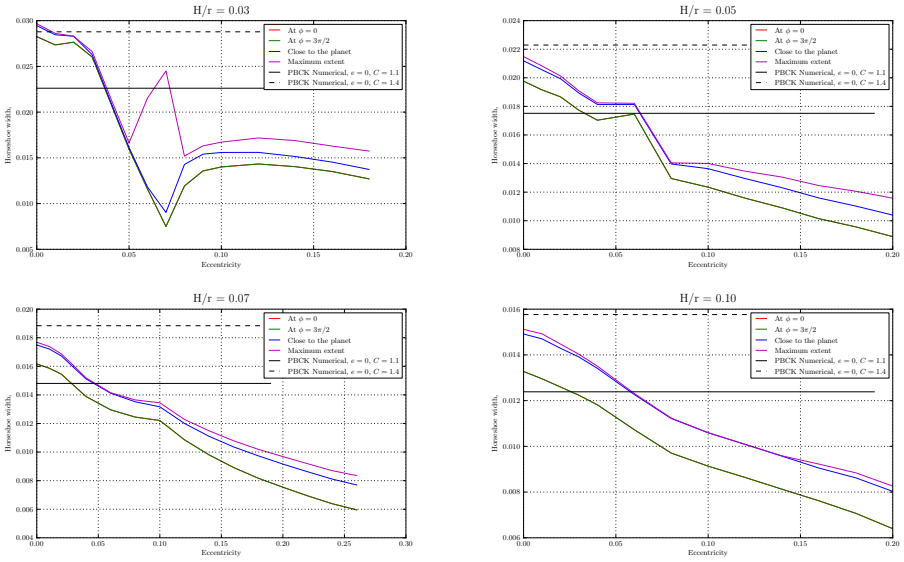

Figure 3.31: For all our disc aspect ratios, we plot the measured horseshoe width in our simulations, compared to equation 44 of Paardekooper et al. (2010). Different measures of the horseshoe width are used: **(red line)** x_s at $\phi = 0$; **(green line)** x_s at $\phi = 3\pi/2$; **(blue line)** x_s close to the planet; and **(purple line)** the maximum extent of x_s.

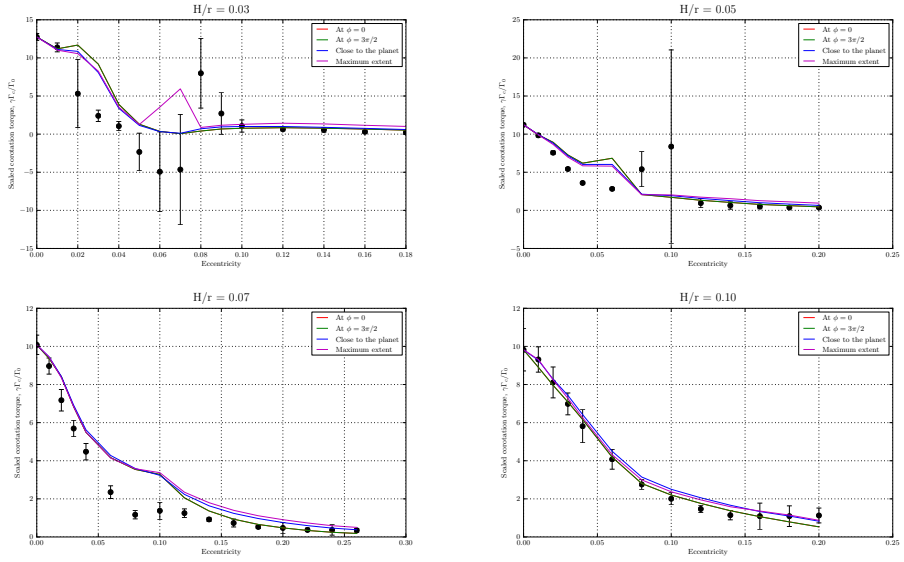

Figure 3.32: For all our disc aspect ratios, we plot the corotation torque against eccentricity as measured by method (iii), with 1σ error bars, as well as the corotation torque predicted by a simple scaling, normalised to the measured torque at $e = 0$ and decaying as x_s^4. Different measures of the horseshoe width are used: **(red line)** x_s at $\phi = 0$; **(green line)** x_s at $\phi = 3\pi/2$; **(blue line)** x_s close to the planet; and **(purple line)** the maximum extent of x_s.

for eccentricity damping, followed by the libration time scale given by equation 3.5 as the planet tends toward a circular orbit. In general, standard type I migration time scales are on the order of 10^4 orbits for 1 $M_\oplus$ planets, and $\sim 10^3$ orbits for 10 $M_\oplus$ bodies (e.g. Tanaka et al., 2002). The eccentricity damping time scale is typically a factor $\sim (H/r)^2$ shorter than the migration time (Tanaka and Ward, 2004), bringing it close to the time scales for horseshoe libration for low mass planets. As such, the damping of eccentricity and growth of the corotation torque will occur on similar time scales. In principle, these are issues that should be accounted for in N-body simulations of planetary formation that include prescriptions for corotation torques, if planet-planet scattering plays an important role.

3.12 Conclusion

In this chapter we have presented a suite of simulations that were designed to examine how the steady disc-induced corotation torque varies as a function of planet orbital eccentricity for low mass planets embedded in protoplanetary discs. We considered disc models with four different aspect ratios, and used three different methods to estimate the corotation torque. In agreement with previous work (Bitsch and Kley, 2010), we find that the corotation torque decreases as the orbital eccentricity increases. We provide an analytical fit to the numerically-obtained corotation torques as a function of eccentricity, and find that they are well-fitted by a simple exponential decay with e-folding eccentricity that scales linearly with the disc aspect ratio.

Through inspection of time-averaged fluid streamlines we find that the fluid in the corotation region continues to undergo horseshoe orbits when the eccentricity is non-zero. As the eccentricity increases we find that the horseshoe region narrows, and we suggest that this is the major reason why the corotation torque decreases with increasing eccentricity, since the non-linear horseshoe drag, Γ_c, is known to scale as $\Gamma_c \sim x_s^4$. When plotting the measured values of Γ_c against the measured values of x_s we find that the corotation torques from the simulations drop off more rapidly than suggested by the x_s^4 scaling. We tentatively suggest that the changing width of the horseshoe region causes the adopted values of thermal relaxation time and viscosity in the simulations to become suboptimal for fully unsaturating the corotation torque, causing the

torque to be smaller than predicted by the x_s^4 scaling.

While previous work (e.g. Hellary and Nelson, 2012) has made use of a simple model of corotation torque as a function of eccentricity, wherein the parameter governing the torque attenuation is e/x_s, we have shown instead that the torque decays as e/e_f, where e_f can be modelled as a linear function of the disc aspect ratio. This latter scaling produces a less severe drop-off in the magnitude of the corotation torque with eccentricity, as the scale height is generally larger than the horseshoe width for low mass embedded planets. The fitting formula we have provided should therefore provide a useful addition to N-body models of planet formation that implement type I migration prescriptions including corotation torques, especially if planet-planet scattering events are important.

Our results have implications for the notion of "zero torque radii" occurring in discs at locations where the (outward) corotation torque balances the (inward) Lindblad torque. Such locations may be important during planetary formation by acting as 'traps' where planetary building blocks may congregate, enhancing accretion. While the locations of these zero torque radii depend on the the properties of the local disc sufficiently optimising the corotation torque, we have shown that a relatively modest planetary eccentricity can have an effect on the torque experienced by the planet, moving the location of zero torque radii, or even removing them entirely if the eccentricities become large enough, resulting in a qualitative effect on planetary migration and formation. One particular scenario where this may be important is in the formation of circumbinary planets, where the disturbing influence of the central binary may excite significant eccentricities, as considered recently by Pierens and Nelson (2013) in application to the Kepler-16, 34 and 35 systems.

Furthermore, as eccentricities are often excited by planetary bodies in mean motion resonance, our work has implications for pairs of planets being able to remain in resonance after having their eccentricities excited, and therefore on the subsequent evolution of such a system. For example, a pair of planets may migrate convergently into resonance, because of the influence of corotation torques, excite their mutual eccentricities, and then migrate divergently such that the resonance is not maintained. Subsequent damping of the eccentricity will then cause this process to repeat, keeping the system near to, but not actually in resonance. Such a mode of evolution could potentially explain the compact systems of low-mass planets discovered by the Kepler mission (e.g.

Kepler-11, described by Lissauer et al., 2011) which are close to, but not in resonance.

This work has been limited in using a simple thermal model in a 2D disc; in the next chapter, we revisit some of the issues raised in a 3D disc.

Summary

- We find the corotation torque attenuates with eccentricity in a manner that can be fitted by an exponential decay with an e-folding eccentricity that goes linearly with disc scale height, between $H/r = 0.03$ and $H/r = 0.10$. This is contrary to the assumption of previous work.
- We suggest that the eccentricity is competing with the pressure forces, determined by the disc height, to set horseshoe width. Thus, $e \sim h$ is necessary for appreciable changes in x_s and Γ_c.
- The decrease in corotation torque is associated with the narrowing of the corotation region between circulating streamlines.

Chapter 4

The Corotation Torque in 3D

In this chapter, the second of the projects that make up my PhD is presented; an extension of the investigation described in the previous chapter into three dimensions. Our simulations are described and then the results are presented and discussed. Our empirical relation betwen eccentricity and the corotation torque is demonstrated to hold in three dimensions. Using time-averaged density and velocity fields, we comment on the three-dimensional structure of the corotation region,

This work is being prepared for publication by Fendyke and Nelson (in prep.).

The work presented in the previous chapter provides an answer to the open question of the behaviour of the corotation torque for low-mass eccentric planets, but it rests on a model in which are contained a number of assumptions; not least, that a simulation of a two dimensional disc with a softening parameter can accurately model the response of a three dimensional disc to a planet for the purposes of studying the corotation region. It is by no means clear that this is in fact the case, and this inspires us to investigate the problem in three dimensions, at least to the extent that we know whether or not we can be confident in the fitting formula we obtained in the previous chapter.

In section 4.1, we set out the aims of this project; in section 4.2 we review some of the relevant background from the introduction and perform some relevant background calculations; in section 4.3 we describe our model and include a resolution study; in section 4.4 we describe the suite of simulations

we performed; in secton 4.5 we describe the behaviour of the corotation torque with eccentricity in these simulations; in section 4.6 we describe the vertical disc structure as seen in our time-averaged density fields; in section 4.7 we investigate the width of the corotation region as a function of altitude in the case of a planet on a circular orbit; in section 4.8 we repeat the analysis of the previous section in the case of eccentric orbits; and finally in section 4.9 we discuss our results in context and conclude.

Note that in this chapter the cylindrical radius will be denoted by R and the spherical radius will be r.

4.1 The Aims

In this project, we aim to ascertain whether or not the empirical relationship obtained in the previous chapter between the corotation torque and planetary eccentricity for low-mass embedded planets holds in three dimensions. We further aim to investigate the width of the corotation region as a function of height in the disc, for different disc scale heights and planetary eccentricities.

4.2 Background

Tanaka et al. (2002) studied isothermal protoplanetary discs and ascertained that the Lindblad torque in three dimensional discs is generally weaker than in two dimensional discs. As their work used an isothermal disc, they do not measure the full non-linear corotation torque including its entropy-related component.

Bitsch and Kley (2010) have previously measured the corotation torque in three dimensional discs with radiative transfer for $20\mathrm{M}_{\oplus}$ planets with eccentricities in the range $0 \leq e \leq 0.4$ at 5.2 AU in a disc of scale height $H/R = 0.037$. They find, as described earlier, that the corotation torque attenuates, essentially vanishing for $e > 0.15$ in their simulations.

No complete survey exists of the parameter space of planet and disc properties for the corotation torque. The author is not familiar with any work describing the vertical structure of the corotation region in a disc with an embedded

planet of a mass below the threshold at which we expect a non-linear disc response.

Pierens and Nelson (2010) studied dead zones in the context of accretion of gas onto planetary cores in protoplanetary discs using the model of a layered disc; one in which the viscosity parameter α has a dependence on H in the disc. They found that while the timescale for the growth of a giant planet was independent of the presence of a dead zone in the disc, the migration speed is $\sim 40\%$ slower in a disc with a dead zone which extends vertically to $2.3H$. Recent work by Bitsch et al. (2014) has used a similar approach to study the effect on migration of viscosity transitions in a protoplanetary disc using two dimensional simulations (in the $r - z$ plane); they find that disc density transitions are created by the viscosity transitions, and that these density transitions can act as planet 'traps' for smaller migrating planets.

There remains an open question about the dependence of the corotation torque on different prescriptions for the dead zone; *prima facie* evidence as described above suggests that a variation in the maximum vertical extent of the corotation region in a disc with a dead zone might have an effect on the overall corotation torque. We return to this idea in section 4.9.

4.2.1 From surface to volume density

Where in a two dimensional disc, we evolve the surface density, σ, of a disc using the hydrodynamic equations, in three dimensions we must consider the volume density, ρ. One of the issues in moving from a two dimensional disc to a three dimensional disc and trying to compare results is that of ensuring the surface density of the former can be directly compared to the volume density of the latter. As the disc scale height changes with radial extent, a midplane volume density power law set to match the surface density power law of a two dimensional simulation will yield significantly different results. In order to compare discs simulated in full 3D with those simulated in two dimensions, it is helpful to consider the relationship between σ and ρ.

On simple dimensional grounds, $[ML^{-2}] \sim [ML^{-3}][L]$;

$$\sigma \sim \rho H, \tag{4.1}$$

where H is the height of the disc.

If we have a disc where $\rho \sim R^p$ and $T \sim R^q$, we note that the square of the sound speed,

$$c_s^2 \sim T \sim R^q.$$

Using

$$c_s = H\Omega,$$

we also have that

$$R^{\frac{q}{2}} \sim HR^{-\frac{3}{2}},$$

which gives

$$H \sim R^{\frac{q+3}{2}}.$$

Equation 4.1 then gives us that

$$\sigma \sim R^p R^{\frac{q+3}{2}}. \tag{4.2}$$

Thus, to obtain a disc with an initial surface density profile of R^s, given a temperature distribution of R^q, we require a midplane *volume* density profile of R^p where $s = \frac{q+3}{2} + p$. For example, a surface density power law of $s = -0.5$ to match the simulations discussed in chapter 3, assuming a temperature power law of $q = -2$, requires a volume density of $p = -1$.

More precisely, the surface density in the disc can be obtained by integrating the volume density over the entire thickness of the disc;

$$\sigma = \int_{-\infty}^{\infty} \rho_{mid} \exp\left(-\frac{z^2}{2H^2}\right) \mathrm{d}z, \tag{4.3}$$

which can be solved by noting that this is trivially the Gaussian integral, $\int_{-\infty}^{\infty} e^{-x^2}\,\mathrm{d}x = \sqrt{\pi}$, with a constant coefficient and a coordinate transformation in the variable being integrated over, to obtain the constant of proportionality in equation 4.1 above,

$$\sigma = \sqrt{2\pi} H \rho_{mid}. \tag{4.4}$$

This is of particular concern when comparing torque measurements; a 2D disc normalised to some σ_0 at $R = 1$ will have a different Γ_0 to a 3D disc with the midplane volume density initialised to the same value.

4.3 The Model

In chapter 2, we described the NIRVANA code, the 2D implentation of which we used in chapter 3. For this work, we use the 3D variant. We solve the hydrodynamic equations in spherical polar coordinates ($r \times \phi \times \theta$) and the simulations are computed in a frame of reference corotating with the planet, such that the planetary eccentricity manifests itself as epicyclic motion around a guiding centre.

We simulate a planet of mass ratio $q = 1.5 \times 10^{-5}$ (equivalent to $5\mathrm{M}_{\oplus}$ around a solar mass star) in a disc with temperature power law of $T = T_0 R^{-2}$. To obtain a power law in surface density comparable to that of the previous chapter, we set the midplane density power law to $\rho_{\mathrm{mid}} = \rho_0 R^{-1}$. We choose these values, as in the previous chapter, to obtain a large enough corotation torque to clearly measure. Our initial density and azimuthal velocity prescriptions are those described in section 1.2.5. We normalise our disc mass to $\rho_{\mathrm{mid},0} = 1.35 \times 10^{-3}$, although in the absence of self-gravity, this simply linearly scales the resultant torque. We set the adiabatic exponent, $\gamma = 1.4$.

Our planet is held at a fixed location of $(r, \phi, \theta) = (1, \frac{\pi}{2}, 0)$ in the rotating frame and we use the planet potential described in chapter 2.

We set our kinematic viscosity ν to 10^{-8} for the $H/r = 0.10$ disc and 10^{-7} for the $H/r = 0.05$ and 0.07 discs, consistent with obtaining sufficiently smooth time-series data to extract the corotation torque.

We assume symmetry about the midplane in altitude; by simulating only one half of the disc, we make more efficient use of our computation time. The boundary condition at the disc upper surface corresponds to a zero-gradient outflow condition. The azimuthal boundary conditions are periodic and we simulate the full 2π radians of the disc. In the radial direction we adopt reflecting boundary conditions at $r = 0.5$ and $r = 1.8$. As in the previous chapter, we use a wave-killing region after de Val-Borro et al. (2006) at the radial boundaries with a damping timescale of $\tau_{\rm damp} = 0.05$ for H/r of 0.05 and 0.07 discs, and $\tau_{\rm damp} = 0.03$ for $H/r = 0.1$. This is consistent with the greater sound speed in a thicker disc and the consequent requirement that the damping be more rapid.

We use an upper boundary of $\theta = 0.175$ radians ($\approx \pi/18 = 10°$) for the $H/r = 0.05$ disc (equivalent to just over 3.5 scale heights from the midplane) and for the thicker discs, we increase the boundary proportionally to always have the same resolution in terms of cells per scale height.

We determine the resolution of our simulations through a series of trials discussed in section 4.3.1. We decide on a resolution of $1032 \times 1032 \times 32$ ($r \times \phi \times \theta$), parallelised over 12 nodes of 48 cores each (that is, 576 processors) and where each simulation is run for 120 hours.

We use a softening length of the size of one cell, purely to avoid numerical singularities. This is distinct from the purpose of the softening parameter in 2D simulations, where it serves allow a 2D simulation to produce comparable results to a 3D disc and should be tuned accordingly. A result of this is that our softening length is tied to resolution and that the softening length is smaller for higher resolutions. We see the effect of this in our resolution study in that further increases in resolution continue to yield greater torque values beyond the limit where no further gains are found in the 2D case, where the softening is explicit and independent of resolution.

4.3.1 Resolution Study

In figure 4.1, we show our resolution study. Unlike with the 2D case, softening is not independent of resolution, so we do not expect convergence of torque at high resolution.

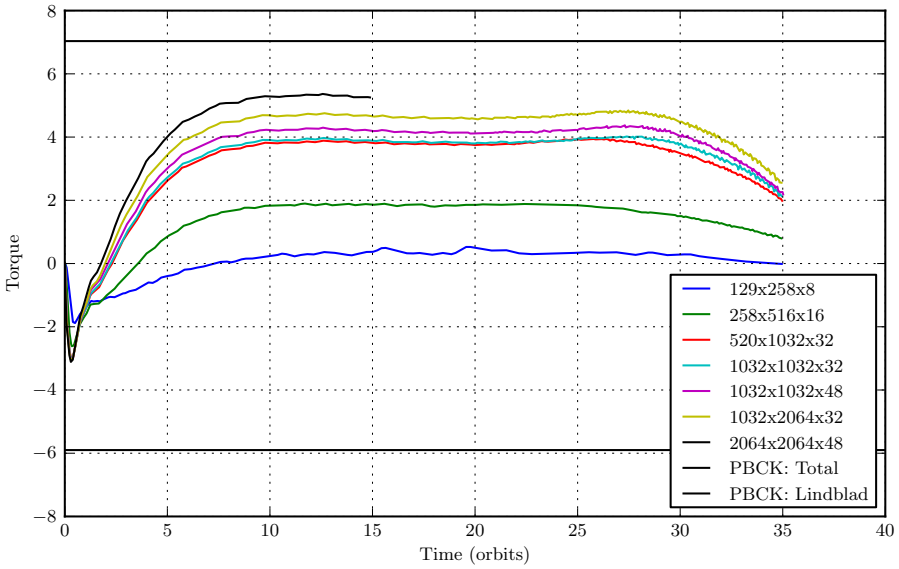

Figure 4.1: The resolution study for our 3D simulations, showing the first ~ 40 orbits for a variety of different resolutions. We find that as the resolution increases, we continue to find higher torque values, in a departure from the behaviour of the 2D case. This we attribute to the softening parameter being set to the cell size to avoid numerical singularities; as the resolution increases, the softening decreases and the potential becomes stronger.

We believe our set-up provides a balance between the requirement for a high resolution, the requirement to run a number of simulations to sufficiently explore the relevant volume of parameter space and the requirement to setup a problem that is computationally tractable.

We also show the torque calculated using the Paardekooper et al. (2010) formulae, based on 2D calculations and with a softening parameters, $b/h = 0.4$, in figure 4.1. We comment that precise agreement between 3D and 2D softened simulations is not expected, but that incresing the resolution yields improved agreement between the two. In their figure 3, Paardekooper et al. (2010) note that work by Tanaka in 3D gets significantly different results for the Lindblad torque in the case of steep temperature gradients. At the moment, no fitting formulae exist to give the corotation torque in a 3D disc.

4.4 Simulations

We computed disc models with disc aspect ratios $h \equiv H/r = 0.05, 0.07$ and 0.1. For each of these values of H/r, we consider eccentricity values of $e = 0$, 0.02, 0.04, 0.08 and 0.12. All simulations are of low-viscosity, adiabatic discs with no thermal relaxation parameter comparable to that in the previous chapter. A low viscosity adiabatic disc allows saturation of both the vortensity and entropy related contributions to the corotation torque as material in the horseshoe region becomes phase mixed and the vortensity and entropy gradients disappear. We use these simulations to estimate the corotation torque from torque time-series by using our method (iii) described in section 3.8.3.

As in the previous chapter, as the non-linear horseshoe drag is due to material undergoing horseshoe orbits, and the timescale for even the shortest horseshoe orbit is significantly longer than the planetary orbital period, we continually construct and record time-averaged density and velocity fields from the disc in all simulations for further analysis; we use these data to constuct maps of the time-averaged horseshoe trajectories in the disc.

4.5 Corotation torque with eccentricity in 3D

We measure the corotation torque using our method (iii), as described in chapter 3, for the disc thicknesses $H/r = 0.05$ and $H/r = 0.10$. In figures 4.2 and 4.3 respectively, we show these torques, shown in normalised torque units against the torques obtained for the same disc thickness by the same method in two dimensions from the previous chapter. We show in these figures fits using our fitting formula from chapter 3, $\Gamma_{\rm c} = \Gamma_{\rm c,e=0} \exp(-e/e_{\rm f})$, where $e_{\rm f} = h/2 + 0.01$, which we normalise to the measured torque in the case of the planet on a circular orbit, as no appropriate torque formulae exist for the corotation torque in an adiabatic disc in three dimensions.

We note that the empirical fit derived in chapter 3 fits these data remarkably well. The observed torque is slightly higher than the expected value at low eccentricity (~ 0.02) for both scale heights and slightly lower for greater eccentricities (~ 0.08), just as for the analogous two dimensional results. In both cases, the discrepancy is not much more than the error bars.

It also transpires that the magnitude of the corotation torque for a planet on a circular orbit in the three dimensional case is comparable to that in two dimensions for a disc of scale height $H/r = 0.05$: In units scaled by Γ_0/γ, the two dimensional simulation torque value from Paardekooper et al. (2010) for $e = 0$ is 11.2. In our simulations as shown in figure 3.27 in the same units, we find values of nearer 11–12 by methods (i) and (iii) and even as low as ~ 8.5 by our method (ii), though we expect that value to underestimate the true value for reasons discussed in chapter 3. In the 3D case, by comparison, we get 10.5, a value which is perfectly consistent. For the thicker disc of scale height $H/r = 0.1$, on the other hand, we find that our three dimensional simulations yield a corotation torque at zero eccentricity of 14–15, a substantially greater value than in the two dimensional case.

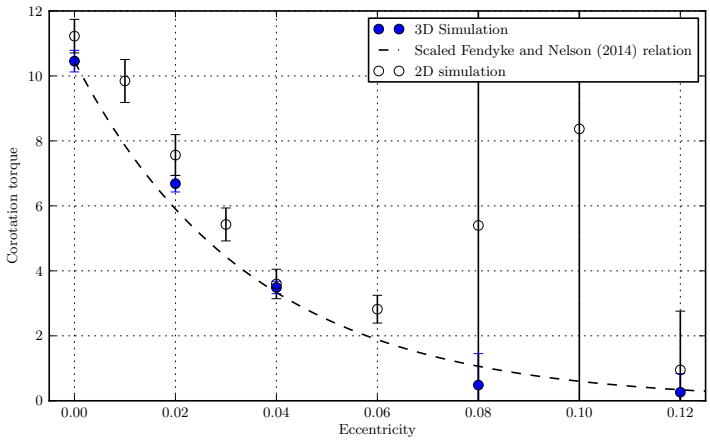

Figure 4.2: The corotation torque against eccentricity for a $H/r = 0.05$ disc as measured by our method (iii). Results from our 3D simulation are shown as blue circles, the results for the 2D case are white circles. Error bars shown 1σ in the measurement of the difference between the total torque and the Lindblad torque. The dotted line is the fit shown in figure 3.20, normalised to the measured torque value in three dimensions for a planet on a circular orbit, $\Gamma_c = \Gamma_{c,e=0} \exp(-e/e_f)$.

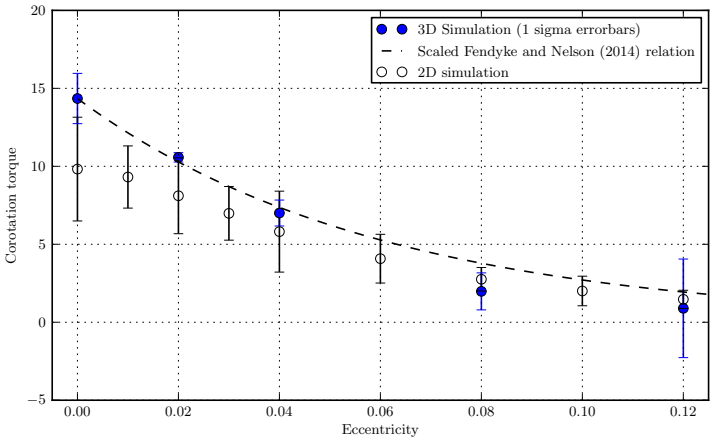

Figure 4.3: The corotation torque against eccentricity for a $H/r = 0.10$ disc as measured by our method (iii). Results from our 3D simulation are shown as blue circles, the results for the 2D case are white circles. Error bars shown 1σ in the measurement of the difference between the total torque and the Lindblad torque. The dotted line is the fit in figure 3.20, normalised to the measured torque value in three dimensions for a planet on a circular orbit, $\Gamma_c = \Gamma_{c,e=0} \exp(-e/e_f)$.

4.6 Vertical disc structure

An advantage of performing these hydrodynamic simulations in three dimensions is that it allows us to explore disc structure both in the midplane and as a function of altitude. In this section, we use the time-average values of density and the three components of velocity to investigate the vertical structure of the corotation region for a low-mass planet in a protoplanetary disc.

We plot disc density fields at different heights through the disc in figures 4.4, 4.5 and 4.6. With 32 cells in the θ direction, we show slices in the 1st, 9th, 17th, 25th and 32nd cells for different scale heights. The reader is reminded that as the disc scale height changes, the maximum extent of the computational domain is altered proportionally. Slices of the $H/r = 0.05$ disc are shown in figure 4.4, the $H/r = 0.07$ disc in figure 4.5 and the $H/r = 0.10$ disc in figure 4.6. On top of these density fields, we show disc velocity streamlines and the 'last circulating streamline' (defined analogously to its definition in chapter 3) and the maximum extent of this streamline as a line of constant r. We calculate this last circulating streamline by considering circulating streamlines to be defined as those started at $r > 1$, $\theta = 0$ that reach $\theta = 2\pi$ or at $r < 1$, $\theta = 2\pi$ that reach $\theta = 0$.

We see that the width and shape of the corotation region appears to be broadly independent of altitude, nicely confirming the assumption of Ward (1991) in the first work on the non-linear horseshoe drag in which he suggested that "we might vertically average the equations of motion ... this assumes that a column of disc material responds as a unit to the torque exerted on it"; an assumption repeated by every subsequent two dimensional disc simulation.

This assumption breaks down near the surface layer, where we see the appearance of an asymmetric horseshoe streamline morphology. We discuss this in the next section.

In the case of an eccentric planet, we see the same features as in two dimensions; the planet's spiral density wave splits into two strands, due to the density perturbation at apo- and pericentre. This is visible in figure 4.7.

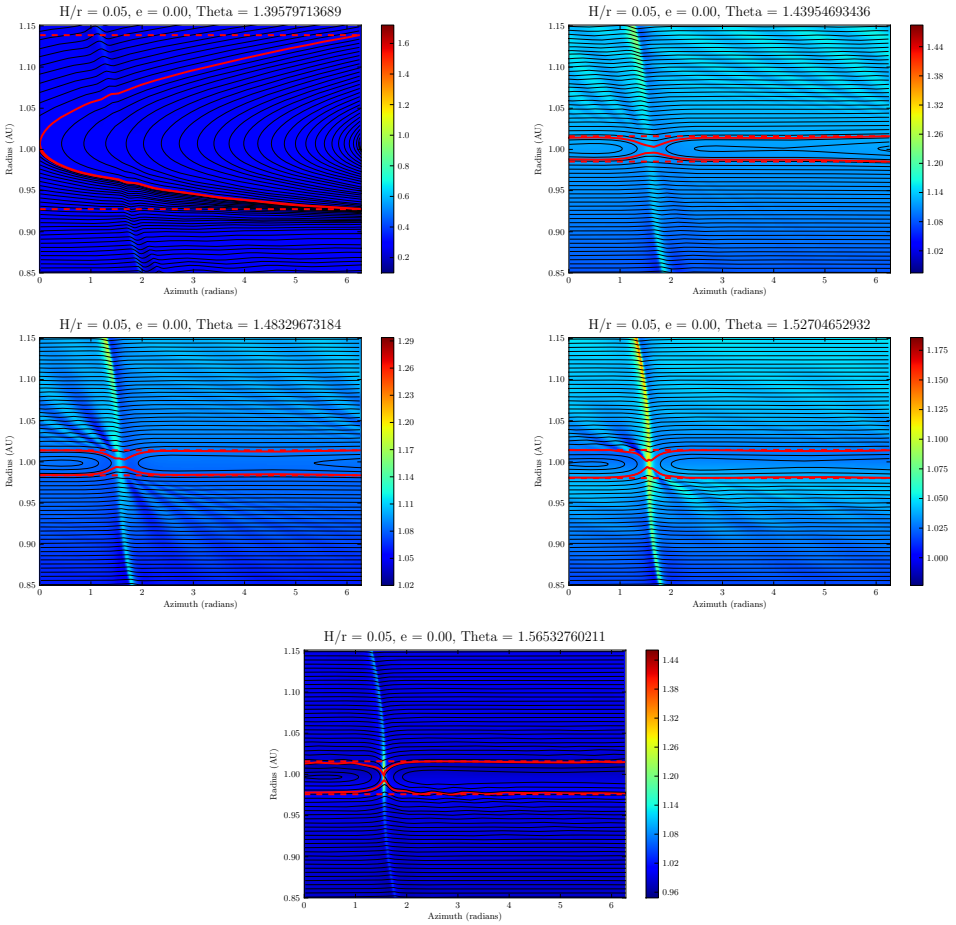

Figure 4.4: Vertical slices through a $H/r = 0.05$ disc. As the resolution in θ is 32 cells, we show here the 1st, 9th, 17th, 25th and 32nd cell slices. The maximum extent of the horseshoe region on each side is marked with a dotted line. The quantity plotted is the perturbation to the initial density and in this case the planet is on a circular orbit.

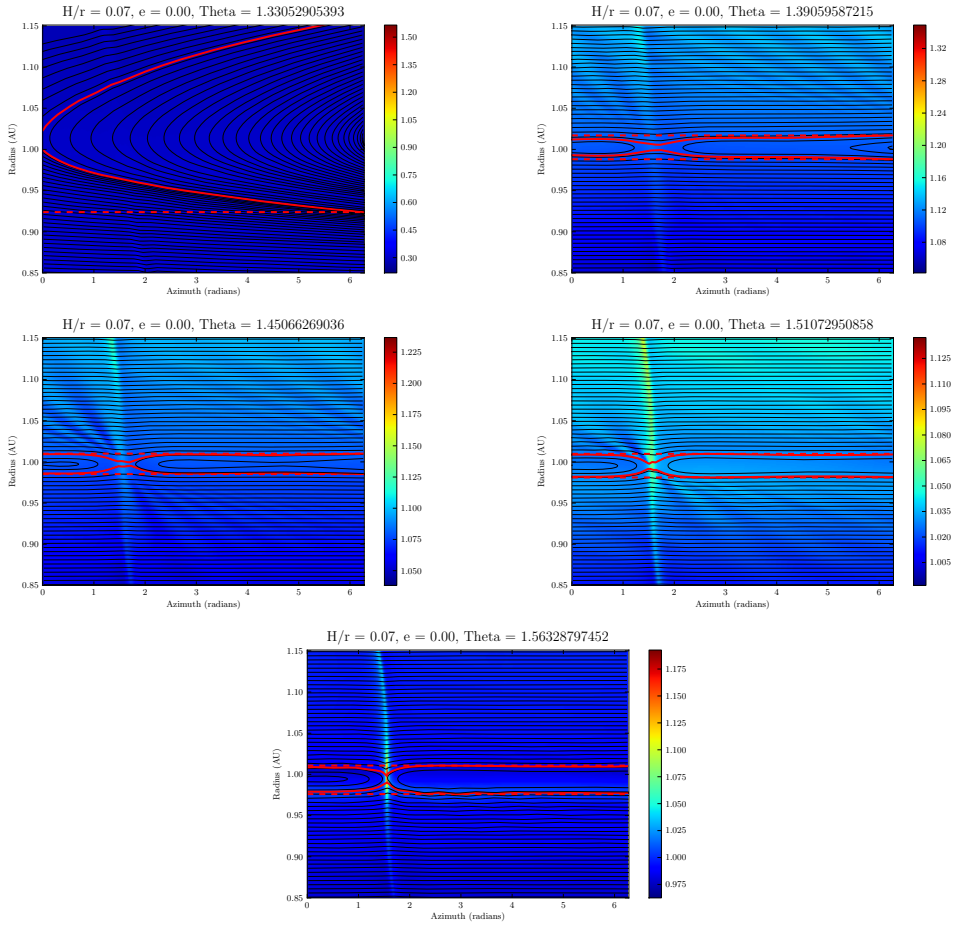

Figure 4.5: Vertical slices through a $H/r = 0.07$ disc. As the resolution in θ is 32 cells, we show here the 1st, 9th, 17th, 25th and 32nd cell slices. The maximum extent of the horseshoe region on each side is marked with a dotted line. The quantity plotted is the perturbation to the initial density and in this case the planet is on a circular orbit.

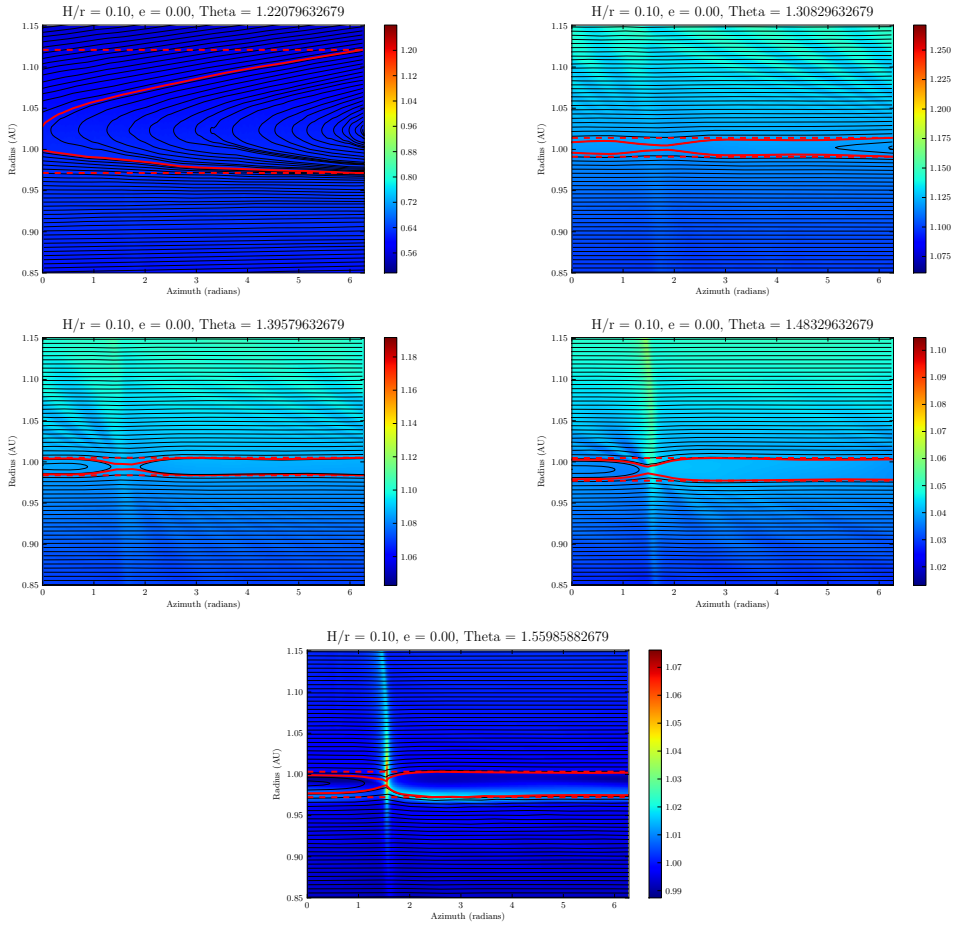

Figure 4.6: Vertical slices through a $H/r = 0.10$ disc. As the resolution in θ is 32 cells, we show here the 1st, 9th, 17th, 25th and 32nd cell slices. The maximum extent of the horseshoe region on each side is marked with a dotted line. The quantity plotted is the perturbation to the initial density and in this case the planet is on a circular orbit.

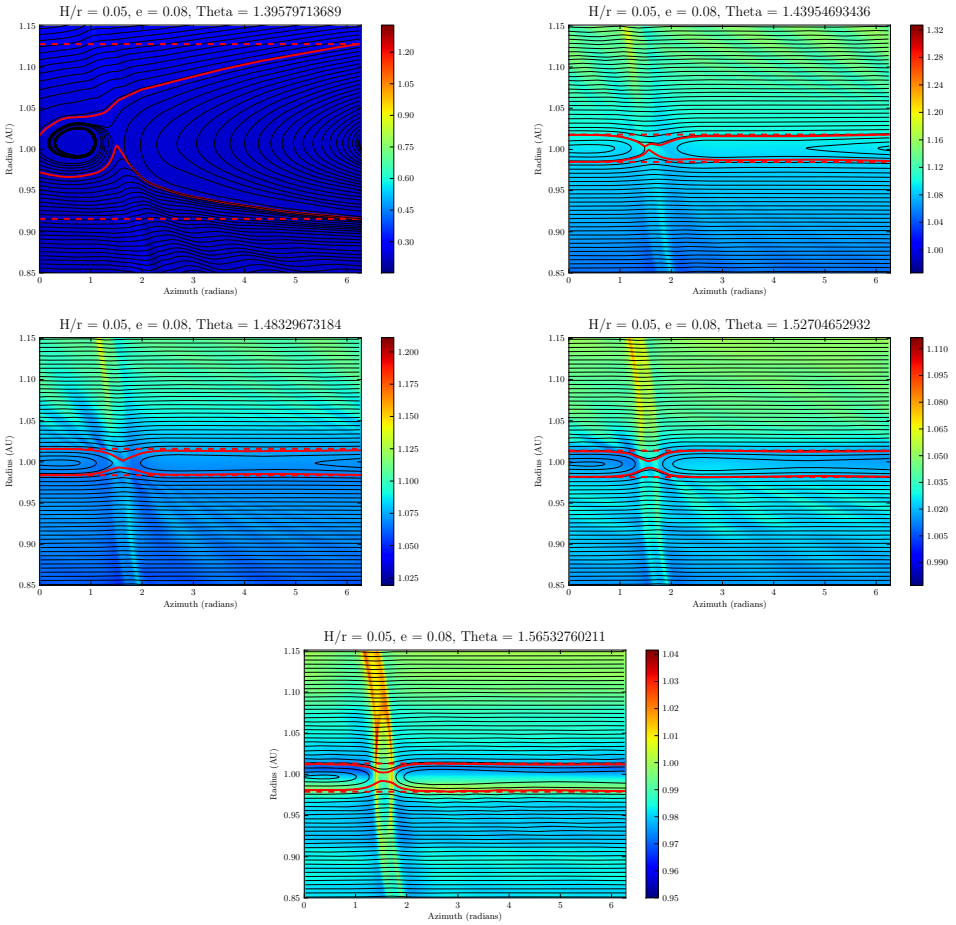

Figure 4.7: Vertical slices through a $H/r = 0.05$ disc. As the resolution in θ is 32 cells, we show here the 1st, 9th, 17th, 25th and 32nd cell slices. The maximum extent of the horseshoe region on each side is marked with a dotted line. The quantity plotted is the perturbation to the initial density and in this case the planet is on an orbit of eccentricity, $e = 0.08$.

4.7 Horseshoe width with height, circular orbit

While the width of the horseshoe region varies with azimuth, we can use the plotted 'maximum extent' of the horseshoe region on either side to estimate the horseshoe half-width as simply half the distance between the two extreme radial locations. These are plotted in figure 4.8 for all three disc scale heights in the case of a planet on a circular orbit. A clear similarity is apparent between the three cases.

We make a more appropriate comparison by noting that at constant q, the width of the horseshoe region is expected to scale with the inverse square root of the disc scale height; $x_s \sim h^{-0.5}$. The altitudinal coordinate, θ, also has a dependence on h as $\theta \sim h$. This suggests that we can replot figure 4.8 in coordinates of $x_s\sqrt{h}$ and θ/h to remove the expected scaling as shown in figure 4.9.

We observe that in these coordinates the width of the corotation region decays by only a few 10s of percent and almost linearly with altitude until around 2.5–3 scale heights, after which the width increases at an accelerating rate.

We can compare this measurement of the horseshoe width, x_s, to a number of different expressions for the horseshoe width in the literature, as introduced in section 1.5.1. These expressions are derived for two dimensional discs, and have a dependence on the prescribed softening parameter b/h. In figure 4.10, these are presented for comparison in the case of a $H/r = 0.05$ disc, as a function of b/h.

- **(1, black line)** This is the theoretical expression for the horseshoe width given by Paardekooper and Papaloizou (2009b), shown in the thesis as equation 1.20. This does not account for the disc being adiabatic or for back pressure, and so gives a wider value than we find in numerical simulations.
- **(2, red line)** In the limit of zero softening ($b \to 0$), equation 1.20 tends towards the expression given in equation 1.21.
- **(3, blue line)** In the limit $b \gg h$, equation 1.20 tends towards the expression given in equation 1.22.

- **(4, green line)** Paardekooper et al. (2010) present a value empirically obtained from two dimensional numerical simulations which they assert holds for b/h > 0.3. This value is consistently narrower than the theoretical value because the latter did not account for the disc being adiabatic and or include the effects of back pressure from Lindblad wakes, both of which narrow the corotation region.

- **(5, purple line)** We have our 3D results, shown earlier. We combine the results for all disc thicknesses, as figure 4.9 indicates that horseshoe widths for different disc scale heights can be compared when correctly scaled. We take the 'Fendyke, 3D' value to be the mean scaled horseshoe width below 3 scale heights, scaled by $0.05^{-0.5}$ to give the expected value for a $H/r = 0.05$ disc, with errorbars representing the standard deviation about this mean. We obtain $x_s = 0.0170 \pm 0.0028$.

We see that the measured horseshoe width is perfectly consistent with equation 1.23 (that is, equation 44 of Paardekooper et al., 2010) with a softening length of 0.4–0.5; see the dotted purple line, which intersects the numerical expression where $b/h = 0.459204$. This vindicates our choice of softening parameter used in chapter 3 and in other work, and confirms nicely that such a value of b is the correct choice for a 2D simulation to closely resemble a 3D one.

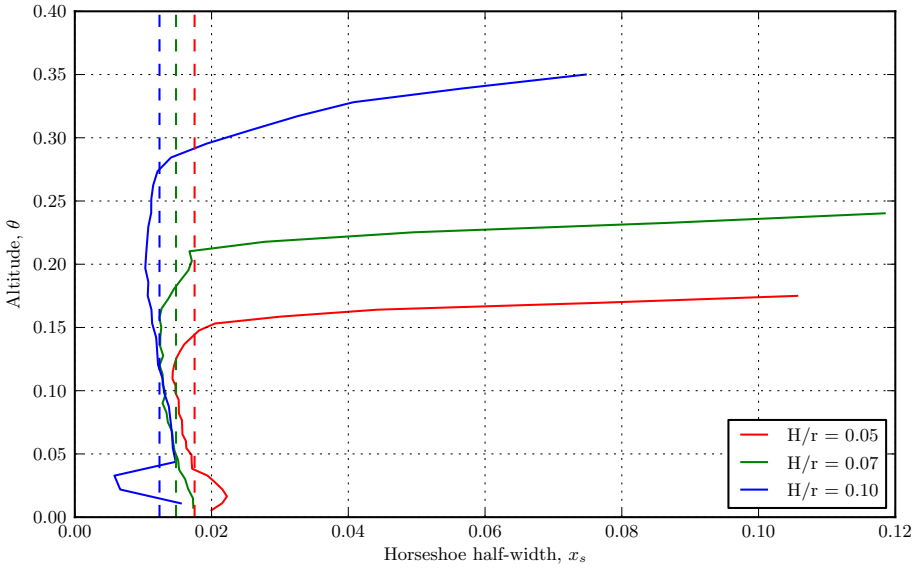

Figure 4.8: Here we show the horseshoe half-width, derived from the maximum extent of the last librating streamlines, against height in the disc measured by the altitudinal coordinate, θ, from the midplane in radians.

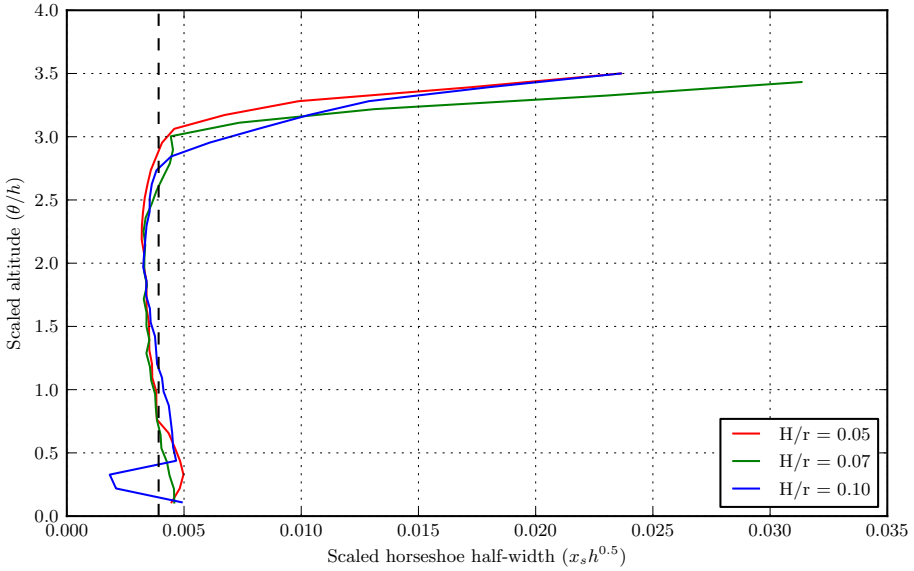

Figure 4.9: Here we show the horseshoe half-width, derived from the maximum extent of the last librating streamlines, against height in the disc measured by the altitudinal coordinate, θ, from the midplane in radians. In this figure, the quantities have been scaled such that $x_s \rightarrow x_s h^{0.5}$ and $h \rightarrow \theta/h$. In this coordinate system, we can see that the horseshoe width profile as a function of height is very similar for all three disc scale heights.

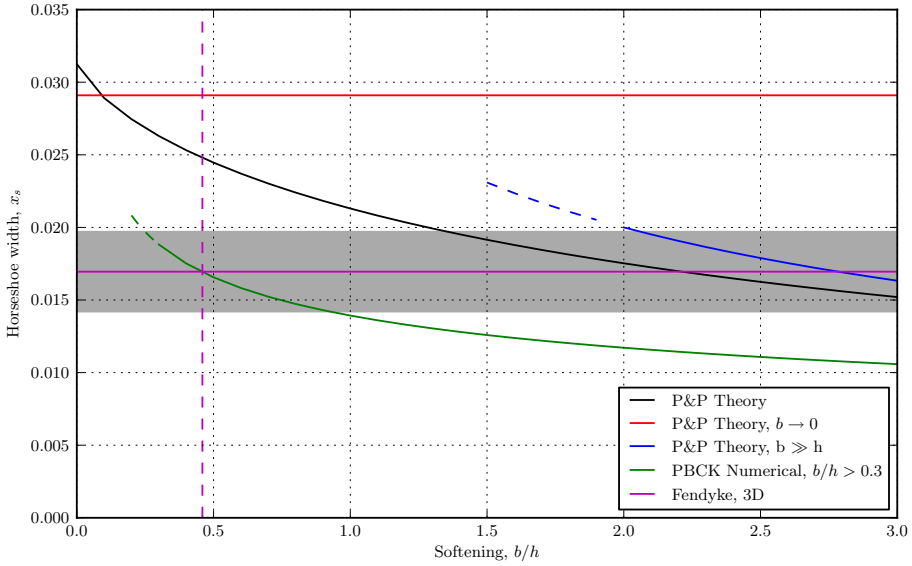

Figure 4.10: In this figure, different prescriptions for the horseshoe width from the literature are compared to our 3D values. We show **(1, black line)** the theoretical expression for the horseshoe width given by Paardekooper and Papaloizou (2009b), shown in the thesis as equation 1.20. This does not account for the disc being adiabatic or for back pressure, and so gives a wider value than we find in numerical simulation; **(2, red line)** the limit of zero softening ($b \to 0$), in which equation 1.20 tends towards the expression given in equation 1.21; **(3, blue line)** the limit ($b \gg h$), in which equation 1.20 tends towards the expression given in equation 1.22; **(4, green line)** the value from Paardekooper et al. (2010) empirically obtained from numerical simulations which they assert holds for $b/h > 0.3$; and **(5, purple line)** our 3D results, shown earlier. We combine the results for all disc thicknesses as figure 4.9 indicates that horseshoe widths for different disc scale heights can be compared when correctly scaled. The plotted value is the mean scaled horseshoe width below 3 scale heights, scaled by $0.05^{-0.5}$ to give the expected value for a $H/r = 0.05$ disc, with error bars representing the standard deviation about this mean. We obtain $x_s = 0.0170 \pm 0.0028$. Curve (4) and value (5) intersect for a $b/h = 0.459204$; a value comparable to the canonical value of 0.4 used for 2D simulations in chapter 3.

4.8 Horseshoe width with height, eccentric orbit

We can perform a similar analysis of horseshoe width as a function of altitude for increasing planetary eccentricity. We show this in figures 4.11 and 4.12 for the $H/r = 0.05$ disc. We find that the most significant effect on the horseshoe width occurs near the midplane– the plane in which the epicyclic motion takes place in– where we see a decrease in horseshoe width of some tens of percent. Further away from the midplane, we note much less of an effect. When we consider that more mass in the disc is located near the midplane, we suggest that this decrease in midplane horseshoe width is primarily responsible for the decrease of the corotation torque.

In 4.13, we show the same plot for the thicker disc where $H/r = 0.10$. We see that at higher eccentricities the corotation region shrinks dramatically around the midplane, with the height of this decrease extending to $\theta = 0.15$ $(1.5H)$ from the midplane for $e = 0.12$. This appears to be an effect of the stagnation point of the horseshoe streamlines being offset from the planet's radial location. Paardekooper and Papaloizou (2009b) find that this offset goes as $\sim br_p$ in their two dimensional simulations. Given our dependence of two dimensional softening on disc scale height, we expect the offset to be increased in a thicker disc, as we see here. This is confirmed by figure 4.14 in which the streamlines are shown.

We note that the height of the corotation region appears unchanged for increased eccentricity.

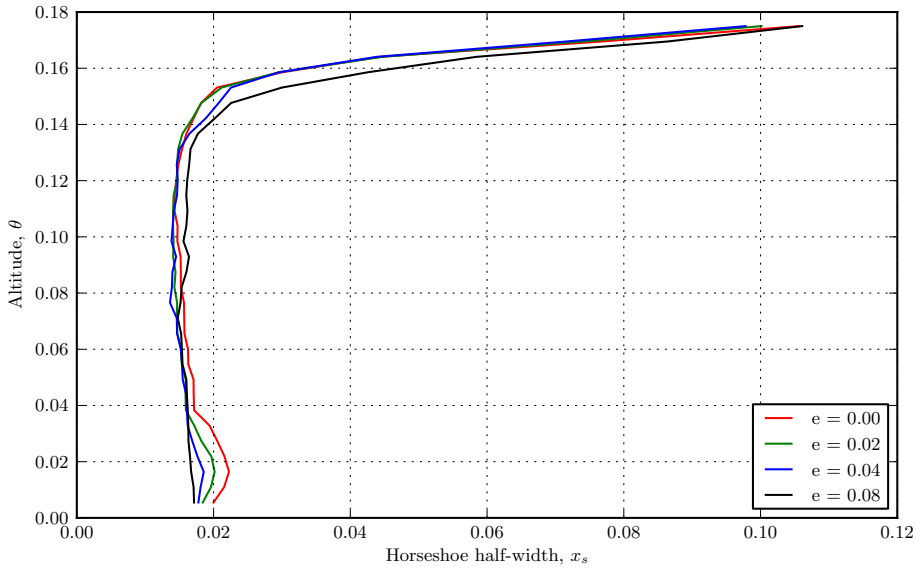

Figure 4.11: This figure shows the horseshoe width, x_s, as a function of altitude, θ, for a disc of scale height $H/r = 0.05$ and for a range of eccentricities.

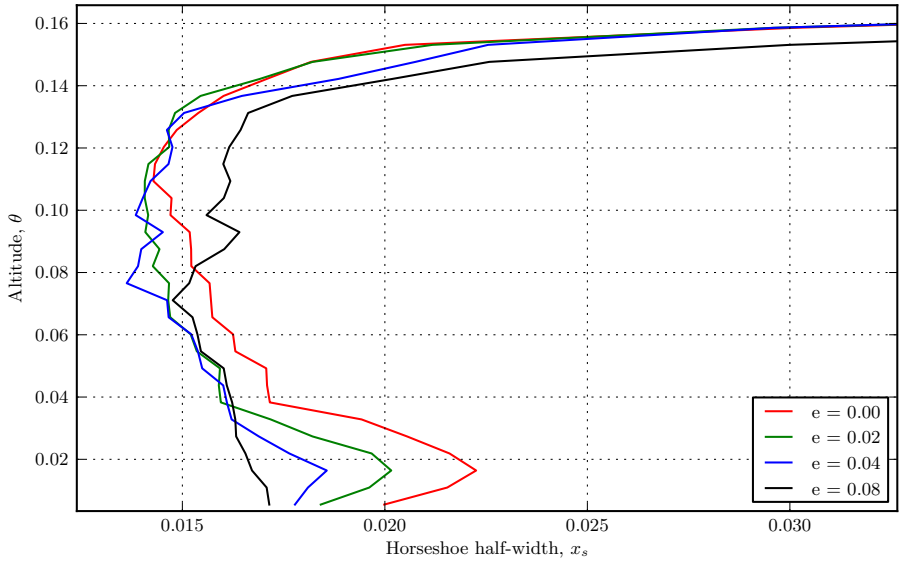

Figure 4.12: A zoomed-in version of figure 4.11 above.

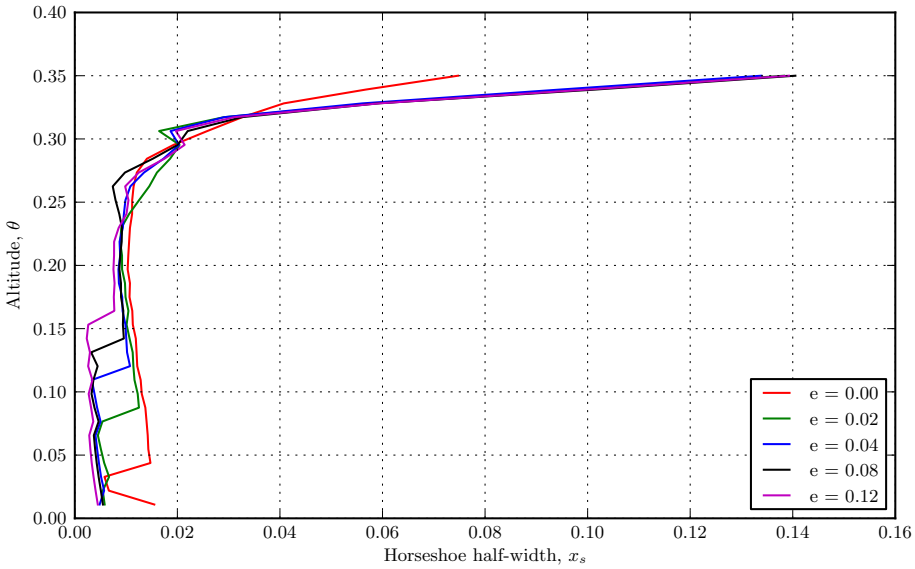

Figure 4.13: This figure shows the horseshoe width, x_s, as a function of altitude, θ, for a disc of scale height $H/r = 0.1$ and for a range of eccentricities.

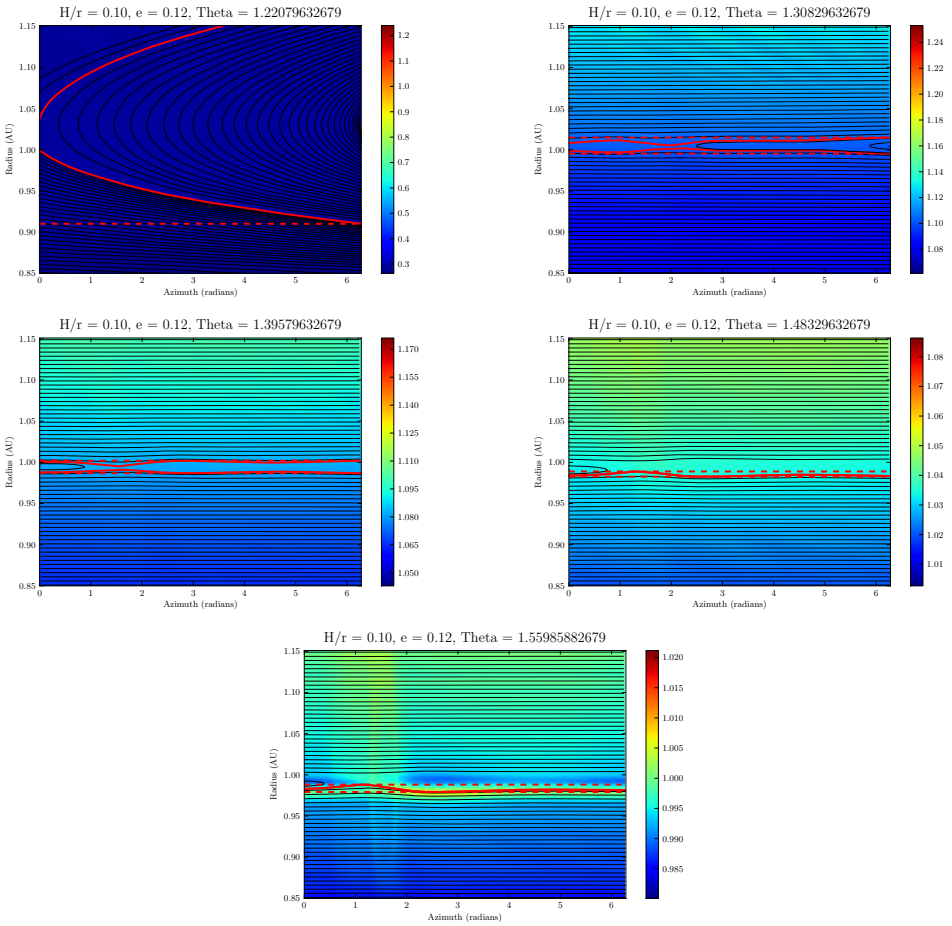

Figure 4.14: Vertical slices through a $H/r = 0.10$ disc. As the resolution in θ is 32 cells, we show here the 1st, 9th, 17th, 25th and 32nd cell slices. The maximum extent of the horseshoe region on each side is marked with a dotted line. Note that for the very outer disc, the notion of the horseshoe width is nominal, as horseshoe streamlines are not truly set up and the flow structure is complex. The quantity plotted is the perturbation to the initial density and in this case the planet is on an orbit of eccentricity, $e = 0.12$.

4.9 Discussion

In this section, we briefly review our simulation results, presented in the previous sections, and discuss the key points, highlighting some of the implications of this research.

4.9.1 Corotation torque in three dimensions

In discs with scale height $H/r = 0.05$ we observe good agreement between the two and three dimensional simulations. The magnitude of the measured torque is slightly greater in the two dimensional case (itself slightly underestimating the value we would expect from the model of Paardekooper et al. (2010)), but the attenuation appears to follow the same law. At low values of eccentricity, our model slightly underestimates the torque and at high values, our model slightly overestimates it; this is similar to a number of cases in the two dimensional regime and the discrepancy is rarely more than the error bars of the measurement.

In thicker discs with scale heights $H/r = 0.07$ and 0.1, we find that in the three dimensional case, we measure a greater corotation torque magnitude than either that of Paardekooper et al. (2010) or of our own work in two dimensions, with the scaled corotation torque reaching 14–15 in the case of $H/r = 0.1$ disc and 13 for the disc with $H/r = 0.07$, compared to 10.5 for the $H/r = 0.05$ disc. This suggests that agreement between simulations in two and three dimenions gets worse for thicker discs. We note, however, that in the case with the thicker disc, the horseshoe width is narrower and not resolved by as many cells as for the thinner disc. Combined with the fact that we do not reach convergence in our resolution study, we are cautious about making any observations about the expected magnitude of the corotation torque in a three dimensional disc and suggest the problem deserves further study.

For the $H/r = 0.1$ disc, we find that the attenuation of the torque with eccentricity fits our model and we feel confident, therefore, that the model of corotation torque attentuation that we proposed in the previous chapter is consistent with our results in 3D.

4.9.2 Vertical structure

As discussed in the previous section (4.8), we find that the horseshoe width stays roughly constant as a function of altitude below around three scale heights. This implies that the material of the corotation region librates as a column and so that material at a range of disc altitudes contribute to the overall corotation torque. We discuss the existence of a well-defined 'ceiling' to the corotation region at around three scale heights in section 4.9.3.

As the disc density profile away from the midplane decays following a Gaussian distribution, we expect that 68.2% of disc material will lie below one scale height, 95.4% will lie below two scale heights, and 99.7% will lie below three scale heights. This implies that density features in the disc beyond this limit of three scale heights are not likely to affect the corotation torque as so little mass is above that limit.

If, however, the height of the corotation region is dependent on the disc parameters, as we discuss in section 4.9.3, then we might expect this to be an issue that should be considered in discs with a dead zone. For such discs, the viscosity– and therefore the capacity of the disc to unsaturate the corotation torque– depends on altitude; the resultant corotation torque should therefore depend on the mass of material librating on horseshoe trajectories which has a viscosity capable of unsaturating the corotation torque.

In the case when the embedded planet is on an eccentric orbit, we see a narrowing of the corotation region, as in two dimensions, which is most predominant around the midplane, in which the epicyclic motion occurs. Due to the greater mass around the midplane, this is consistent with the decrease in the corotation torque.

4.9.3 Surface layers

As we note in the previous section, material in the corotation region below around three scale heights appears to librate on well-defined horseshoe trajectories with respect to the planet's location. The width and morphology of these horseshoe trajectories does not change significantly with altitude. Above three scale heights, the horseshoe streamlines begin to take on an asymmetric shape, causing an increase in horseshoe width with increasing altitude, as seen

for example in figure 4.4. In the case of our simulations, we expect the amount of disc material above $3H$ to be small, and the torque from these asymmetric exchanges to make a negligible contribution to the corotation region.

In this section, we explore whether this phenomenon can necessarily be neglected for all discs. As the point at which horseshoe streamline symmetry occurs appears to be independent of both planetary eccentricity and disc scale height, we tentatively suggest that it is a result of vertical shear in the disc.

From equation 1.9, we can write an expression for the difference in the angular velocity between disc material in the midplane and at some height z. If we assume a thin disc ($z \approx \theta_{\rm mid}$, where $\theta_{\rm mid}$ is altitude measured from the midplane) then we can let $R = 1$ and, at three scale heights, let $\theta_{\rm mid} \approx z = 3H$;

$$\Delta\Omega_{\rm shear} = [\Omega(R = 1, z = 0) - \Omega(R = 1, z = 3H)], \tag{4.5}$$

where Ω_k is the Keplerian angular velocity at $R = 1$.

We can compare this to the offset in angular velocity (from its Keplerian value) of material librating at the edge of the corotation region, a distance x_s from the planet (if we neglect the offset between the stagnation point of the horseshoe streamlines and the planet's location),

$$\Delta\Omega_{\rm lib} = \frac{3}{2}\frac{\Omega_k}{R}x_s. \tag{4.6}$$

As the contribution to angular velocity due to vertical shear increases, we would expect the corotation region ahead of the planet to narrow, as more material is now moving too rapidly with respect to the planet to undergo a horseshoe U-turn. As material behind the planet in its orbit is now approaching the planet at a decreased velocity, however, we expect the horseshoe region to widen, as more material is able to exchange sufficient angular momentum with the planet. In the case where $\Delta\Omega_{\rm shear} = \Delta\Omega_{\rm lib}$, material at a distance x_s from the planet no longer has sufficient angular velocity to be deflected by the planet and so will no longer librate on a horseshoe trajectory.

Here, we find that at three scale heights, for all disc thicknesses, the ratio of the change in angular momentum due to vertical shear and due to horseshoe libration is $\sim 43\%$. If our tentative suggestion has merit and the height at which the horseshoe region becomes asymmetric is indeed determined by the height at which the shear velocity becomes comparable to the horseshoe libration velocity, then we might expect that for discs with different density and temperature profiles (p and q in equation 1.9), we find a different 'height' to the corotation region.

This is particularly relevant given work by, for example, Pierens and Nelson (2010) which found that migration can be slowed by $\sim 40\%$ in a disc with a dead zone which extends to $2.3H$; if all of the corotation region is contained in the dead zone, the corotation torque will be nowhere unsaturated and it will attenuate after some number of orbital periods. If, however, the corotation region extends beyond the dead zone, the corotation torque will saturate for disc layers in the midplane but will be unsaturated at a greater altitude in the disc, giving a sustained overall corotation torque.

4.9.4 Comparing two and three dimensions

The final important result to come out of this investigation is our insight into the correct value of softening parameter for two dimensional simulations.

The canonical value of the softening parameter b/h has been taken to be 0.4, such that linear torques in two dimensional isothermal discs match those in three dimensional isothermal simulations by Tanaka et al. (2002). It has been an open question as to whether this value is appropriate for reproducing the non-linear horseshoe drag of a three dimensional disc with vortensity and entropy gradients. To run the suite of simulations required to answer this question would be a prohibitively expensive task at present, and no answer has yet been suggested in the literature.

In this work, we have made some progress on the issue by noting that for a disc with scale height $H/r = 0.05$, the magnitude and behaviour of the corotation torque in three dimensions are comparable to those in two dimensions with a softening parameter of $b/h = 0.4$. While in a thicker disc with $H/r = 0.07$ and 0.1, the torque magnitude appears greater in three dimensions, the attenuation of the corotation torque with eccentricity fits the law we derived in chapter 3.

Further, if we measure the width of the corotation region in units where the scaling with the scale height of the disc has been removed, we find that we get the same horseshoe width as the formula of Paardekooper et al. (2010) would yield for a two dimensional disc with $b/h = 0.46$; this value is close to the canonical choice of $b/h = 0.4$. This is by no means a definitive solution to this open question, but the evidence so far suggests that such a value of softening parameter is indeed the appropriate choice.

Summary

- We find that the relationship between corotation torque and eccentricity derived empirically in the previous chapter fits well for 3D disc models of $H/r = 0.05$ and 0.10.
- We measured the average width of the corotation region below $3H$ and found it to be comparable to the prescription of Paardekooper et al. (2010) when a softening length of $b/h = 0.4$–0.5 is used. This is consistent with the canonical $b/h = 0.4$ used in two dimensional disc simulations.
- We find that the corotation region appears to have a constant width from the midplane to a height of approximately $3H$ for all eccentricities and for all disc scale heights. Above this, the morphology of the horseshoe region becomes asymmetric; we suggest that vertical shear is responsible for this.
- We find that the horseshoe width narrows most significantly in the midplane in the case of eccentric embedded planets, giving rise to the observed decrease in corotation torque as orbital eccentricity increases.

Chapter 5

Gap Formation in Radiative Discs

In this chapter, the final project of my PhD is presented; a series of three dimensional simulations of fully radiative discs with embedded protoplanets.

In section 5.1, we describe the aims of this project; in section 5.2, we review some of the relevant background; in section 5.3 we introduce the radiation model we use for this work and our validation of the PLUTO code; in section 5.4 we describe our first model; in section 5.5 we describe our low resolution test simulations; in section 5.6 we describe our work at high resolution; finally in section 5.7 we discuss our results in context.

Please note that the work presented in this chapter was conducted in collaboration with Dr Mario Flock, who kindly provided the radiative module for the PLUTO code. The simulations described were run and analysed by the author.

5.1 The Aim

The aim of this project is to simulate fully radiative three dimensional discs with embedded protoplanets evolving under the influence of stellar irradiation. We are interested in low-mass planets, close to their parent stars where stellar irradiation is likely to be important during the formation process and we ulti-

mately seek to determine the gap opening criterion for such planets in such a region of the disc.

We tackle the problem of developing techniques to address this question in a number of stages; first, we verify that the PLUTO code we are using gives results consistent with the NIRVANA code used in chapters 3 and 4. We then consider gap opening of more massive planets further out in the disc, as a test case. We set up a series of low-resolution tests that we can conduct relatively cheaply in terms of computation time. Finally, we attempt high-resolution, long-duration simulations of massive planets further out in the disc as a prelude to considering gap-opening close to the star.

In the event, the full scope of this work proved too ambitious for the time available and we were unable to complete high-resolution simulations of massive planets in the outer disc. However, this chapter is offered as a proof-of-concept based on the work conducted so far, in the expectation that it will serve as a roadmap for future investigations.

5.2 Background

It is instructive to review some of the relevant observations of extrasolar planets that motivate this investigation.

A number of planetary systems have been detected containing super-Earth mass planets orbiting very close to their parent stars. Examples include the $4.2M_{\oplus}$ planet orbiting the 0.7 Solar mass star *HD 156668* at 0.05AU (Howard et al., 2011); the four planets in the *Kepler-224* system of 1.4, 3.1, 2.3 and 2.0 Earth radii inside 0.2AU around a star of mass 0.82 Solar masses; and the five planets of the *Kepler-186* system inside 0.36 AU of 1.1, 1.1, 1.4, 1.3 and 1.1 Earth radii (Rowe et al., 2014). The various exoplanet catalogues described in chapter 1 contain many more.

The thickness of a protoplanetary disc is determined by the requirement for vertical hydrostatic equilibrium, as described in section 1.2.5. We expect the disc scale height to be least closest to the central star and to increase as some function of radius. This is supported by 2D simulations (D'Angelo and Marzari, 2012).

We recall from chapter 3 that even low mass planets can undergo non-linear interactions in regions of the disc that are sufficiently thin. In this case, the thickness of the disc and its response to the planet will determine the migration regime of embedded planets. A planet which opens a gap, for instance, will undergo type II migration on the viscous timescale of the disc. In a region of the disc where scale height, $H/r = 0.01$, for example, the gap opening criterion in an inviscid disc (equation 1.25) is $q > 3(H/r)^3 = 3 \times 10^{-6} = 1\mathrm{M}_{\oplus}$.

To date, no numerical modelling has addressed the question of the behaviour of embedded planets in such regions of protoplanetary discs with stellar irradiation.

5.3 The Radiation Model

In this section, we briefly describe the radiation model used for this work. We use the PLUTO code for these simulations, with the radiation transfer module written for that code by Flock et al. (2013), based on the two-temperature flux-limited diffusion (FLD) model of Commerçon et al. (2011) and the hydrid flux limited diffusion approach of Kuiper et al. (2010).

In addition to the hydrodynamic equations 2.3 and the ideal gas law, the two relevant equations for radiation transport under this scheme are

$$\frac{\partial \rho e}{\partial t} = -\kappa_P(T)\rho c(a_R T^4 - E_R) - \nabla \cdot F_*, \tag{5.1}$$

$$\frac{\partial E_R}{\partial t} - \nabla \frac{c\lambda}{\kappa_R(T)\rho} \nabla E_R = \kappa_P(T)\rho c(a_R T^4 - E_R), \tag{5.2}$$

where ρ is density, κ_P and κ_R are the Planck and Rosseland mean opacities, $a_R = 4\sigma/c$ is the radiation constant, σ is the Stefan-Boltzmann constant, c is the speed of light, e is the thermal energy per unit mass, E_R is the radiation energy density and F_* is the stellar radiation flux. We use the adiabatic exponent $\gamma = 1.42$, and assume a mixture of hydrogen and helium such that the mean molecular weight is 2.35.

The irradiation flux from the central star which appears as a source term in equation 5.1 is given by

$$F_*(r) = \int_\Omega \int_\nu B_\nu(\nu, T_*) \left(\frac{R_*}{r}\right)^2 \exp[-\tau(\nu, r)]\, \mathrm{d}\nu \mathrm{d}\Omega, \tag{5.3}$$

where B_ν is the Planck function, Ω is here the solid angle, T_* and R_* are the surface temperature and radius of the star, ν is frequency and the radial optical depth for the irradiation flux is given by

$$\tau(\nu, r) = \int_{R_*}^{r} \kappa(\nu)\rho\, \mathrm{d}r. \tag{5.4}$$

The opacity values are taken from the tables of Draine and Lee (1984).

In this scheme, these equations are solved using the implicit scheme described by Flock et al. (2013), and validated by tested against the Monte Carlo radiative transfer code RADMC-3D. Briefly, the radiation transfer equations are rewritten in the form of a matrix equation $\mathbf{A}\vec{x} = \mathbf{B}$, and solved by iteration for the internal energy density of the system.

This method performs well compared to the alternative paradigm of using a Monte Carlo radiative transfer method, such as that employed by the RADMC-3D code, in which individual 'packets' of radiation are propagated through the grid in a probabilistic fashion.

5.3.1 The PLUTO code

We select the PLUTO hydrodynamic code for this task, as it is a mature, maintained code suitable for a variety of hydrodynamic and magnetohydrodynamic problems in different geometries and numbers of dimensions and capable of implementing full tensor viscosity, the FARGO algorithm and for which the radiation module described above is under active development.

Before considering a radiative disc, we first test the code against NIRVANA by setting up a suite of simulations of the kind described in chapter 3. We simulate a $5\mathrm{M}_\oplus$ planet on a fixed circular orbit in a two dimensional protoplanetary disc with scale height $H/r = 0.05$. Shown in figure 5.1 as an illustration are torque time-series for comparison from the PLUTO code run at low ($256 \times$

512) resolution and then both PLUTO and NIRVANA at the higher resolution of (1024×2048). We use wave-killed regions at the inner and outer radial boundaries, with reflecting boundary conditions. The full 2π of the disc in azimuth is simulated and a softening parameter of $b/h = 0.4$ is used.

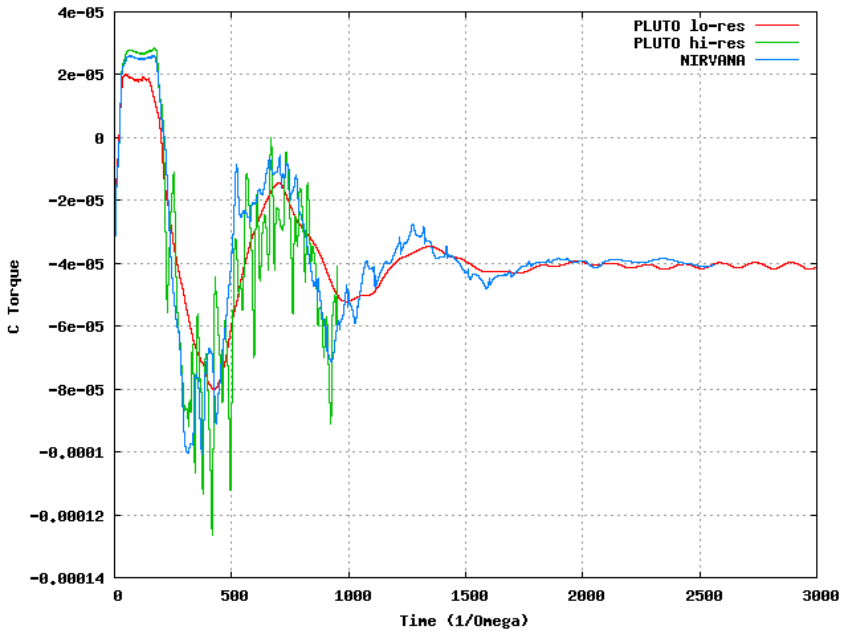

Figure 5.1: The torque time-series for a $5M_\oplus$ planet on a fixed circular orbit in a two dimensional protoplanetary disc with scale height $H/r = 0.05$. The lines shown are the data from the NIRVANA simulation used in chapter 3, from the PLUTO code at low (256×512) resolution and from the PLUTO code at the same resolution as the NIRVANA code.

In all our test simulations, as in figure 5.1, we find good agreement between our previous NIRVANA work and the PLUTO code for both torque time-series and disc density structure.

5.4 The First Model

We now begin to set up the PLUTO code to tackle the particular problem in which we are interested. As a first step, we consider gap-opening by more massive planets in outer regions of the disc, taking a $1M_J$ planet at 5AU as our standard.

We use spherical polar coordinates, which is required by the radiation module for the obvious geometrical advantages that it yields for the treament of

spherically symmetrical stellar radiation. The size of our radial cells are set to depend on a logarithmic scale, such that the cells are smallest closest the central star and largest in the outer disc. Our inner radial boundary is at 1.25 AU and our outer radial boundary is at 20 AU. We obtain our initial conditions as described in subsection 5.4.1. We simulate the full 2π of the disc in azimuth, and measure the altitude from the vertical axis such that the upper disc boundary is at 1.33 radians and the lower is at 1.81 radians, where the midplane corresponds to $\theta = \frac{\pi}{2}$.

We use a zero-gradient boundary condition at the inner and outer radial boundaries, with an outflow condition such that material can leave the computational domain but not enter. Inside 2 AU and outside 13 AU, we damp the r-component of velocity using the method of de Val-Borro et al. (2006) such that it vanishes at the grid edge. At the vertical boundary, after Gressel et al. (2013), we solve for hydrostatic balance in the boundary. We obtain the balance using first-order finite-differencing.

For the radiation transport step, we set the boundary conditions such that $T = 50$K at the upper, lower and outer radial boundaries and 200K at the inner radial boundary. We select this by requiring a value that matches the expected behaviour of the disc beyond the computation grid due to stellar irradiation. Our star has a radius of 1 solar radius and a surface temperature of 5800K and we use a dust to gas ratio of 10^{-3} in these tests.

We first consider a planetary mass of $1M_J$ at 5AU and use an α-viscosity with a viscosity of 2×10^{-3}.

5.4.1 Initial conditions

We set up an initial disc with a midplane density power law of -0.5 and a pressure consistent with a constant disc scale height $H/r = 0.05$. We first integrate this disc in two dimensions ($r \times \theta$), noting that without an embedded planet we can adopt azimuthal symmetry for the state of our disc. In this simulation, we prohibit hydrodynamic evolution but allow energy to propagate according to our radiation transport algorithm. We evolve this disc until it has reached thermal equilibrium and use it as the initial condition for a hydrodynamic and radiative disc simulation with an embedded planet.

Such a disc is shown in figures 5.3 and 5.4 and the azimuthal slice of the density field can be compared to that shown in 5.5 for an isothermal simulation where the effect of stellar irradiation on the inner disc and the surface layers is readily apparent.

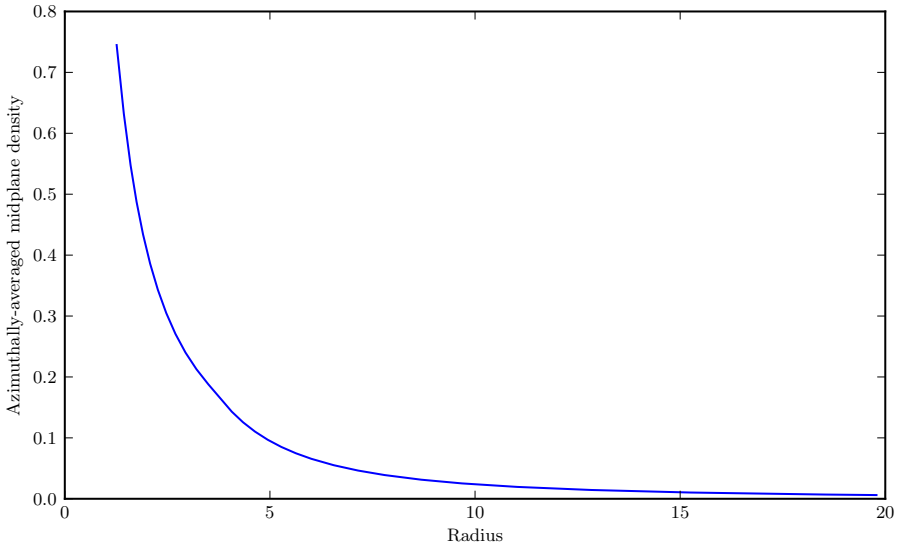

Figure 5.2: The initial (unperturbed) midplane density profile.

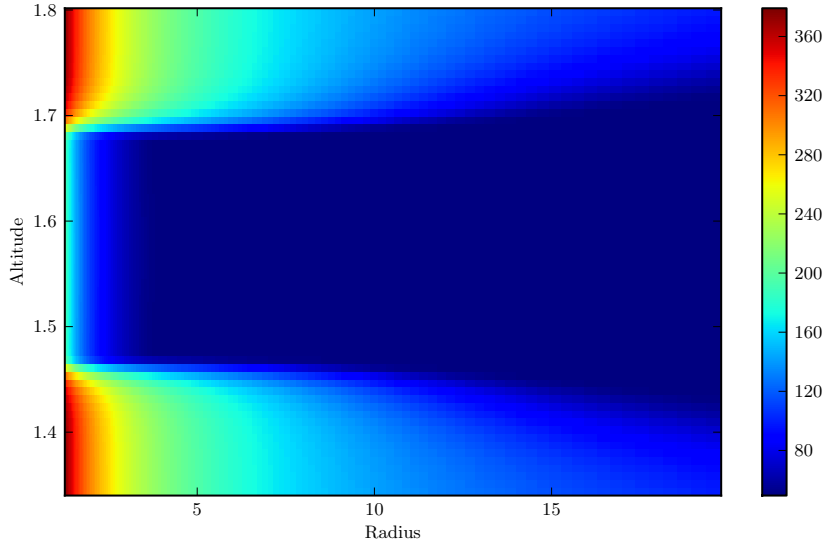

Figure 5.3: A meridional slice of the initial (unperturbed) radiative disc temperature distribution, plotted in K. Note the cool shielded interior of the disc and the warmer surface layers.

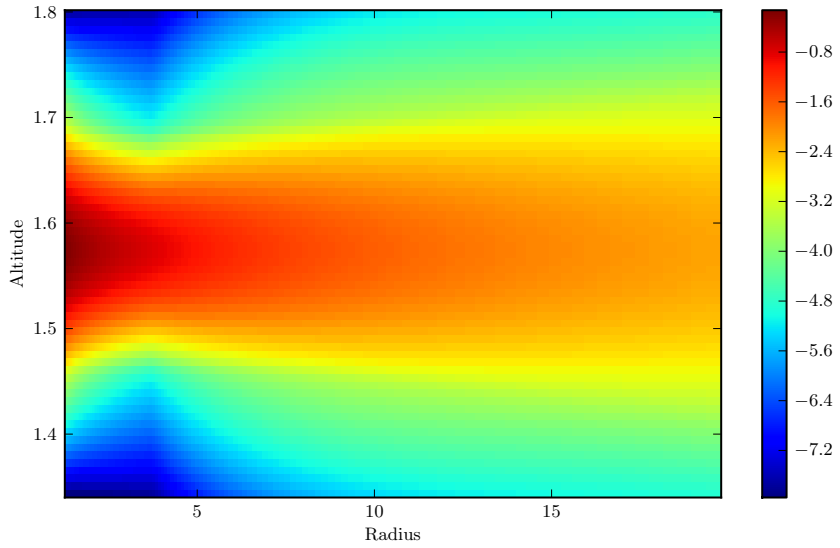

Figure 5.4: A meridional slice of the initial (unperturbed) radiative disc density distribution, plotted on a logarithmic colour scale of base 10. Note the different thickness of the disc compared to the isothermal case shown in figure 5.5.

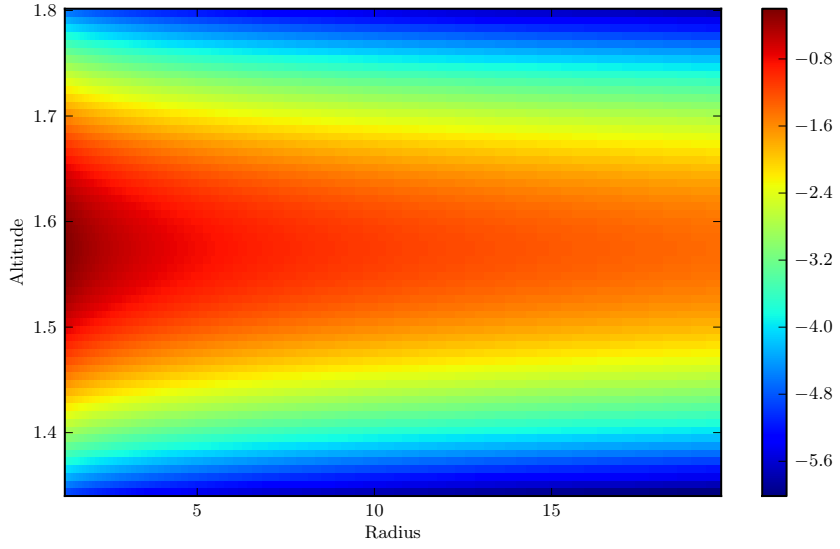

Figure 5.5: An meridional slice of the initial (unperturbed) isothermal disc density distribution, plotted on a logarithmic colour scale of base 10, for an isothermal disc.

5.5 Low-Resolution Simulations

We test this model at a resolution of $128 \times 64 \times 256$ ($N_r \times N_\theta \times N_\phi$). We note that the Hill radius of a $1M_J$ planet at 5AU is 0.35AU and that at our resolution, a single cell in radius at the planet's location (remembering that we use a logarithmic scale for radial cell sizes) is around 0.1AU. Therefore, while we do not expect results at this resolution to fully capture all the relevant physics, it allows us to develop and test the software with simulations that can be performed in an acceptable time.

We give our planet an initial mass of 20 $M_\oplus$. As material is only accreted from cells within a Hill radius of the planet, as described below, we increase the initial mass artificially in the case that no material is accreted due to the low-resolution of the simulation. Our planet is allowed to grow by accretion up to a maximum mass of $1M_J$. After this, material is still removed from the grid and the accretion rate is recorded, but the planet mass does not increase.

We also run a locally isothermal simulation for comparison, with no radiation transport step. In this simulation, we grow the planet in the same way by accretion. We note that these simulations run for hundreds of years at this resolution, for a range of viscosities. Here, we present some simulation data for a planet of mass $1M_J$ at 5AU and with viscosity parameter $\alpha = 2 \times 10^{-3}$.

5.5.1 Accretion algorithm

Our accretion algorithm follows the approach of Kley (1999).

We first set an 'accretion fraction', f_{acc}, to be some constant multiplied by the length of the current timestep (with the the condition that it is never greater than 0.01). We determine the constant in this test case such that our gap is formed in a reasonable amount of simulation time. We find a value of 30 works well.

If a grid cell is within 0.25 Hill radii of the planet, a fraction f_{acc} of the mass in the grid cell is removed. If the planet is within between 0.25 and 0.5 Hill radii of the planet, a fraction $f_{\text{acc}}/3$ of the mass is removed instead, to represent an increased accretion rate from material close to the planet. The mass removed from the grid is then added to the planet after being multiplied by a factor

of 4; this accelerated growth of the planet by more material than we accrete from the grid is intended to ensure that the growth of the planet, as well as the gap, occurs on a computationally feasible timescale.

5.5.2 Mass accretion rate

We show in figures 5.6 and 5.7 the planet mass as a function of time and the mass accreted from disc by the planet in each time step of the simulation. While the value of the latter is subject to fluctuations due to variations in the time step, we are still able to compare the mass accretion rates in the two cases. As the mass accretion rate becomes more nearly constant at > 150 orbits, we superimpose dashed black lines of the mean mass accretion rate beyond that, to illustrate the difference in rates.

We find a significantly increased mass accretion rate, and a correspondingly decreased planetary growth time in the isothermal disc as compared to the radiative one. This is consistent with the expectation from previous work; Paardekooper and Mellema (2008) find that in simulated discs with radiation transport but no stellar irradiation, the accretion rate is limited by the ability of disc material to cool effectively and can drop by as much as an order of magnitude from the expected values from isothermal simulations.

5.5.3 Disc structure

In figure 5.8, we show the midplane density in radiative and isothermal simulations respectively and note that the gap width appears to be comparable in the two cases, though the density in the outer disc shows a different behaviour. This is more clearly seen by comparing figures 5.9 and 5.10 in which we show azimuthally-averaged density after ~ 150 orbits on the same colour scale. We note that surface 'flaring' is apparent in the radiative case compared to the isothermal one.

Figure 5.11 shows the azimuthally averaged temperature profile of the disc. We note that the temperature profile primarily appears to have altered at the disc surface and towards the upper and lower regions of the gap opened by the planet, though we note here again the low resolution being used in these simulations.

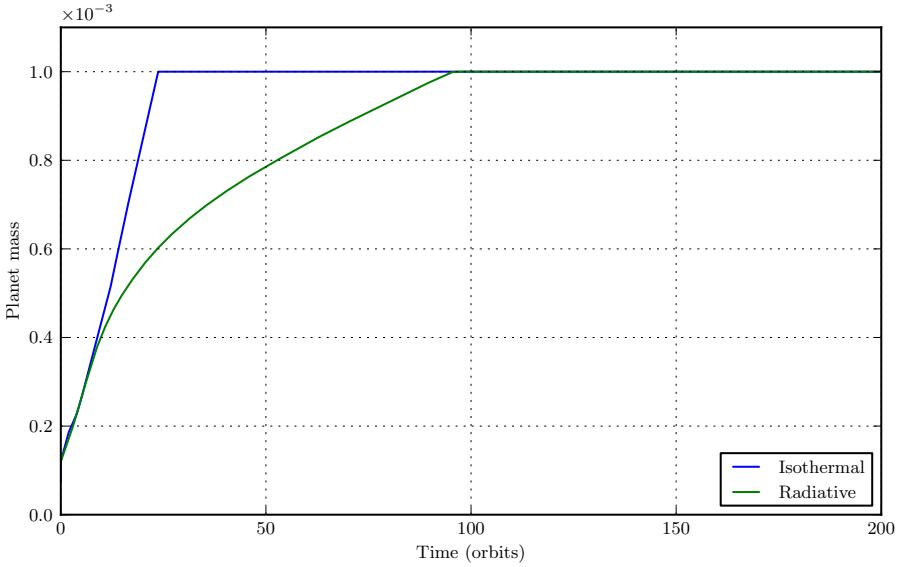

Figure 5.6: Time series of the planet mass against time. We note that the planet grows much more rapidly in the isothermal case. This is consistent with the greater accretion rate that we see in figure 5.7.

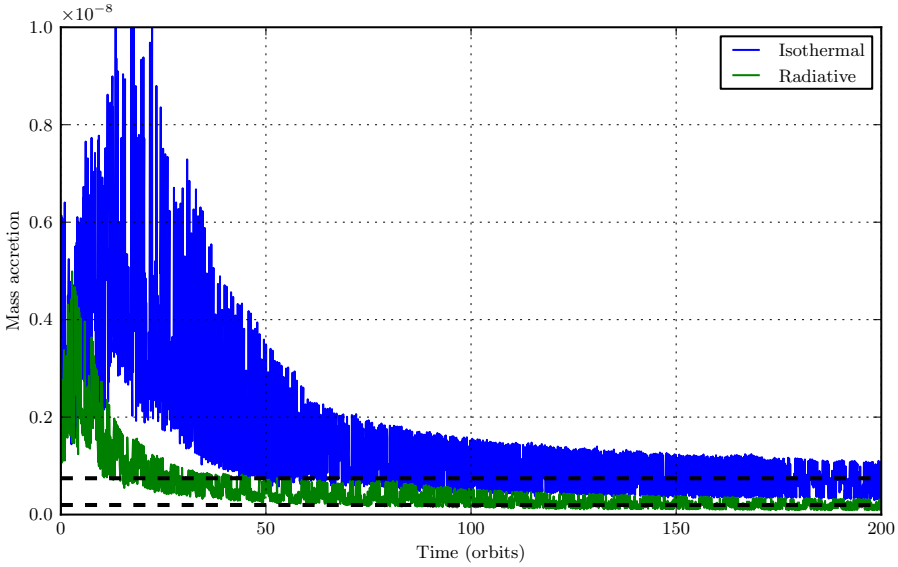

Figure 5.7: Time series of the mass accreted from the disc by the planet per timestep. As the mass accretion rate becomes more nearly constant at > 150 orbits, we superimpose dashed black lines of the mean mass accretion rate beyond that, to illustrate the difference in rates; we find accretion in the radiative disc proceeds at $\sim 26\%$ of the rate in the comparable isothermal disc.

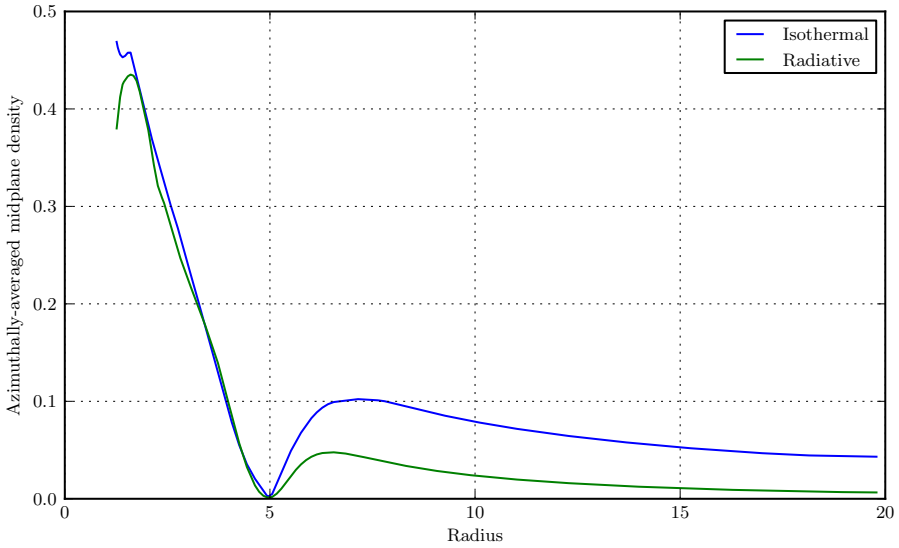

Figure 5.8: The midplane density for both our radiative and isothermal disc simulations at low resolution.

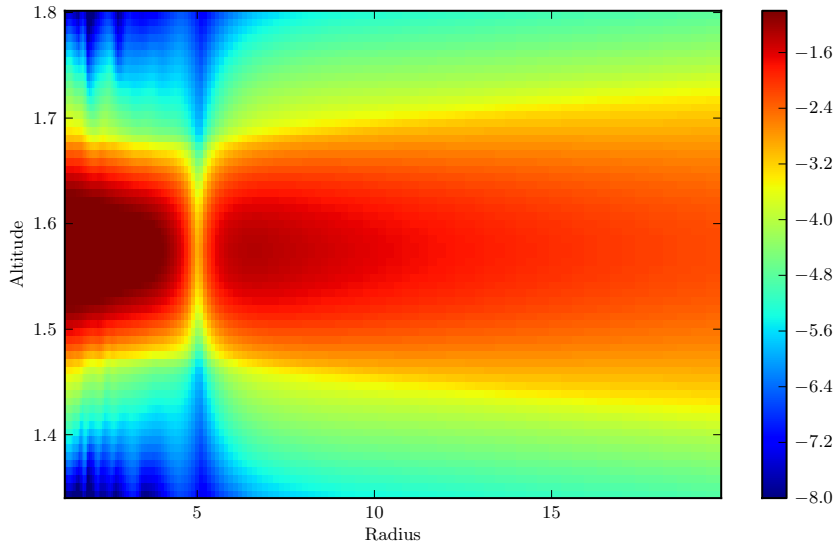

Figure 5.9: The azimuthally averaged density profile of the our low-resolution radiative disc with an embedded planet.

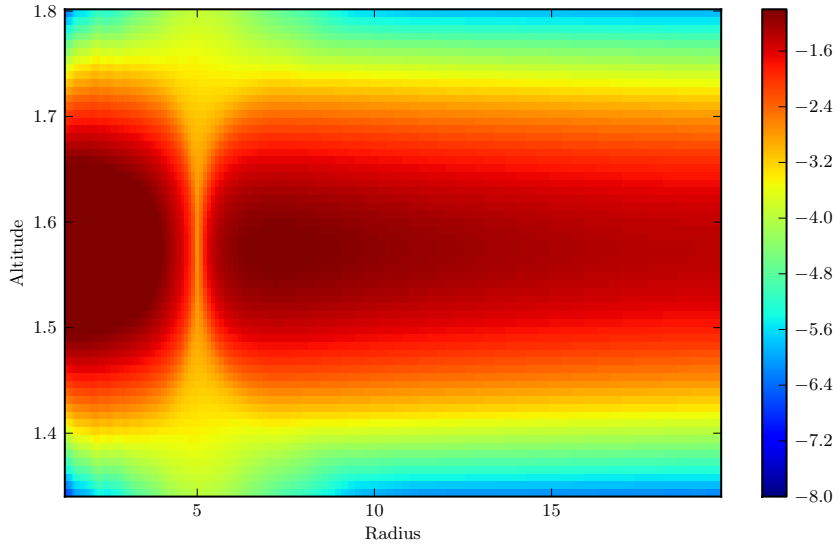

Figure 5.10: The azimuthally averaged density profile of the our low-resolution isothermal disc with an embedded planet.

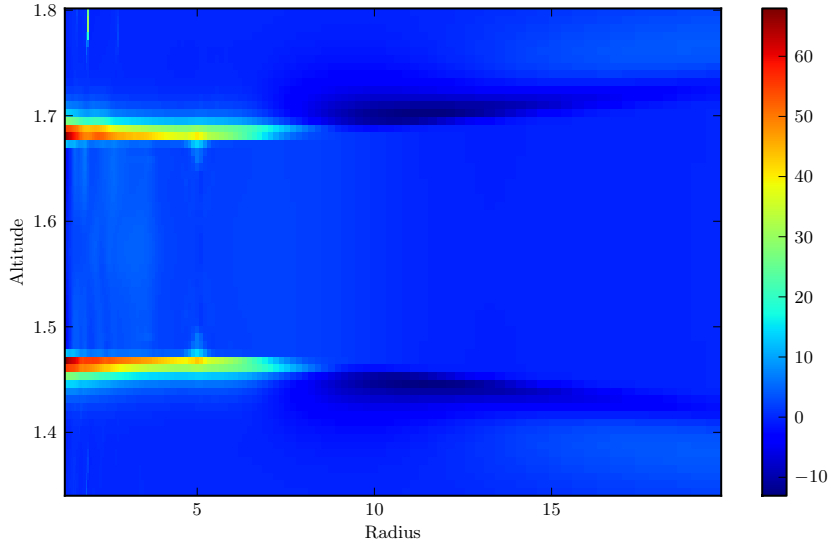

Figure 5.11: The azimuthally averaged temperature profile of the our low-resolution radiative disc with an embedded planet, shown as the difference in temperature from the unperturbed stated shown in figure 5.3.

5.6 High-Resolution Simulations

Having sucessfully simulated an embedded planet in an disc under stellar irradiation, we attempt to increase the resolution. Unfortunately, we find that the simulation is not numerically stable; producing unphysical cell properties at the boundaries, ending the simulation after only a few orbits, even without the presence of a planet. This appears to be connected to the strong density features near the upper and lower boundaries shown in figure 5.12.

It appears that more work needs to be done to allow the disc to maintain a stationary equilibrium and this will require improvements to the vertical boundary conditions. We suggest that further study is needed to ascertain what form of boundary condition will allow us to tackle this problem at high resolutions. Once this question has been addressed, the next step in this project is to consider the inner regions of the protoplanetary disc where stellar irradiation has a greater effect on the structure of the disc.

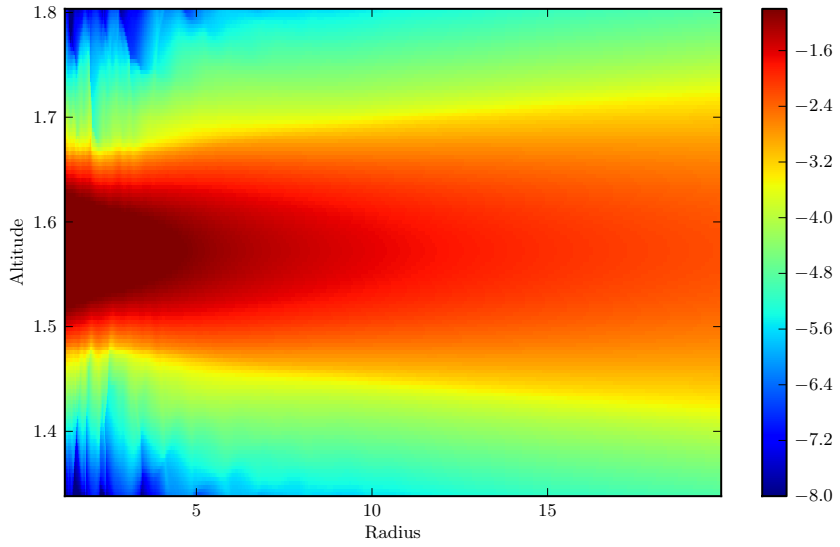

Figure 5.12: The density profile of the our low-resolution radiative disc with an embedded planet.

5.7 Discussion

In this section, we comment briefly on the work presented in this chapter, which we remind the reader should not be taken as a complete project with solid results, but rather as a proof of concept and as evidence of the development work conducted so far.

We find that at low-resolution, we can simulate a disc with stellar irradiation and an embedded protoplanet. We find that the accretion rate is significantly lower in the radiative disc than the isothermal disc, consistent with previous work, as the acreting gas needs to cool before it falls onto the planet.

We find this work cannot be easily extended to the higher resolutions that would be required to investigate in detail the process of gap formation and planetary accretion rates of different mass planets in different regimes of the protoplanetary disc.

We suggest that if the boundary conditions can be improved to the point where we are able to run a stable simulation, we can extend this work to the regime in which we are primarily interested. This work is in progress and will be the focus of future work.

Summary

- We have set up a low-resolution simulation of a 1 M_{J} planet embedded at 5 AU in a protoplanetary disc which evolves under the action of stellar irradiation. We get results broadly consistent with previous work.
- We find this simulation set-up cannot be easily extended to higher resolution and suggest more work on improving the boundary conditions.

Chapter 6

Concluding remarks

In this chapter, I provide a brief summary of the work presented in the previous chapters and discuss in more detail how my results fit into the body of literature in the field. I also make some suggestions regarding future research to build upon our findings.

6.1 The Big Picture: Population Synthesis

Current population synthesis models (e.g. Mordasini et al., 2009; Hellary and Nelson, 2012; Coleman and Nelson, 2014) cannot yet reproduce in a natural way the population of currently observed exoplanets including the large population of super-Earth and Neptune mass planets known to exist. Tackling this problem requires a two-fold approach; observers must continue to update the dataset of known extrasolar planetary systems to inform theorists in their work, and theorists must revise and improve their models using more detailed simulations and analyses.

As it is impossible to simulate all the relevant physics required in such a model over the Myr timescales on which planetary systems are believed to form, it is necessary for such work to make use of simplifications and heuristics, often derived from analytic work and highly-detailed simulations of physical processes over a much shorter timescale.

6.2 The Corotation Torque

In this thesis, we have presented research that materially adds to the understanding of the corotation torque experienced by a low-mass planet in a protoplanetary disc, by using two and three dimensional hydrodynamic simulations. We have demonstrated that the corotation torque can be modelled as exponentially decreasing with planetary eccentricity, with an e-folding eccentricity that goes with the disc scale height. As the corotation torque determines the existence of zero-torque radii, towards which planets migrate, an understanding of the corotation torque is crucial for a qualitative understanding of the behaviour of embedded planets. We have also presented the first stages in a project to better understand the hitherto unstudied evolution of low-mass planets in the thin, inner regions of protoplanetary discs, including the effects of stellar irradiation.

While our work has contributed significantly, we still lack a general model of the corotation torque suitable for all disc morphologies and verified by three-dimensional hydrodynamic simulations and we suggest that such a model would be valuable.

In parallel with our own research, work has continued on other aspects of the corotation torque. The formation of asymmetric cold 'fingers' which add a negative contribution to the corotation torque for planets $\lesssim 5\mathrm{M}_\oplus$ were discovered by Lega et al. (2014), for instance, in simulations of protoplanetary discs including radiative transfer; the effect is believed to be caused by disc material librating on horseshoe trajectories encountering the planet and radiatively cooling, becoming cooler and more dense. This effect has no analogue in isothermal or adiabatic models. Further investigations of this feature will require high-resolution simulations with sophisticated thermal models. In addition, Guilet et al. (2013) have explored a magnetic component to the corotation torque in the case of weakly magnitised discs due to the interaction between the horseshoe motion and the gas.

These two cases demonstrate the necessity of improving the resolution of simulations and the accuracy of the physics being simulated.

The magnitude of the corotation torque is linked to the ability of the disc to maintain the entropy and vortensity gradients across the corotation region. In practice, we expect discs to have a 'dead zone' with a magnetic field and not

suspceptible to the magneto-rotational instability believed to be the dominant contributor to disc viscosity; this implies that we might expect disc viscosity to vary as function of location in the disc. In this context, we can appreciate the impact of our brief investigation into the three dimensional structure of the corotation region; we found that for our discs, the horseshoe width remains roughly constant for around three scale heights from the midplane and that above that, the horseshoe width rapidly increases as the trajectories become asymmetric. We suggest that the velocity shear in the disc approaches the libration velocity of disc material and leave open the question of whether the height at which this occurs changes with disc parameters. Further research on this question would be desirable, as well as the development of more sophisticated models of the existence and evolution of dead zones in protoplanetary disc, such as the work by Bitsch et al. (2014) who find that viscosity transitions in radiative discs can cause density features which act as 'planet traps' for planets of a few Earth masses.

6.3 Short-period, Low-mass Planets.

Due to increased computational complexity and the associated longer time to run simulations, relatively few disc simulations have included realistic transport and even fewer have considered stellar irradiation. Such realism will be required for simulations of low-mass planets close to their parent stars, where the disc is expected to be sufficiently thin that planets of only a few Earth masses are likely to be able to significantly perturb the disc and even open gaps.

In chapter 5, we presented the initial stages of a project to explore this interesting region. We found that further development of the numerical set up, including more sophisticated boundary conditions, are likely to be required before this problem can be tackled at high resolution with sellar irradiation. Further work on this area is likely to continue.

6.4 Future Work

One area in which future work will focus is that of the process of accretion of disc material by embedded planets. Gressel et al. (2013), for instance, have performed global 3D hydrodynamic and magnetohydrodynamic simulations of accretion, including the formation and evolution of circumplanetary discs. As this research develops, it will allow a more accurate prescription for planetary accretion to be included in other work.

The PLATO spacecraft (Rauer et al., 2013), scheduled for launch by the European Space Agency between 2022 and 2024, will be positioned in orbit around the L2 Lagrangian point of the Sun and the Earth and will be in operation for at least six years, providing long-duration, high-precision, uninterrupted light curves for a large sample of bright stars (magnitude 11 and brighter).

The goal of PLATO is to locate terrestrial planets in the habitable zone of stars similar to our own, answering the question of how common Earth-like planets are. Planets detected around the bright stars in the survey are likely to be prime targets for spectrographic follow-up.

An open question remains about more extreme planetary systems. Work by Jensen and Akeson (2014) in which misaligned prootplanetary discs in a binary system were studied using data from the ALMA radio telescope array, for instance, raises the question of how planets might evolve in such a system. Theoretical studies of such binary systems include, for example, that of Martin et al. (2013) who simulated dead zones in protoplanetary discs in binary systems.

References

Andrews, S. M. and Williams, J. P. (2005). Circumstellar Dust Disks in Taurus-Auriga: The Submillimeter Perspective. *The Astrophysical Journal*, 631:1134–1160.

Armitage, P. J. (2011). Dynamics of Protoplanetary Disks. *Annual Review of Astronomy and Astrophysics*, 49(1):195–236.

Artymowicz, P. (1993). On the Wave Excitation and a Generalized Torque Formula for Lindblad Resonances Excited by External Potential. *The Astrophysical Journal*, 419:155.

Balbus, S. A. and Hawley, J. F. (1991). A powerful local shear instability in weakly magnetized disks. I - Linear analysis. II - Nonlinear evolution. *The Astrophysical Journal*, 376:214–233.

Balbus, S. A. and Papaloizou, J. C. B. (1999). On the Dynamical Foundations of α Disks. *The Astrophysical Journal*, 521:650–658.

Baruteau, C., Crida, A., Paardekooper, S.-J., Masset, F., Guilet, J., Bitsch, B., Nelson, R. P., Kley, W., and Papaloizou, J. C. (2013). *Planet-Disc Interactions and Early Evolution of Planetary Systems*. Protostars and Planets VI (website preprint).

Baruteau, C. and Masset, F. (2008). On the corotation torque in a radiatively inefficient disk. *The Astrophysical Journal*, 672(2):1054.

Bitsch, B. and Kley, W. (2010). Orbital evolution of eccentric planets in radiative discs. *Astronomy & Astrophysics*, 523.

Bitsch, B., Morbidelli, A., Lega, E., Kretke, K., and Crida, A. (2014). Stellar irradiated discs and implications on migration of embedded planets-III. Viscosity transitions. *Astronomy & Astrophysics*, 570:A75.

Borucki, W. J., Agol, E., Fressin, F., Kaltenegger, L., Rowe, J., Isaacson, H., Fischer, D., Batalha, N., Lissauer, J. J., Marcy, G. W., et al. (2013). Kepler-62: A five-planet system with planets of 1.4 and 1.6 Earth radii in the Habitable Zone. *Science*, 340(6132):587–590.

Brown, D. J. A., Cameron, A. C., Anderson, D. R., Enoch, B., Hellier, C., Maxted, P. F. L., Miller, G. R. M., Pollacco, D., Queloz, D., Simpson, E., Smalley, B., Triaud, A. H. M. J., Boisse, I., Bouchy, F., Gillon, M., and Hébrard, G. (2012). Rossiter-McLaughlin effect measurements for WASP-16, WASP-25 and WASP-31. *Monthly Notices of the Royal Astronomical Society*, 423:1503–1520.

Casertano, S., Lattanzi, M. G., Sozzetti, A., Spagna, A., Jancart, S., Morbidelli, R., Pannunzio, R., Pourbaix, D., and Queloz, D. (2008). Double-blind test program for astrometric planet detection with Gaia. *Astronomy & Astrophysics*, 482:699–729.

Chambers, J. E. (2009). Planetary Migration: What Does It Mean for Planet Formation? *Annual Review of Earth and Planetary Sciences*, 37:321–344.

Chatterjee, S., Ford, E. B., Matsumura, S., and Rasio, F. A. (2008). Dynamical Outcomes of Planet-Planet Scattering. *The Astrophysical Journal*, 686:580–602.

Clarke, C. J., Gendrin, A., and Sotomayor, M. (2001). The dispersal of circumstellar discs: the role of the ultraviolet switch. *Monthly Notices of the Royal Astronomical Society*, 328:485–491.

Coleman, G. A. and Nelson, R. P. (2014). On the formation of planetary systems via oligarchic growth in thermally evolving viscous discs. *Monthly Notices of the Royal Astronomical Society*, 445(1):479–499.

Commerçon, B., Teyssier, R., Audit, E., Hennebelle, P., and Chabrier, G. (2011). Radiation hydrodynamics with adaptive mesh refinement and application to prestellar core collapse. I. Methods. *Astronomy & Astrophysics*, 529:35.

Cossou, C., Raymond, S., and Pierens, A. (2013). Convergence zones for Type I migration: an inward shift for multiple planet systems. *Astronomy & Astrophysics*, 553:L2.

Courant, R., Friedrichs, K., and Lewy, H. (1928). Über die partiellen differenzengleichungen der mathematischen physik. *Mathematische Annalen*, 100:32–74.

Cresswell, P., Dirksen, G., Kley, W., and Nelson, R. P. (2007). On the evolution of eccentric and inclined protoplanets embedded in protoplanetary disks. *Astronomy & Astrophysics*, 473:329–342.

Cresswell, P. and Nelson, R. (2006). On the evolution of multiple protoplanets embedded in a protostellar disc. *Astronomy & Astrophysics*, 450(2):833–853.

Crida, A., Morbidelli, A., and Masset, F. (2006). On the width and shape of gaps in protoplanetary disks. *Icarus*, 181(2):587–604.

D'Angelo, G. and Marzari, F. (2012). Outward Migration of Jupiter and Saturn in Evolved Gaseous Disks. *The Astrophysical Journal*, 757:50.

Davies, M. B., Adams, F. C., Armitage, P., Chambers, J., Ford, E., Morbidelli, A., Raymond, S. N., and Veras, D. (2013). *The Long-Term Dynamical Evolution of Planetary Systems*. Protostars and Planets VI (website preprint).

de Val-Borro, M., Edgar, R., Artymowicz, P., Ciecielag, P., Cresswell, P., D'Angelo, G., Delgado-Donate, E., Dirksen, G., Fromang, S., Gawryszczak, A., et al. (2006). A comparative study of disc–planet interaction. *Monthly Notices of the Royal Astronomical Society*, 370(2):529–558.

Draine, B. T. and Lee, H. M. (1984). Optical properties of interstellar graphite and silicate grains. *The Astrophysical Journal*, 285:89–108.

Dullemond, C. and Monnier, J. (2010). The Inner Regions of Protoplanetary Disks. *Annual Review of Astronomy and Astrophysics*, 48(1):205–239.

Endl, M., Robertson, P., Cochran, W. D., MacQueen, P. J., Brugamyer, E. J., Caldwell, C., Wittenmyer, R. A., Barnes, S. I., and Gullikson, K. (2012). Revisiting ρ1 Cancri e: A New Mass Determination Of The Transiting super-Earth. *The Astrophysical Journal*, 759(1):19.

ESA (2013). Esa science and technology: Exoplanets. `http://sci.esa.int/gaia/40577-extra-solar-planets/`. Accessed: August 2014.

Fabrycky, D. C., Ford, E. B., Steffen, J. H., Rowe, J. F., Carter, J. A., Moorhead, A. V., Batalha, N. M., Borucki, W. J., Bryson, S., Buchhave, L. A.,

et al. (2012). Transit Timing Observations from Kepler. IV. Confirmation of Four Multiple-planet Systems by Simple Physical Models. *The Astrophysical Journal*, 750(2):114.

Fendyke, S. M. and Nelson, R. P. (2014). On the corotation torque for low-mass eccentric planets. *Monthly Notices of the Royal Astronomical Society*, 437:96–107.

Flock, M., Fromang, S., González, M., and Commerçon, B. (2013). Radiation magnetohydrodynamics in global simulations of protoplanetary discs. *Astronomy & Astrophysics*, 560:43.

Fogg, M. J. and Nelson, R. P. (2007). The effect of type I migration on the formation of terrestrial planets in hot-Jupiter systems. *Astronomy & Astrophysics*, 472(3):1003–1015.

Fogg, M. J. and Nelson, R. P. (2009). Terrestrial planet formation in low-eccentricity warm-Jupiter systems. *Astronomy & Astrophysics*, 498:575–589.

Ford, E. B., Ragozzine, D., Rowe, J. F., Steffen, J. H., Barclay, T., Batalha, N. M., Borucki, W. J., Bryson, S. T., Caldwell, D. A., Fabrycky, D. C., Gautier, T. N., Holman, M. J., Ibrahim, K. A., Kjeldsen, H., Kinemuchi, K., Koch, D. G., Lissauer, J. J., Still, M., Tenenbaum, P., Uddin, K., and Welsh, W. (2012). Transit Timing Observations from Kepler. V. Transit Timing Variation Candidates in the First Sixteen Months from Polynomial Models. *The Astrophysical Journal*, 756(2):185.

Fox, P. (1967). On the Partial Difference Equations of Mathematical Physics. *IBM J. Res. Develop.*, 11:215–234.

Fressin, F., Torres, G., Rowe, J. F., Charbonneau, D., Rogers, L. A., Ballard, S., Batalha, N. M., Borucki, W. J., Bryson, S. T., Buchhave, L. A., et al. (2011). Two Earth-sized planets orbiting Kepler-20. *Nature*.

Gammie, C. F. (1996). Layered Accretion in T Tauri Disks. *The Astrophysical Journal*, 457:355.

Gammie, C. F. (2001). Nonlinear Outcome of Gravitational Instability in Cooling, Gaseous Disks. *The Astrophysical Journal*, 553:174–183.

Gautier III, T. N., Charbonneau, D., Rowe, J. F., Marcy, G. W., Isaacson, H., Torres, G., Fressin, F., Rogers, L. A., Désert, J.-M., Buchhave, L. A., et al.

(2012). Kepler-20: a Sun-like star with three sub-Neptune exoplanets and two Earth-size candidates. *The Astrophysical Journal*, 749(1):15.

Goldreich, P. and Sari, R. (2003). Eccentricity Evolution for Planets in Gaseous Disks. *The Astrophysical Journal*, 585:1024–1037.

Goldreich, P. and Tremaine, S. (1979). The excitation of density waves at the lindblad and corotation resonances by an external potential. *The Astrophysical Journal*, 233:857–871.

Goldreich, P. and Tremaine, S. (1980). Disk-satellite interactions. *The Astrophysical Journal*, 241:425–441.

Gressel, O., Nelson, R. P., Turner, N. J., and Ziegler, U. (2013). Global Hydromagnetic Simulations of a Planet Embedded in a Dead Zone: Gap Opening, Gas Accretion, and Formation of a Protoplanetary Jet. *The Astrophysical Journal*, 779:59.

Gropp, W., Lusk, E., and Thakur, R. (1999). *Using MPI-2: Advanced features of the message-passing interface*. MIT press.

Guilet, J., Baruteau, C., and Papaloizou, J. C. B. (2013). Type I planet migration in weakly magnetized laminar discs. *Monthly Notices of the Royal Astronomical Society*, 430:1764–1783.

Hayashi, C. (1981). Structure of the Solar Nebula, Growth and Decay of Magnetic Fields and Effects of Magnetic and Turbulent Viscosities on the Nebula. *Progress of Theoretical Physics Supplement*, 70:35–53.

Heintz, W. D. (1988). The binary star 70 Ophiuchi revisited. *Journal of the Royal Astronomical Society of Canada*, 82:140–145.

Hellary, P. and Nelson, R. P. (2012). Global models of planetary system formation in radiatively-inefficient protoplanetary discs. *Monthly Notices of the Royal Astronomical Society*, 419:2737–2757.

Helled, R., Meru, F., Fortney, J. J., Bodenheimer, P., Mayer, L., Podolak, M., Boley, A., Nayakshin, S., Alibert, Y., and Boss, A. P. (2013). *Giant Planet Formation, Evolution, and Internal Structure*. Protostars and Planets VI (website preprint).

Hernández, J., Hartmann, L., Megeath, T., Gutermuth, R., Muzerolle, J., Calvet, N., Vivas, A. K., Briceño, C., Allen, L., Stauffer, J., Young, E., and

Fazio, G. (2007). A Spitzer Space Telescope Study of Disks in the Young σ Orionis Cluster. *The Astrophysical Journal*, 662:1067–1081.

Howard, A. W., Johnson, J. A., Marcy, G. W., Fischer, D. A., Wright, J. T., Henry, G. W., Isaacson, H., Valenti, J. A., Anderson, J., and Piskunov, N. E. (2011). The NASA-UC Eta-Earth Program. II. A Planet Orbiting HD 156668 with a Minimum Mass of Four Earth Masses. *The Astrophysical Journal*, 726:73.

Hubickyj, O. (2010). Core-accretion Model. *Formation and Evolution of Exoplanets (Ed. by Rory Barnes)*, pages 101–122.

Jackson, B., Greenberg, R., and Barnes, R. (2008). Tidal Evolution of Close-in Extrasolar Planets. *The Astrophysical Journal*, 678:1396–1406.

Jacob, W. S. (1855). On certain Anomalies presented by the Binary Star 70 Ophiuchi. *Monthly Notices of the Royal Astronomical Society*, 15:228–230.

Jensen, E. L. N. and Akeson, R. (2014). Misaligned protoplanetary disks in a young binary star system. *Nature*, 511:567–569.

Kley, W. (1999). Mass flow and accretion through gaps in accretion discs. *Monthly Notices of the Royal Astronomical Society*, 303:696–710.

Kley, W., Bitsch, B., and Klahr, H. (2009). Planet migration in three-dimensional radiative discs. *Astronomy & Astrophysics*, 506:971–987.

Kley, W., Müller, T., Kolb, S., Benítez-Llambay, P., and Masset, F. (2012). Low-mass planets in nearly inviscid disks: numerical treatment. *Astronomy & Astrophysics*, 546:A99.

Kley, W. and Nelson, R. P. (2012). Planet-Disk Interaction and Orbital Evolution. *Annual Review of Astronomy and Astrophysics*, 50(1):211–249.

Kolb, S. M., Stute, M., Kley, W., and Mignone, A. (2013). Radiation hydrodynamics integrated in the PLUTO code. *Astronomy & Astrophysics*, 559:80.

Korycansky, D. and Papaloizou, J. (1996). A method for calculations of nonlinear shear flow: Application to formation of giant planets in the solar nebula. *The Astrophysical Journal Supplement Series*, 105:181.

Korycansky, D. and Pollack, J. (1993). Numerical calculations of the linear response of a gaseous disk to a protoplanet. *Icarus*, 102(1):150–165.

Kuiper, G. P. (1951). On the Origin of the Solar System. *Proceedings of the National Academy of Science*, 37:1–14.

Kuiper, R., Klahr, H., Dullemond, C., Kley, W., and Henning, T. (2010). Fast and accurate frequency-dependent radiation transport for hydrodynamics simulations in massive star formation. *Astronomy & Astrophysics*, 511:A81.

Landau, L. D. and Lifshitz, E. (1987). *Fluid mechanics: Volume 6 (Course of Theoretical Physics)*. Butterworth-Heinemann.

Lega, E., Crida, A., Bitsch, B., and Morbidelli, A. (2014). Migration of Earth-sized planets in 3D radiative discs. *Monthly Notices of the Royal Astronomical Society*, 440:683–695.

LeVeque, R. J. (2002). *Finite volume methods for hyperbolic problems*. Cambridge University Press.

Lin, D. and Papaloizou, J. (1986a). On the tidal interaction between protoplanets and the primordial solar nebula. II-Self-consistent nonlinear interaction. *The Astrophysical Journal*, 307:395–409.

Lin, D. and Papaloizou, J. (1986b). On the tidal interaction between protoplanets and the protoplanetary disk. III- Orbital migration of protoplanets. *The Astrophysical Journal*, 309:846.

Lin, D. N. C. and Papaloizou, J. C. B. (1993). On the tidal interaction between protostellar disks and companions. In Levy, E. H. and Lunine, J. I., editors, *Protostars and Planets III*, pages 749–835.

Lissauer, J. J., Fabrycky, D. C., Ford, E. B., Borucki, W. J., Fressin, F., Marcy, G. W., Orosz, J. A., Rowe, J. F., Torres, G., Welsh, W. F., Batalha, N. M., Bryson, S. T., Buchhave, L. A., Caldwell, D. A., Carter, J. A., et al. (2011). A closely packed system of low-mass, low-density planets transiting Kepler-11. *Nature*, 470:53–58.

Lissauer, J. J., Fabrycky, D. C., Ford, E. B., Borucki, W. J., Fressin, F., Marcy, G. W., Orosz, J. A., Rowe, J. F., Torres, G., Welsh, W. F., et al. (2011). A closely packed system of low-mass, low-density planets transiting Kepler-11. *Nature*, 470(7332):53–58.

Lissauer, J. J., Marcy, G. W., Rowe, J. F., Bryson, S. T., Adams, E., Buchhave, L. A., Ciardi, D. R., Cochran, W. D., Fabrycky, D. C., Ford, E. B., et al. (2012). Almost All of Kepler's Multiple-planet Candidates Are Planets. *The Astrophysical Journal*, 750(2):112.

Lovis, C., Ségransan, D., Mayor, M., Udry, S., Benz, W., Bertaux, J.-L., Bouchy, F., Correia, A., Laskar, J., Lo Curto, G., et al. (2011). The HARPS search for southern extra-solar planets: XXVIII. Up to seven planets orbiting HD 10180: probing the architecture of low-mass planetary systems. *Astronomy & Astrophysics*, 528.

Marois, C., Zuckerman, B., Konopacky, Q. M., Macintosh, B., and Barman, T. (2010). Images of a fourth planet orbiting HR 8799. *Nature*, 468:1080–1083.

Martin, R. G., Armitage, P. J., and Alexander, R. D. (2013). Formation of circumbinary planets in a dead zone. *The Astrophysical Journal*, 773(1):74.

Masset, F. (2000). FARGO: A fast eulerian transport algorithm for differentially rotating disks. *The Astrophysical Journal Supplement Series*, 141:165–173.

Masset, F. and Casoli, J. (2009). On the horseshoe drag of a low-mass planet. II. Migration in adiabatic disks. *The Astrophysical Journal*, 703(1):857.

Masset, F. S. (2001). On the Co-orbital Corotation Torque in a Viscous Disk and Its Impact on Planetary Migration. *The Astrophysical Journal*, 558:453–462.

Masset, F. S. (2011). On type-I migration near opacity transitions. A generalized Lindblad torque formula for planetary population synthesis. *Celestial Mechanics and Dynamical Astronomy*, 111(1–2):131–160.

Masset, F. S. and Casoli, J. (2010). Saturated Torque Formula for Planetary Migration in Viscous Disks with Thermal Diffusion: Recipe for Protoplanet Population Synthesis. *The Astrophysical Journal*, 723:1393–1417.

Masset, F. S., D'Angelo, G., and Kley, W. (2006a). On the Migration of Protogiant Solid Cores. *The Astrophysical Journal*, 652:730–745.

Masset, F. S., Morbidelli, A., Crida, A., and Ferreira, J. (2006b). Disk Surface Density Transitions as Protoplanet Traps. *The Astrophysical Journal*, 642:478–487.

Masset, F. S. and Papaloizou, J. C. B. (2003). Runaway migration and the formation of hot jupiters. *The Astrophysical Journal*, 588(1):494.

Mayer, L. (2010). Formation via Disk Instability. *Formation and Evolution of Exoplanets (Ed. by Rory Barnes)*, pages 71–99.

Mayor, M. and Queloz, D. (1995). A Jupiter-mass companion to a solar-type star. *Nature*, 378(6555):355–359.

McLaughlin, D. B. (1924). Some results of a spectrographic study of the Algol system. *The Astrophysical Journal*, 60:22–31.

McNeil, D. S. and Nelson, R. P. (2010). On the formation of hot Neptunes and super-Earths. *Monthly Notices of the Royal Astronomical Society*, 401:1691–1708.

Mignone, A., Bodo, G., Massaglia, S., Matsakos, T., Tesileanu, O., Zanni, C., and Ferrari, A. (2007). PLUTO: A Numerical Code for Computational Astrophysics. *The Astrophysical Journal Supplement Series*, 170:228–242.

Mordasini, C., Alibert, Y., and Benz, W. (2009). Extrasolar planet population synthesis. I. Method, formation tracks, and mass-distance distribution. *Astronomy & Astrophysics*, 501:1139–1160.

Movshovitz, N., Bodenheimer, P., Podolak, M., and Lissauer, J. J. (2010). Formation of Jupiter using opacities based on detailed grain physics. *Icarus*, 209:616–624.

Müller, T. W. A., Kley, W., and Meru, F. (2012). Treating gravity in thin-disk simulations. *Astronomy & Astrophysics*, 541:A123.

Murray, C. D. and Dermott, S. F. (1999). *Solar system dynamics*. Cambridge university press.

Muto, T., Suzuki, T., and Inutsuka, S. (2010). Two-dimensional Study of the Propagation of Planetary Wake and the Indication of Gap Opening in an Inviscid Protoplanetary Disk. *The Astrophysical Journal*, 724:448–463.

Nelson, R. P. and Gressel, O. (2010). On the dynamics of planetesimals embedded in turbulent protoplanetary discs. *Monthly Notices of the Royal Astronomical Society*, 409:639–661.

Nelson, R. P., Papaloizou, J. C. B., Masset, F., and Kley, W. (2000). The migration and growth of protoplanets in protostellar discs. *Monthly Notices of the Royal Astronomical Society*, 318:18–36.

Norman, M. (2000). Introducing ZEUS-MP: A 3D, Parallel, Multiphysics Code for Astrophysical Fluid Dynamics. In *Revista Mexicana de Astronomia y Astrofisica Conference Series*, volume 9, pages 66–71.

Ogilvie, G. and Lubow, S. (2002). On the wake generated by a planet in a disc. *Monthly Notices of the Royal Astronomical Society*, 330(4):950–954.

Paardekooper, S., Baruteau, C., Crida, A., and Kley, W. (2010). A torque formula for non-isothermal type I planetary migration–I. Unsaturated horseshoe drag. *Monthly Notices of the Royal Astronomical Society*, 401(3):1950–1964.

Paardekooper, S., Baruteau, C., and Kley, W. (2011). A torque formula for non-isothermal Type I planetary migration–II. Effects of diffusion. *Monthly Notices of the Royal Astronomical Society*, 410(1):293–303.

Paardekooper, S. and Mellema, G. (2006). Halting type I planet migration in non-isothermal disks. *Astronomy & Astrophysics*, 459(1):17–20.

Paardekooper, S. and Papaloizou, J. (2008). On disc protoplanet interactions in a non-barotropic disc with thermal diffusion. *Astronomy & Astrophysics*, 485(3):877–895.

Paardekooper, S.-J. and Mellema, G. (2008). Growing and moving low-mass planets in non-isothermal disks. *Astronomy & Astrophysics*, 478:245–266.

Paardekooper, S.-J. and Papaloizou, J. (2009a). On corotation torques, horseshoe drag and the possibility of sustained stalled or outward protoplanetary migration. *Monthly Notices of the Royal Astronomical Society*, 394(4):2283–2296.

Paardekooper, S.-J. and Papaloizou, J. (2009b). On the width and shape of the corotation region for low-mass planets. *Monthly Notices of the Royal Astronomical Society*, 394(4):2297–2309.

Papaloizou, J. and Larwood, J. (2002). On the orbital evolution and growth of protoplanets embedded in a gaseous disc. *Monthly Notices of the Royal Astronomical Society*, 315(4):823–833.

Papaloizou, J. and Lin, D. (1984). On the tidal interaction between protoplanets and the primordial solar nebula. I-Linear calculation of the role of angular momentum exchange. *The Astrophysical Journal*, 285:818–834.

Papaloizou, J. and Lin, D. (1995). Theory of accretion disks I: Angular momentum transport processes. *Annual Review of Astronomy and Astrophysics*, 33:505–540.

Peiró, J. and Sherwin, S. (2005). Finite difference, finite element and finite volume methods for partial differential equations. In *Handbook of materials modeling*, pages 2415–2446. Springer.

Pierens, A. and Nelson, R. P. (2010). On the growth and orbital evolution of giant planets in layered protoplanetary disks. *Astronomy & Astrophysics*, 520:A14.

Pierens, A. and Nelson, R. P. (2013). Migration and gas accretion scenarios for the Kepler 16, 34, and 35 circumbinary planets. *Astronomy & Astrophysics*, 556:A134.

Pollack, J. B., Hubickyj, O., Bodenheimer, P., Lissauer, J. J., Podolak, M., and Greenzweig, Y. (1996). Formation of the Giant Planets by Concurrent Accretion of Solids and Gas. *Icarus*, 124:62–85.

Pringle, J. E. (1981). Accretion discs in astrophysics. *Annual Review of Astronomy and Astrophysics*, 19:137–162.

Rauer, H., Catala, C., Aerts, C., Appourchaux, T., Benz, W., Brandeker, A., Christensen-Dalsgaard, J., Deleuil, M., Gizon, L., Goupil, M.-J., Güdel, M., Janot-Pacheco, E., Mas-Hesse, M., Pagano, I., Piotto, G., Pollacco, D., Santos, N. C., Smith, A., -C., J., Suárez, Szabó, R., Udry, S., Adibekyan, V., Alibert, Y., Almenara, J.-M., Amaro-Seoane, P., Ammler-von Eiff, M., Asplund, M., Antonello, E., Ball, W., Barnes, S., Baudin, F., Belkacem, K., Bergemann, M., Bihain, G., Birch, A. C., Bonfils, X., Boisse, I., Bonomo, A. S., Borsa, F., Brandão, I. M., Brocato, E., Brun, S., Burleigh, M., Burston, R., Cabrera, J., Cassisi, S., Chaplin, W., Charpinet, S., Chiappini, C., Church, R. P., Csizmadia, S., Cunha, M., Damasso, M., Davies, M. B., Deeg, H. J., Diaz, R. F., Dreizler, S., Dreyer, C., Eggenberger, P., Ehrenreich, D., Eigmüller, P., Erikson, A., Farmer, R., Feltzing, S., de Oliveira Fialho, F., Figueira, P., Forveille, T., Fridlund, M., Garcia, R. A., Giommi, P., Giuffrida, G., Godolt, M., Gomes da Silva, J., Granzer, T., Grenfell, J. L.,

Grotsch-Noels, A., Günther, E., Haswell, C. A., Hatzes, A. P., Hébrard, G., Hekker, S., Helled, R., Heng, K., Jenkins, J. M., Johansen, A., Khodachenko, M. L., Kislyakova, K. G., Kley, W., Kolb, U., Krivova, N., Kupka, F., Lammer, H., Lanza, A. F., Lebreton, Y., Magrin, D., Marcos-Arenal, P., Marrese, P. M., Marques, J. P., Martins, J., Mathis, S., Mathur, S., Messina, S., Miglio, A., Montalban, J., Montalto, M., Monteiro, M. J. P. F. G., Moradi, H., Moravveji, E., Mordasini, C., Morel, T., Mortier, A., Nascimbeni, V., Nelson, R. P., Nielsen, M. B., Noack, L., Norton, A. J., Ofir, A., Oshagh, M., Ouazzani, R.-M., Pápics, P., Parro, V. C., Petit, P., Plez, B., Poretti, E., Quirrenbach, A., Ragazzoni, R., Raimondo, G., Rainer, M., Reese, D. R., Redmer, R., Reffert, S., Rojas-Ayala, B., Roxburgh, I. W., Salmon, S., Santerne, A., Schneider, J., Schou, J., Schuh, S., Schunker, H., Silva-Valio, A., Silvotti, R., Skillen, I., Snellen, I., Sohl, F., Sousa, S. G., Sozzetti, A., Stello, D., Strassmeier, K. G., Švanda, M., Szabó, G. M., Tkachenko, A., Valencia, D., van Grootel, V., Vauclair, S. D., Ventura, P., Wagner, F. W., Walton, N. A., Weingrill, J., Werner, S. C., Wheatley, P. J., and Zwintz, K. (2013). The PLATO 2.0 Mission. *ArXiv e-prints*.

Rein, H. (2012). A proposal for community driven and decentralized astronomical databases and the Open Exoplanet Catalogue. *ArXiv e-prints*, 1211.7121.

Rossiter, R. A. (1924). On the detection of an effect of rotation during eclipse in the velocity of the brigher component of beta Lyrae, and on the constancy of velocity of this system. *The Astrophysical Journal*, 60:15–21.

Rowe, J. F., Bryson, S. T., Marcy, G. W., Lissauer, J. J., Jontof-Hutter, D., Mullally, F., Gilliland, R. L., Issacson, H., Ford, E., Howell, S. B., Borucki, W. J., Haas, M., Huber, D., Steffen, J. H., Thompson, S. E., Quintana, E., Barclay, T., Still, M., Fortney, J., Gautier, III, T. N., Hunter, R., Caldwell, D. A., Ciardi, D. R., Devore, E., Cochran, W., Jenkins, J., Agol, E., Carter, J. A., and Geary, J. (2014). Validation of Kepler's Multiple Planet Candidates. III. Light Curve Analysis and Announcement of Hundreds of New Multi-planet Systems. *The Astrophysical Journal*, 784:45.

S. Udry, X. Bonfils, X. Delfosse, T. Forveille, M. Mayor, C. Perrier, F. Bouchy, C. Lovis, F. Pepe, D. Queloz, and J.-L. Bertaux (2007). The HARPS search for southern extra-solar planets. *Astronomy & Astrophysics*, 469(3):L43–L47.

Safronov, V. S. (1969). *Evolution of the protoplanetary cloud and formation*

of the earth and planets. Translated from the Russian by the Israel Program for Scientific Translations (1972).

Shakura, N. and Sunyaev, R. (1973). Black holes in binary systems. Observational appearance. *Astronomy & Astrophysics*, 24:337–355.

Snellgrove, M. D., Papaloizou, J. C. B., and Nelson, R. P. (2001). On disc driven inward migration of resonantly coupled planets with application to the system around GJ876. *Astronomy & Astrophysics*, 374:1092–1099.

Stone, J. M., Mihalas, D., and Norman, M. L. (1992). ZEUS-2D: A radiation magnetohydrodynamics code for astrophysical flows in two space dimensions. III: The radiation hydrodynamic algorithms and tests. *The Astrophysical Journal Supplement Series*, 80:819–845.

Stone, J. M. and Norman, M. L. (1992a). ZEUS-2D: A radiation magnetohydrodynamics code for astrophysical flows in two space dimensions. I: The hydrodynamic algorithms and tests. *The Astrophysical Journal Supplement Series*, 80:753–790.

Stone, J. M. and Norman, M. L. (1992b). ZEUS-2D: A radiation magnetohydrodynamics code for astrophysical flows in two space dimensions. II: The magnetohydrodynamic algorithms and tests. *The Astrophysical Journal Supplement Series*, 80(2):791–818.

Struve, O. (1952). Proposal for a project of high-precision stellar radial velocity work. *The Observatory*, 72:199–200.

Tanaka, H., Takeuchi, T., and Ward, W. R. (2002). Three-Dimensional Interaction between a Planet and an Isothermal Gaseous Disk. I. Corotation and Lindblad Torques and Planet Migration. *The Astrophysical Journal*, 565:1257–1274.

Tanaka, H. and Ward, W. R. (2004). Three-dimensional Interaction between a Planet and an Isothermal Gaseous Disk. II. Eccentricity Waves and Bending Waves. *The Astrophysical Journal*, 602:388–395.

Terquem, C. and Papaloizou, J. C. B. (2007). Migration and the Formation of Systems of Hot Super-Earths and Neptunes. *The Astrophysical Journal*, 654:1110–1120.

Terquem, C. E. J. M. L. J. (2008). New Composite Models of Partially Ionized Protoplanetary Disks. *The Astrophysical Journal*, 689:532–538.

Toro, E. F. (2009). *Riemann solvers and numerical methods for fluid dynamics: a practical introduction*. Springer.

Vicente, S. M. and Alves, J. (2005). Size distribution of circumstellar disks in the Trapezium cluster. *Astronomy & Astrophysics*, 441(1):195–205.

Ward, W. R. (1991). Horsehoe Orbit Drag. In *Lunar and Planetary Institute Science Conference Abstracts*, volume 22 of *Lunar and Planetary Institute Science Conference Abstracts*, page 1463.

Ward, W. R. (1997). Protoplanet Migration by Nebula Tides. *Icarus*, 126:261–281.

Weidenschilling, S. (1977). The distribution of mass in the planetary system and solar nebula. *Astrophysics and Space Science*, 51(1):153–158.

Williams, J. P. and Cieza, L. A. (2011). Protoplanetary Disks and Their Evolution. *Annual Review of Astronomy and Astrophysics*, 49(1):67–117.

Wolszczan, A. and Frail, D. A. (1992). A planetary system around the millisecond pulsar PSR1257 + 12. *Nature*, 355:145–147.

Wright, J. T., Fakhouri, O., Marcy, G. W., Han, E., Feng, Y., Johnson, J. A., Howard, A. W., Fischer, D. A., Valenti, J. A., Anderson, J., and Piskunov, N. (2011). The Exoplanet Orbit Database. *Publications of the Astronomical Society of the Pacific*, 123(902):pp. 412–422.

Wright, J. T. and Gaudi, B. S. (2013). Exoplanet detection methods. In Oswalt, T. D., French, L. M., and Kalas, P., editors, *Planets, Stars and Stellar Systems*, pages 489–540. Springer Netherlands.

Wu, Y. and Murray, N. (2003). Planet Migration and Binary Companions: The Case of HD 80606b. *The Astrophysical Journal*, 589:605–614.

Wyatt, M. C. (2008). Evolution of debris disks. *Annual Review of Astronomy and Astrophysics*, 46:339–383.

Ziegler, U. (1998). NIRVANA+: An adaptive mesh refinement code for gas dynamics and MHD. *Computer Physics Communications*, 109(2):111–134.

Ziegler, U. (2008). The NIRVANA code: Parallel computational MHD with adaptive mesh refinement. *Computer Physics Communications*, 179(4):227–244.

Zingale, M., Dursi, L. J., ZuHone, J., Calder, A. C., Fryxell, B., Plewa, T., Truran, J. W., Caceres, A., Olson, K., Ricker, P. M., Riley, K., Rosner, R., Siegel, A., Timmes, F. X., and Vladimirova, N. (2002). Mapping Initial Hydrostatic Models in Godunov Codes. *The Astrophysical Journal Supplement Series*, 143:539–565.